JYVÄSKYLÄ STUDIES IN COMPUTING

2

Dmitri Kuzmin

Numerical Simulation of Reactive Bubbly Flows

UNIVERSITY OF JYVÄSKYLÄ

JYVÄSKYLÄ 1999

JYVÄSKYLÄ STUDIES IN COMPUTING 2

Dmitri Kuzmin

Numerical Simulation of Reactive Bubbly Flows

Esitetään Jyväskylän yliopiston informaatioteknologian tiedekunnan suostumuksella
julkisesti tarkastettavaksi yliopiston vanhassa juhlasalissa (S212)
marraskuun 19. päivänä 1999 kello 12.

Academic dissertation to be publicly discussed, by permission of
the Faculty of Information Technology of the University of Jyväskylä,
in Auditorium S212, on November 19, 1999 at 12 o'clock noon.

UNIVERSITY OF JYVÄSKYLÄ

JYVÄSKYLÄ 1999

Numerical Simulation of Reactive Bubbly Flows

JYVÄSKYLÄ STUDIES IN COMPUTING 2

Dmitri Kuzmin

Numerical Simulation of Reactive Bubbly Flows

UNIVERSITY OF JYVÄSKYLÄ

JYVÄSKYLÄ 1999

Editors
Tommi Kärkkäinen
Department of Computer Science and Information Systems, University of Jyväskylä
Kaarina Nieminen
Publishing Unit, University Library of Jyväskylä

URN:ISBN:978-951-39-9625-3
ISBN 978-951-39-9625-3 (PDF)
ISSN 1456-5390

Jyväskylän yliopisto, 2023

ISBN 951-39-0574-8
ISSN 1456-5390

Copyright © 1999, by University of Jyväskylä

Jyväskylä University Printing House, Jyväskylä and
ER-Paino Ky, Lievestuore 1999

ABSTRACT

Kuzmin, Dmitri
Numerical Simulation of Reactive Bubbly Flows
Jyväskylä: University of Jyväskylä, 1999. 110 p.
(Jyväskylä Studies in Computing,
ISSN 1456-5390; 2)
ISBN 951-39-0574-8
Finnish summary
Diss.

The interaction of numerous physical and chemical phenomena in bubble columns, a popular type of multiphase reactors, is studied numerically. The state of the art of gas-liquid flow modeling is reviewed, and a sophisticated mathematical model is assembled. It combines a detailed treatment of the two-phase flow hydrodynamics with consideration of mass transfer possibly enhanced by homogeneous chemical reaction in the liquid phase. Reasonable model simplifications are discussed.

Approximate solution to the problem at hand is obtained by the finite element method. The numerical challenges to be faced are the tracking of moving boundaries, dominating convection and strong nonlinearities, to name just a few. Operator-splitting techniques are employed to decompose the original problem into a set of tractable subproblems. Proper solution tools are proposed in each case, and their performance is illustrated by application to benchmark problems. Notable accomplishments include a strategy for inflow/outflow boundary treatment within a Lagrangian space-time finite element method, a pointwise limiter for pure convection problems and a simplified mass-conserving projection scheme for the intergrid transfer of data. These and other elemental components are embedded into a global numerical algorithm for dynamic numerical simulation of gas-driven flows in a bubble column reactor.

The advocated approach is applied to investigate the startup behavior of a two-dimensional bubble column under a wide range of operating conditions. The role played by various model parameters is analyzed. The presented computational results are in good qualitative agreement with experimental data available in the literature.

Keywords: multiphase flow, mass transfer, chemical reactions, convection-dominated transport, Navier-Stokes equations, finite element method, operator-splitting

Author's Address

Dmitri Kuzmin
Department of Mathematical
Information Technology
University of Jyväskylä
P.O. Box 35, FIN-40351
Jyväskylä, Finland

E-mail: kuzmin@mit.jyu.fi

Supervisors

Docent Heikki Haario
Department of Mathematics
University of Helsinki
Finland

Professor Pekka Neittaanmäki
Department of Mathematical
Information Technology
University of Jyväskylä
Finland

Professor Timo Tiihonen
Department of Mathematical
Information Technology
University of Jyväskylä
Finland

Reviewers

Professor Roland Glowinski
Department of Mathematics
University of Houston
USA

Professor Stefan Turek
Institute for Applied Mathematics
University of Dortmund
Germany

Opponent

Professor Peter Hansbo
Department of Solid Mechanics
Chalmers University of Technology
Sweden

ACKNOWLEDGEMENTS

I would like to express my sincere gratitude to Prof. Pekka Neittaanmäki and Prof. Timo Tiihonen (University of Jyväskylä, Finland) for introducing me into the realm of numerical mathematics and giving me the opportunity to work at the Laboratory of Scientific Computing, where I have enjoyed a friendly atmosphere and access to superb research facilities. I am also deeply indebted to my late supervisor, Prof. Valery Rivkind, for specifying the general direction of my research and exposing me to computational fluid dynamics.

I am extremely grateful to my adviser, Prof. Heikki Haario (University of Helsinki, Finland). The accomplishments reported in this thesis would have been impossible without his continuous support, numerous discussions and encouragement. On this occasion, I would also like to acknowledge a fruitful collaboration with M. Sc. Anton Smolianski (University of Jyväskylä, Finland) and thank him for the insightful perusal of my manuscripts and valuable feedback.

My deepest appreciation goes to Dr. Alexander Sokolichin (University of Stuttgart, Germany) for sharing his expertise in numerical simulation of bubble columns with me. I have greatly benefited from his assistance during my first numerical experiments as well as from his comments regarding the outcome of my research.

Support of this work by COMAS Graduate School of the University of Jyväskylä, by the Academy of Finland and by TEKES Technology Development Center is gratefully acknowledged.

Jyväskylä, July 1999

Dmitri Kuzmin

CONTENTS

1 INTRODUCTION **9**

2 MATHEMATICAL MODEL **13**
2.1 Physical assumptions 13
2.2 Evolution of the bubble size 14
2.3 Fluid dynamics of bubbly flow 15
2.4 Interphase momentum transfer 17
2.5 Model simplifications 18
2.6 Bubble path dispersion 21
2.7 Chemical reactions 22
2.8 Interphase mass transfer 23
2.9 System of equations 25

3 DEVELOPMENT OF FINITE ELEMENT SCHEMES FOR FLUID DYNAMICS **27**
3.1 Motivation 27
3.2 Free-Lagrange space-time FEM 29
3.2.1 Overview 29
3.2.2 Finite element formulation for convection-diffusion . . 30
3.2.3 Implementation aspects 34
3.2.4 Numerical examples 44
3.3 High-resolution finite element schemes: PCT versus FCT . . 46
3.3.1 Overview 46
3.3.2 High and low-order schemes 47
3.3.3 Flux-corrected transport 50
3.3.4 Pointwise-corrected transport 52
3.3.5 Numerical examples 54
3.4 Fractional-step projection method 57
3.4.1 Overview 57
3.4.2 Initial-boundary value problem 59
3.4.3 Projection guidelines 60
3.4.4 Fractional-step algorithm 64
3.4.5 Numerical examples 68

4 NUMERICAL ALGORITHM **74**
4.1 Operator-splitting 74
4.2 Gas phase variables 75

4.3 Velocity fields 76
4.4 Concentrations of species 78
4.5 Projection between meshes 78
4.6 Summary of the algorithm 80

5 SIMULATION OF BUBBLE COLUMN REACTORS 82

6 CONCLUDING REMARKS 96

LIST OF SYMBOLS 99

BIBLIOGRAPHY 101

FINNISH SUMMARY 110

Chapter 1

INTRODUCTION

Bubbly flows with mass transfer accompanied by chemical reactions are encountered in many important industrial processes. In this thesis, we focus on investigation of the dynamic behavior of bubble column reactors which are widespread in chemical industry. These devices are used to bring reactive components contained in respective phases (gas and liquid) into mutual contact. In its most simple form, a bubble column is a liquid-filled cylindrical tank with an aspect ratio (height over diameter) typically between 2 and 10. The gas consisting of one or several components is fed at the bottom of the reactor through a gas sparger which may vary in design. If the gas is supplied through the entire cross-section, we speak of a uniformly aerated bubble column (Figure 1.1, left), otherwise the bubble column at hand is classified as locally aerated (Figure 1.1, right).

The ascending bubbles entrain liquid with them and lead to unsteady circulating flows in the liquid phase catering for a high level of backmixing. One of the key operating parameters is the superficial gas velocity, which is defined as the ratio of gas throughput to the cross-section area. In concert with other adjustable operating conditions, construction parameters and process-specific data, it determines the flow modes which prevail in the bubble column [10]. The gaseous reactants are absorbed into the bulk liquid where they proceed to react with the liquid itself or with some other species dissolved or suspended in it. Chemical reactions can be used either to produce a desired new substance or to increase the capacity of equipment for gas scrubbing (removal of an unwanted component from a gas stream). In the former case, it is essential to be aware of the nature and amounts of any byproducts formed. In fact, the cost of the reactor may not appear to be large as compared to that of the associated equipment for separation and purification of products.

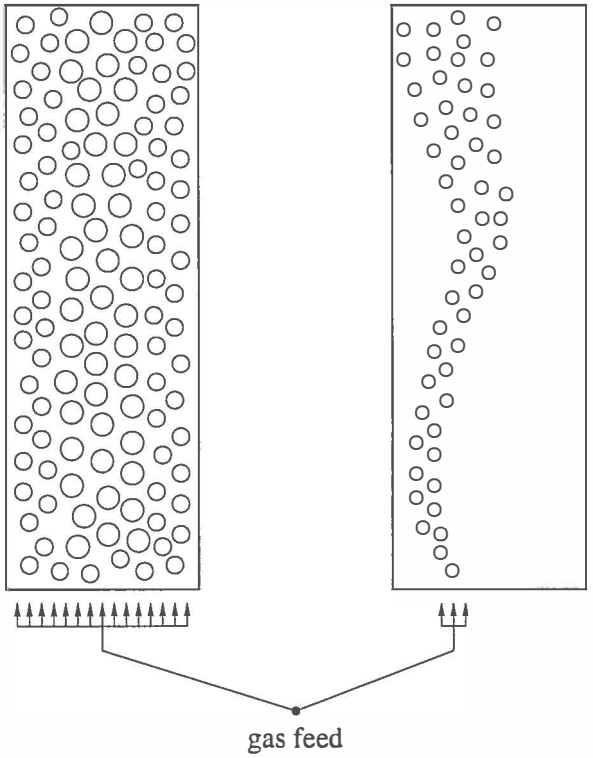

FIGURE 1.1 Uniformly (left) and locally (right) aerated bubble column.

The advantages of bubble column reactors include low cost, simplicity of construction, excellent heat transfer characteristics, and the lack of any mechanically operated parts. However, this simple environment gives rise to extremely complex flow patterns and interactions between physical and chemical parameters, which makes an efficient design and scale-up of such units a challenging task.

Traditional chemical engineering approach to design of bubble columns is based on simplified one-dimensional reactor models. Depending on the estimated degree of mixing, each phase (gas or liquid) can be described by

- CSTR, continuous stirred tank reactor model (perfect mixing).
- ADM, axial dispersion model (partial mixing).
- PFM, plug flow model (ideal tubular flow).

Combinations of models which involve a higher level of mixing for the gas phase than for the liquid phase are ruled out [10]. The axial dispersion model for both gas and liquid is allegedly the most relevant choice for industrial-scale bubble columns. However, incorporation of all mixing processes into one overall dispersion coefficient results in a very remote picture of reality. Due to the complex flow structure, no general relationship for the dispersion coefficient has been established. Therefore, design and scale-up of bubble column reactors using dispersion models is rather uncertain and unreliable.

The past decade has witnessed the advent of more fundamental modeling techniques. Multiphase fluid dynamics has provided a proper description of the gas-liquid flow. Numerical simulation validated by comparison with experimental data has become an increasingly popular tool for investigation of the multifarious flow patterns unfolding inside bubble columns [11], [28], [50], [65], [78], [85]. The most recent developments in this field and spectacular numerical results can be found in [19]. Advanced mathematical models for dispersed two-phase flow can be classified into the so-called Euler-Euler and Euler-Lagrange formulations [78], [79]. The salient features of both approaches are briefly outlined below.

The Euler-Euler model treats both gas and liquid phase as space-sharing interpenetrating continua. Each phase is assumed present at every point in the reactor and assigned a volume fraction representing the share of space occupied by that phase in a small control volume around the point. The two-phase flow equations governing the conservation of mass and momentum for each phase are obtained by postulation or by averaging of the associated single-phase continuity and momentum equations. As a rule, the phases have individual density, velocity and pressure fields which interact via the interphase transfer terms. The premise behind this theory is that the desired spatial resolution corresponds to a substantially larger scale than the size of a single bubble.

The Euler-Lagrange formulation retains a continuous treatment for the liquid phase, whereas bubbles or bubble clusters are tracked in a Lagrangian way by solving the Newtonian equations of motion. The nonuniform distribution of bubbles in the reactor is responsible for dynamic variations in the mean density of the continuous phase. This creates buoyancy forces leading to convective flows in the bubble column. The Euler-Lagrange model warrants the absence of pernicious numerical diffusion in the gas phase and offers considerable advantages if gas absorption as well as bubble coalescence and breakup are to be taken into account. These benefits are offset by the fact that the computational time and storage requirements strongly depend on the number of bubbles to be followed, so that numerical simulation can

become prohibitively expensive as the size of the reactor approaches the industrial scale. Therefore, we subscribe to the Euler-Euler viewpoint in this thesis.

Computational fluid dynamics has provided a deeper insight into the flow characteristics and gas holdup distribution in bubble columns. However, most of the numerical studies published to date were limited to inert systems, the dissertation of Hillmer [36] being a notable exception to this rule. It is possible to consider the fluid dynamics and reaction phenomena sequentially only for negligibly small absorption rates. Otherwise, a complex interplay of the hydrodynamics, mass transfer and chemical reactions must be reckoned with. Indeed, reaction enhanced mass transfer often spells considerable spatial and temporal variations of the bubble size, gas holdup and interfacial area. Since the system is essentially gas driven, changes in the void fraction can result in entirely different circulation patterns or even effect transition from the heterogeneous flow regime to the homogeneous one and vice versa [36]. The velocity fields respond by altering the backmixing in both phases.

One of the main goals pursued in this thesis is to bridge the gap between simulations of the fluid dynamics of bubble columns and absorption/reaction processes by means of a practical two-phase flow model which would allow for the interphase mass transfer and expansion of the rising bubbles due to the fall of hydrostatic pressure. The finite element method is chosen for approximate solution of partial differential equations because of its flexibility and the possibility of using unstructured grids and a wealth of adaptive techniques. The quest for suitable numerical schemes has spurred some interesting algorithmic developments, the exposition of which constitutes the core of this thesis.

The thesis is organized as follows. In Chapter 2, we assemble a detailed mathematical model for reactive gas-liquid flow in a bubble column. Our contribution to the development of finite element methods for convection-dominated problems in fixed and variable domains is reported in Chapter 3. A global numerical algorithm for bubble column simulations is worked out in Chapter 4 and its performance is illustrated by computational results presented in Chapter 5. Finally, in Chapter 6 we draw conclusions and point out some prospective directions for further research.

Chapter 2

MATHEMATICAL MODEL

2.1 Physical assumptions

We consider an unsteady two-dimensional flow in a wafer bubble column. Because of the uncertainty connected with applicability of single-phase turbulence models to gas-liquid flows, we use a constant effective viscosity equal to the laminar viscosity multiplied by a factor of 100. This approach was shown to yield a good quantitative agreement with experimental results [2]. The column is assumed to be operated in the bubbly flow regime under isothermal conditions. Small spherical bubbles consist of a pure gas whose pressure and density are related by the ideal gas law

$$p_G = \rho_G \frac{R}{\eta} T. \tag{2.1}$$

Here R is the universal gas constant, T is the temperature and η is the molar mass of species. The liquid density ρ_L is constant. Throughout the thesis the subscript G will refer to the gas phase and L will be reserved for the liquid phase.

One of our key variables is the local gas holdup or the volume fraction of the gas phase which is defined by

$$\epsilon = \frac{4}{3}\pi a^3 n, \tag{2.2}$$

where a is the average bubble radius and n is the number density which denotes the number of bubbles in a unit volume of bubbly liquid. We will consider dilute bubbly flows, so that direct interactions and collisions of bubbles can be neglected. If there is no coalescence or breakup of bubbles,

then the number density is conserved:

$$\frac{\partial n}{\partial t} + \nabla \cdot (n\mathbf{v}_G) = 0, \tag{2.3}$$

where $\mathbf{v}_G$ is the gas phase velocity. Gas dissolution will manifest itself in the vanishing radius of the bubble.

Remark 2.1. If coalescence and breakup of bubbles do occur, the number density varies with the bubble mass m and is called the bubble size distribution function $f = f(\mathbf{x}, t, m)$. Then equations (2.2) and (2.3) should be replaced by the following relations [21], [50]

$$\frac{\partial f}{\partial t} + \nabla \cdot (f\mathbf{v}_G) + \frac{\partial (f\dot{m})}{\partial m} = D + S - L, \tag{2.4}$$

$$\epsilon(\mathbf{x}, t) = \frac{1}{\rho_G} \int_0^\infty m f(\mathbf{x}, t, m)\, dm, \tag{2.5}$$

where $\dot{m}$ is the rate of gas absorption, D takes account of dispersive effects in the gas phase, S and L are the source and sink terms due to coalescence and breakup. Bubbles of mass m can be formed by coalescence of smaller bubbles or breakup of larger bubbles. The associated bubble radius a is given by

$$a = \sqrt[3]{\frac{3m}{4\pi\rho_G}}. \tag{2.6}$$

By virtue of the ideal gas law, changes in the gas holdup and interfacial area due to different pressures at different heights are afforded by this model.

2.2 Evolution of the bubble size

The bubbles are released at the bottom of the reactor into an initially stagnant pool of liquid. The volume of a rising bubble is not constant, and its rate of change depends primarily on two phenomena. On the one hand, the bubble expands due to the fall of liquid pressure. On the other hand, it shrinks due to mass transfer into the liquid. The net effect on the bubble size will depend on the relative importance of these factors.

The behavior of a single bubble in an infinite domain of liquid can be described by the Rayleigh-Plesset system which is derived analytically from the Navier-Stokes equations formulated for a time-dependent spherically symmetric motion of incompressible fluid about a spherical bubble [57], [58]. If

gas absorption is taken into account, the radial velocity of liquid w and the bubble radius a satisfy

$$a\left(\frac{\partial w}{\partial t}+\mathbf{v}_G\cdot\nabla w\right)+\frac{3}{2}w^2=\frac{1}{\rho_L}\left(p_G-p_\infty-4\mu\frac{w}{a}-\frac{2\sigma}{a}\right), \quad (2.7)$$

$$\frac{\partial a}{\partial t}+\mathbf{v}_G\cdot\nabla a=w-\frac{\eta\mathcal{N}}{\rho_L}, \quad (2.8)$$

where p_∞ is the liquid pressure at infinity, μ is the dynamic viscosity, σ is the surface tension coefficient and $\mathcal{N}$ is the molar flux defining the rate of interphase mass transfer (see below).

Equation (2.7) can be generalized to take account of the presence of other bubbles in the flow field and the motion of liquid past them on the assumption that the bubbles preserve their spherical shape [57], [58]. The evolution of w along the streamlines of the gas phase is given by

$$\begin{aligned}(1-\xi_1)a\left(\frac{\partial w}{\partial t}+\mathbf{v}_G\cdot\nabla w\right)&=\frac{1}{\rho_L}\left(p_G-p_L-4\mu\frac{w}{a}-\frac{2\sigma}{a}\right)\\&-(1-\xi_2)\frac{3}{2}w^2+(1-\xi_3)\frac{|\mathbf{v}_{\text{slip}}|^2}{4},\end{aligned} \quad (2.9)$$

where p_L is the pressure in the liquid phase, $\mathbf{v}_{\text{slip}}=\mathbf{v}_G-\mathbf{v}_L$ is the slip velocity, and ξ_1, ξ_2, ξ_3 are correction coefficients. They were found to be

$$\xi_1\approx\frac{1.1\epsilon^{1/3}-\epsilon}{1-\epsilon},\quad \xi_2\approx\frac{1.5\epsilon^{1/3}-1.3\epsilon}{1-\epsilon},\quad \xi_3\approx\frac{\epsilon}{1-\epsilon}$$

for a locally uniform distribution of bubbles, and

$$\xi_1\approx 3.6\epsilon,\qquad \xi_2\approx 12\epsilon$$

for a chaotic distribution [57].

Remark 2.2. To keep things simple, we use the original equation (2.7) with the hydrostatic pressure p_H in lieu of p_∞ in our numerical simulations.

2.3 Fluid dynamics of bubbly flow

Multiphase flow models have their origins in single-phase continuum mechanics. Each phase satisfies a system of conservation laws, and namely the continuity and momentum equations with appropriate jump conditions at the moving gas-liquid interface. These microscopic equations provide an exact description of the two-phase flow. However, such level of resolution is

neither necessary nor desirable to gain an insight into the overall behavior of the bubble column. The flow details are commonly suppressed by applying some kind of averaging (space, time or ensemble) to the microscopic equations multiplied by the phase indicator function. This yields macroscopic balances of mass and momentum for each phase. The averaging process can be bypassed by directly postulating the two-phase flow equations. The resulting relations rarely differ in anything but minor detail [18], [58]. They constitute the two-fluid or Euler-Euler [78] model. The macroscopic continuity equations read [17]

$$\frac{\partial \tilde{\rho}_G}{\partial t} + \nabla \cdot (\tilde{\rho}_G \mathbf{v}_G) = -4\pi a^2 n \eta \mathcal{N}, \tag{2.10}$$

$$\frac{\partial \tilde{\rho}_L}{\partial t} + \nabla \cdot (\tilde{\rho}_L \mathbf{v}_L) = 4\pi a^2 n \eta \mathcal{N}, \tag{2.11}$$

where $\tilde{\rho}_G = \epsilon \rho_G$ and $\tilde{\rho}_L = (1-\epsilon)\rho_L$ are the effective densities.

Conservation of momentum is given by [17]

$$\begin{aligned}
\frac{\partial(\tilde{\rho}_G \mathbf{v}_G)}{\partial t} + \nabla \cdot (\tilde{\rho}_G \mathbf{v}_G \mathbf{v}_G) &= -\epsilon \nabla p_G + \tilde{\rho}_G \mathbf{g} \\
&+ (p_G^* - p_G)\nabla \epsilon + \mathbf{f}_{\text{int}} - 4\pi a^2 n \eta \mathcal{N} \mathbf{v}_G^*, \\
\frac{\partial(\tilde{\rho}_L \mathbf{v}_L)}{\partial t} + \nabla \cdot (\tilde{\rho}_L \mathbf{v}_L \mathbf{v}_L) &= -(1-\epsilon)\nabla p_L + \nabla \cdot (2\tilde{\mu}\mathcal{D}(\mathbf{v}_L)) + \tilde{\rho}_L \mathbf{g} \\
&- (p_L^* - p_L)\nabla \epsilon - \mathbf{f}_{\text{int}} + 4\pi a^2 n \eta \mathcal{N} \mathbf{v}_L^*,
\end{aligned}$$

where $\tilde{\mu} = (1-\epsilon)\mu$ is the effective viscosity,

$$\mathcal{D}(\mathbf{v}_L) = \frac{1}{2}(\nabla \mathbf{v}_L + (\nabla \mathbf{v}_L)^T)$$

is the deformation rate tensor, $\mathbf{g}$ is the gravitational force, p_G^* and p_L^* are the interfacial pressures, $\mathbf{f}_{\text{int}}$ is the interphase force, $\mathbf{v}_G^*$ and $\mathbf{v}_L^*$ are the interfacial velocities. Constituitive equations will be supplied for the terms which are left unspecified for the time being.

We neglect the change of average momentum as the mass is crossing the interface and set

$$\mathbf{v}_L^* = \mathbf{v}_G^* = \mathbf{v}_G.$$

The interfacial pressures are related by the Young-Laplace equation

$$p_L^* = p_G^* - \frac{2\sigma}{a}.$$

Since the bubbles are small, the gas pressure within them cannot differ much from that at the interface. Thus, we can consider

$$p_G^* = p_G.$$

Invoking the continuity equations, we rearrange momentum balances to read

$$\tilde{\rho}_G \left(\frac{\partial \mathbf{v}_G}{\partial t} + (\mathbf{v}_G \cdot \nabla)\mathbf{v}_G \right) = -\epsilon \nabla p_G + \tilde{\rho}_G \mathbf{g} + \mathbf{f}_{\text{int}}, \tag{2.12}$$

$$\begin{aligned} \tilde{\rho}_L \left(\frac{\partial \mathbf{v}_L}{\partial t} + (\mathbf{v}_L \cdot \nabla)\mathbf{v}_L \right) &= -(1-\epsilon)\nabla p_L + \nabla \cdot (2\tilde{\mu}\mathcal{D}(\mathbf{v}_L)) + \tilde{\rho}_L \mathbf{g} \\ &- \left(p_G - p_L - \frac{2\sigma}{a} \right) \nabla \epsilon - \mathbf{f}_{\text{int}} + 4\pi a^2 n \eta \mathcal{N} \mathbf{v}_{\text{slip}}. \end{aligned} \tag{2.13}$$

In non-aerated regions we have a single-phase incompressible flow. In this case, $\epsilon = 0$ and the interphase transfer terms vanish, so that (2.13) and (2.11) reduce to the standard form of the Navier-Stokes equations.

2.4 Interphase momentum transfer

The interphase force $\mathbf{f}_{\text{int}}$ takes account of the momentum exchange between the dispersed (gas) and continuous (liquid) phase. Its constituents have been subject to a lot of controversy in the literature. It is commonly accepted that $\mathbf{f}_{\text{int}}$ involves contributions from the drag force, the virtual mass force and the lift force:

$$\mathbf{f}_{\text{int}} = \mathbf{f}_D + \mathbf{f}_{VM} + \mathbf{f}_L. \tag{2.14}$$

The drag force is experienced by a bubble moving steadily through the surrounding liquid. It is usually expressed in terms of a dimensionless drag coefficient C_D as follows

$$\mathbf{f}_D = -\epsilon C_D \frac{3}{8} \frac{\rho_L}{a} |\mathbf{v}_{\text{slip}}| \mathbf{v}_{\text{slip}}. \tag{2.15}$$

The drag coefficient is a function of the Reynolds number $Re = \frac{2a\rho_L}{\mu}|\mathbf{v}_{\text{slip}}|$ and depends among other things on the presence of surfactants which make the bubble behave as a solid particle. A comprehensive summary of correlations for C_D under various flow conditions can be found in Clift *et al.* [8]. A very simple formula was proposed by Schwarz and Turner [74]. They introduce

$$C_W = C_D \frac{3}{8} \frac{\rho_L}{a} |\mathbf{v}_{\text{slip}}| \tag{2.16}$$

and assign it a constant value $5 \times 10^4 \frac{kg}{m^3 s}$ which implies a slip velocity of approximately 20 cm/s. This is reported to agree well with experimental data for air bubbles with diameters between 1 and 10 mm rising in tap water. The drag force simplifies to

$$\mathbf{f}_D = -\epsilon C_W \mathbf{v}_{\text{slip}}. \tag{2.17}$$

The virtual mass force arises from resistance due to an "added mass" of liquid that has to be accelerated along with the bubble. It has the form

$$\mathbf{f}_{VM} = \epsilon C_{VM} \rho_L \left[\left(\frac{\partial \mathbf{v}_L}{\partial t} + (\mathbf{v}_L \cdot \nabla)\mathbf{v}_L \right) - \left(\frac{\partial \mathbf{v}_G}{\partial t} + (\mathbf{v}_G \cdot \nabla)\mathbf{v}_G \right) \right], \tag{2.18}$$

where C_{VM} is the virtual mass coefficient. Zuber [97] obtained

$$C_{VM} = \frac{1}{2} \frac{1 + 2\epsilon}{1 - \epsilon}. \tag{2.19}$$

The lift force is exerted on a bubble moving in a nonuniform flow field. It is transverse to the direction of motion and is given by

$$\mathbf{f}_L = -\epsilon C_L \rho_L \mathbf{v}_{\text{slip}} \times (\nabla \times \mathbf{v}_L). \tag{2.20}$$

According to Drew and Passman [18], the lift coefficient C_L is equal to 0.25 for dilute flows of spherical bubbles.

Remark 2.3. Whether or not consideration of the lift force is relevant in modeling of bubble columns remains an open question. Some authors [28], [85] had to reverse the sign of (2.20) in order to account for the experimentally well documented fact that bubbles tend to accumulate in the column center if the aeration is uniform. The discrepancy between theory and experiment can be attributed to the lack of a complete understanding of the intricate features of turbulent gas-liquid flow [28]. Sokolichin and Eigenberger criticized the "wrong Magnus force" practice and presented a different explanation of the mechanism driving the bubbles towards the central area [19], [78]. Hence, the lift force apparently awaits further analysis, so it would be premature to consider it in our model.

2.5 Model simplifications

Unabridged two-fluid models are rarely implemented in practice because of the high computational cost they incur. Usually, additional assumptions are made to reduce the model to a form amenable to numerical solution.

Care should be exercised to ensure that no important flow characteristics are lost. A profound study of the range of applicability of various model simplifications was carried out by Eigenberger and Sokolichin [19].

A widespread assumption in multiphase flow simulations is that of phases sharing the same pressure field:

$$p_G = p_G^* = p_L^* = p_L. \tag{2.21}$$

This does not apply to the Rayleigh-Plesset equation where the gas pressure is still governed by the ideal gas law.

Remark 2.4. The effective density of the gas phase can be represented as the product of the average bubble mass and the number density:

$$\tilde{\rho}_G = mn. \tag{2.22}$$

Substituting this expression into equation (2.10) and using (2.3), we obtain

$$\frac{\partial m}{\partial t} + \mathbf{v}_G \cdot \nabla m = -4\pi a^2 \eta \mathcal{N}. \tag{2.23}$$

Thus, it is possible to take a shortcut by tracking m instead of w, a and $\tilde{\rho}_G$. The bubble radius follows from equation (2.6), where ρ_G depends on the common pressure as described by the ideal gas law. We implemented this approach along with the Rayleigh-Plesset model and ascertained that it yields virtually identical numerical results (and at a lower cost). This serves as an evidence of credibility of both formulations.

Since the density of liquid is much greater than that of gas, the inertia and gravity terms in equation (2.12) can be neglected. Furthermore, Eigenberger and Sokolichin have shown that also the virtual mass force is of minor importance [19]. Hence, the drag force plays a dominant role in the interphase momentum transfer. The gas phase momentum balance becomes

$$0 = -\epsilon \nabla p_L - \epsilon C_W \mathbf{v}_{\text{slip}}. \tag{2.24}$$

This yields the following slip relation for the gas phase velocity:

$$\mathbf{v}_G = \mathbf{v}_L + \mathbf{v}_{\text{slip}}, \qquad \mathbf{v}_{\text{slip}} = -\frac{\nabla p_L}{C_W}. \tag{2.25}$$

At low gas throughputs the dynamic pressure field can be approximated by the hydrostatic one, so that the slip velocity is given by

$$\mathbf{v}_{\text{slip}} = -\frac{\nabla p_H}{C_W} = -\frac{\rho_L \mathbf{g}}{C_W} \approx 0.2 \frac{m}{s}\, \mathbf{k}, \tag{2.26}$$

where $\mathbf{k}$ is a vector of unit length directed opposite to $\mathbf{g}$. Eigenberger and Sokolichin deem this approximation adequate for a locally aerated bubble column but not for a uniformly aerated bubble column, since then the radial variation of pressure is crucial to obtaining a correct distribution of gas holdup [19].

If we add equation (2.24) to the liquid phase momentum balance, the interphase force term vanishes and so does the term $-(p_L^* - p_L)\nabla\epsilon$ because of the common pressure assumption. The resulting momentum equation resembles its single-phase counterpart with variable effective density and an extra term due to the interphase mass transfer:

$$\begin{aligned}\tilde{\rho}_L\left(\frac{\partial \mathbf{v}_L}{\partial t} + (\mathbf{v}_L \cdot \nabla)\mathbf{v}_L\right) &= -\nabla p_L + \nabla \cdot (2\tilde{\mu}\mathcal{D}(\mathbf{v}_L)) + \tilde{\rho}_L \mathbf{g} \\ &+ 4\pi a^2 n \eta \mathcal{N} \mathbf{v}_{\text{slip}}. \end{aligned} \tag{2.27}$$

Dependence of the effective density on local gas holdup is responsible for buoyancy effects which lead to circulating flows in the liquid phase. Following Eigenberger and Sokolichin [19], we use an analog of the Boussinesq approximation for natural convection problems and drop the tilde everywhere except for the gravity term. After division by the constant liquid density, we obtain

$$\frac{\partial \mathbf{v}_L}{\partial t} + (\mathbf{v}_L \cdot \nabla)\mathbf{v}_L = -\nabla p + \nabla \cdot (2\nu\mathcal{D}(\mathbf{v}_L)) - \epsilon \mathbf{g} + 4\pi a^2 n \frac{\eta \mathcal{N}}{\rho_L} \mathbf{v}_{\text{slip}}. \tag{2.28}$$

Here ν is the kinematic viscosity of liquid, and

$$p = \frac{p_L - p_{\text{atm}}}{\rho_L} - g(h - \mathbf{k} \cdot \mathbf{x}),$$

where p_{atm} denotes the atmospheric pressure, and h is the reactor height.

The last two terms on the right-hand side of equation (2.28) represent the mechanism by which the gas phase influences the motion of the liquid phase. Bubbles are seen to create a buoyancy force proportional to the gas holdup and directed opposite to the gravitational acceleration. Momentum transfer due to gas absorption will typically be very small and can be omitted.

The modified pressure is implicitly regulated by equation (2.11). Since the density of the liquid phase is constant, we have

$$\begin{aligned}(1-\epsilon)\nabla \cdot \mathbf{v}_L &= 4\pi a^2 n \frac{\eta \mathcal{N}}{\rho_L} + \left(\frac{\partial \epsilon}{\partial t} + \mathbf{v}_L \cdot \nabla \epsilon\right) \\ &= 4\pi a^2 n \frac{\eta \mathcal{N}}{\rho_L} - \mathbf{v}_{\text{slip}} \cdot \nabla \epsilon + \left(\frac{\partial \epsilon}{\partial t} + \mathbf{v}_G \cdot \nabla \epsilon\right). \end{aligned} \tag{2.29}$$

Relation for the material derivative of gas holdup can be readily derived using equations (2.2), (2.3) and (2.8):

$$\begin{aligned}\frac{\partial \epsilon}{\partial t} + \mathbf{v}_G \cdot \nabla \epsilon &= \frac{4}{3}\pi a^3 \left(\frac{\partial n}{\partial t} + \mathbf{v}_G \cdot \nabla n\right) + 4\pi a^2 n \left(\frac{\partial a}{\partial t} + \mathbf{v}_G \cdot \nabla a\right) \\ &= -\epsilon \nabla \cdot \mathbf{v}_G + 4\pi a^2 n \left(w - \frac{\eta \mathcal{N}}{\rho_L}\right).\end{aligned}$$

After substitution into equation (2.29), the mass transfer terms cancel out, and the divergence of the liquid phase velocity is given by

$$\nabla \cdot \mathbf{v}_L = 4\pi a^2 n w - \nabla \cdot (\epsilon \mathbf{v}_{\text{slip}}). \tag{2.30}$$

The terms on the right-hand side take account of the fact that for a dynamic simulation the total volume of the gas-liquid mixture may vary with time. Hence, the upper surface of liquid is not fixed, and its position must be determined by solving a free boundary problem. This stipulates the use of sophisticated numerical algorithms and involves a major computational effort. It is therefore reasonable to replace (2.30) by the standard incompressibility constraint

$$\nabla \cdot \mathbf{v}_L = 0. \tag{2.31}$$

This would eliminate the need for coping with evolution of the free surface, so that the normal component of liquid velocity on top of the bubble column can be set equal to zero. Eigenberger and Sokolichin found that (2.31) is indeed a good approximation provided the void fraction doesn't change abruptly in the vertical direction. This requirement is obviously violated during the startup of the reactor. However, the gas holdup distribution remains virtually unaffected. After the bubbles reach the top of the reactor and the integral gas holdup in the bubble column stabilizes, pseudo-compressibility hardly has any effect on the flow characteristics [19].

2.6 Bubble path dispersion

It is known that bubbles do not rise straight upwards and exhibit considerable dispersion on the macroscopic scale. It has become customary to model this phenomenon by introducing diffusion-like terms into the gas phase continuity equation. If there is no mass transfer and the gas is incompressible, we have [79]

$$\frac{\partial \epsilon}{\partial t} + \nabla \cdot (\epsilon \mathbf{v}_G) = \frac{\partial}{\partial x_i}\left(D_i \frac{\partial \epsilon}{\partial x_i}\right), \tag{2.32}$$

where D_i are some empirical diffusion coefficients. They are often related to the turbulent eddy viscosity of the liquid phase [19], [28], [85].

However, we have more gas phase variables than our predecessors had. Bubble path dispersion should somehow be incorporated into equations for n, w and a. This can be accomplished if we surmise that the void fraction is transported solely by convection and redefine the gas phase velocity so that the total flux is conserved:

$$\epsilon \mathbf{v}_G = \epsilon(\mathbf{v}_L + \mathbf{v}_{\text{slip}}) - D\nabla\epsilon. \tag{2.33}$$

The slip relation transforms to

$$\mathbf{v}_G = \mathbf{v}_L + \mathbf{v}_{\text{slip}} + \mathbf{v}_{\text{disp}}, \qquad \mathbf{v}_{\text{disp}} = -\frac{D}{\epsilon}\nabla\epsilon. \tag{2.34}$$

Now all dispersive effects are contained in $\mathbf{v}_G$. Precautions should be taken to avoid division by zero in equation (2.34). Alternatively, we may consider a linear dependence of $\mathbf{v}_{\text{disp}}$ on the gas holdup gradient.

2.7 Chemical reactions

The dissolved gas is involved in homogeneous chemical reactions in the liquid phase. Many industrially important examples of gas-liquid reactions can be symbolically written as

$$A + \nu_B B \to \nu_P P + \ldots, \tag{2.35}$$

where A is the dissolved gas, B is the component it reacts with, P is the desired product and ν_B, ν_P are the stoichiometric coefficients. If the reaction is of second order, the mass balances read

$$\frac{\partial \tilde{c}_A}{\partial t} + \nabla\cdot(\tilde{c}_A\mathbf{v}_L) = \nabla\cdot(\tilde{D}_A\nabla c_A) - \tilde{k}_2 c_A c_B + 4\pi a^2 n\mathcal{N}, \tag{2.36}$$

$$\frac{\partial \tilde{c}_B}{\partial t} + \nabla\cdot(\tilde{c}_B\mathbf{v}_L) = \nabla\cdot(\tilde{D}_B\nabla c_B) - \nu_B\tilde{k}_2 c_A c_B, \tag{2.37}$$

$$\frac{\partial \tilde{c}_P}{\partial t} + \nabla\cdot(\tilde{c}_P\mathbf{v}_L) = \nabla\cdot(\tilde{D}_P\nabla c_P) + \nu_P\tilde{k}_2 c_A c_B. \tag{2.38}$$

In the above, c_A, c_B, c_P are the molar concentrations, D_A, D_B, D_P are the diffusion coefficients, k_2 is the reaction rate constant, and the tilde denotes multiplication by the volume fraction of the liquid phase.

If the reactant B is present in excess, its virtually constant concentration can be lumped into $k_1 = k_2 c_B$, and the reaction is said to be a pseudo-first-order one. The transport equations become

$$\frac{\partial \tilde{c}_A}{\partial t} + \nabla \cdot (\tilde{c}_A \mathbf{v}_L) = \nabla \cdot (\tilde{D}_A \nabla c_A) - \tilde{k}_1 c_A + 4\pi a^2 n \mathcal{N}, \quad (2.39)$$

$$\frac{\partial \tilde{c}_P}{\partial t} + \nabla \cdot (\tilde{c}_P \mathbf{v}_L) = \nabla \cdot (\tilde{D}_P \nabla c_P) + \nu_P \tilde{k}_1 c_A. \quad (2.40)$$

Note that the reaction rate constant is a dimensional quantity, and its units depend on the order of the reaction. It was established experimentally that reaction rates increase exponentially with temperature. This empirical dependency is often well fitted by the Arrhenius law

$$k = \mathcal{A} \exp(-E_a/RT), \quad (2.41)$$

where R is the gas constant, and T is the absolute temperature. In the above expression E_a is termed the activation energy, and $\mathcal{A}$ the frequency factor.

2.8 Interphase mass transfer

The mass transfer rate is proportional to the interfacial area exposed and to the difference between concentration of dissolved gas at the interface and in the bulk liquid. The interfacial concentration is assumed to be in equilibrium with the gas pressure

$$p_G = H c_A^*, \quad (2.42)$$

where H is Henry's law coefficient.

Since the gas is pure, there is no resistance to mass transfer on the gas side, only in the liquid. Then the molar flux $\mathcal{N}$ is given by

$$\mathcal{N} = k_L (c_A^* - c_A), \quad (2.43)$$

where k_L is the liquid-side mass transfer coefficient. If the gas dissolves without reacting, we are dealing with physical absorption. The physical mass transfer coefficient k_L^0 is frequently correlated in terms of a dimensionless Sherwood number $Sh = \frac{2ak_L^0}{D_A}$. This number varies with Peclet number Pe, which is the product of Reynolds number $Re = \frac{2a}{\nu}|\mathbf{v}_{\text{slip}}|$ and Schmidt number $Sc = \frac{\nu}{D_A}$. A good source of correlations for Sh is the book by Clift *et al.* [8].

Chemical reactions in the liquid phase can appreciably alter the absorption process. They reduce the reagent's local concentration, thus increasing the concentration gradient and the flux of gas. Three possible situations can be distinguished [76]:

- For very slow chemical reactions, the mass transfer rate differs little from that predicted by the physical absorption theory. As the time proceeds, the liquid becomes saturated with the dissolved but unreacted gas, so that the absorption capacity of the equipment is drastically reduced.
- For an intermediate range of reaction rates, the whole body of liquid is available for reaction. The concentration of dissolved gas in the liquid phase is low, and the rate of solution is proportional to the total liquid holdup in the apparatus.
- For very rapid reactions, the gaseous component is destroyed already in a film adjacent to the gas-liquid interface. The absorption rate is proportional to the total interfacial area rather than to the volume of liquid.

A standard way of modeling correction to the mass transfer coefficient due to chemical reactions is to define an enhancement factor E as follows

$$k_L = Ek_L^0. \tag{2.44}$$

For a first-order irreversible reaction, the well-known film theory yields [9], [76]

$$E = Ha \coth Ha, \tag{2.45}$$

where $Ha = \frac{\sqrt{D_A k_1}}{k_L^0}$ is the Hatta number. For vanishing Hatta numbers, the hyperbolic tangent tends to zero, and E must be computed as a series

$$E = 1 + \frac{1}{3}Ha^2 - \frac{1}{45}Ha^4 + \frac{2}{945}Ha^6 - \frac{1}{4725}Ha^8 + \dots. \tag{2.46}$$

Note that $E = 0$ in the limit of zero reaction. On the other hand, if the reaction is very fast, equation (2.45) implies $E = Ha$, so that the mass transfer coefficient is independent of k_L^0.

In case of second-order chemical reactions, the nonlinear structure of equations complicates obtaining E which can be derived analytically only for a few limiting cases. For an instantaneous irreversible reaction we have

$$E_i = 1 + \frac{D_B c_B}{\nu_B D_A c_A^*}. \tag{2.47}$$

For slow and intermediate reactions, it is necessary to resort to an approximate solution. Van Krevelen and Hoftijzer [45] found that the results of their analysis can be correlated in the form

$$E = M \coth M, \tag{2.48}$$

in which

$$M = Ha\sqrt{\frac{E_i - E}{E_i - 1}}, \qquad Ha = \frac{\sqrt{D_A k_2 c_B}}{k_L^0}.$$

This equation is nonlinear and has to be solved iteratively. Wellek *et al.* [93] proposed a simpler explicit formula for computation of the enhancement factor:

$$\frac{1}{(E-1)^{1.35}} = \frac{1}{(E_i - 1)^{1.35}} + \frac{1}{(E_1 - 1)^{1.35}}, \tag{2.49}$$

where $E_1 = Ha \coth Ha$.

The criterion for validity of the pseudo-first-order approximation (2.39)–(2.40) reads [44]

$$E_i - 1 > 10\ E_1. \tag{2.50}$$

This gives an upper limit for the range of admissible Hatta numbers.

2.9 System of equations

Now we are in a position to assemble a mathematical model for reactive flow in a bubble column. After all simplifications have been introduced, equations assume the following form:

Gas phase variables

$$\frac{\partial n}{\partial t} + \nabla \cdot (n \mathbf{v}_G) = 0, \qquad p_G = \rho_G \frac{R}{\eta} T,$$

$$a\left(\frac{\partial w}{\partial t} + \mathbf{v}_G \cdot \nabla w\right) + \frac{3}{2} w^2 = \frac{1}{\rho_L}\left(p_G - p_H - 4\mu \frac{w}{a} - \frac{2\sigma}{a}\right),$$

$$\frac{\partial a}{\partial t} + \mathbf{v}_G \cdot \nabla a = w - \frac{\eta \mathcal{N}}{\rho_L}, \qquad \epsilon = \frac{4}{3}\pi a^3 n,$$

$$\frac{\partial \tilde{\rho}_G}{\partial t} + \nabla \cdot (\tilde{\rho}_G \mathbf{v}_G) = -4\pi a^2 n \eta \mathcal{N}.$$

Velocity fields

$$\frac{\partial \mathbf{v}_L}{\partial t} + (\mathbf{v}_L \cdot \nabla)\mathbf{v}_L = -\nabla p + \nabla \cdot (2\nu \mathcal{D}(\mathbf{v}_L)) - \epsilon \mathbf{g},$$

$$\nabla \cdot \mathbf{v}_L = 0, \qquad \mathbf{v}_G = \mathbf{v}_L + \mathbf{v}_{\text{slip}} + \mathbf{v}_{\text{disp}}.$$

Concentrations of species

$$\frac{\partial \tilde{c}_A}{\partial t} + \nabla \cdot (\tilde{c}_A \mathbf{v}_L) = \nabla \cdot (\tilde{D}_A \nabla c_A) - \tilde{k}_2 c_A c_B + 4\pi a^2 n \mathcal{N},$$
$$\frac{\partial \tilde{c}_B}{\partial t} + \nabla \cdot (\tilde{c}_B \mathbf{v}_L) = \nabla \cdot (\tilde{D}_B \nabla c_B) - \nu_B \tilde{k}_2 c_A c_B,$$
$$\frac{\partial \tilde{c}_P}{\partial t} + \nabla \cdot (\tilde{c}_P \mathbf{v}_L) = \nabla \cdot (\tilde{D}_P \nabla c_P) + \nu_P \tilde{k}_2 c_A c_B.$$

Remark 2.5. Equations (2.6) and (2.23) can be considered instead of those governing the evolution of w, a and $\tilde{\rho}_G$.

Remark 2.6. For genuinely first-order chemical reactions or second-order reactions in the pseudo-first-order regime, the equations for concentrations of species in the liquid phase should be replaced by (2.39)–(2.40).

In order to complete the problem statement, it is necessary to impose appropriate initial and boundary conditions. Initially the liquid is quiescent and free of bubbles. The normal velocity of liquid is constrained to zero, and no-slip boundary conditions are presently utilized at all boundaries. At the inlet we must prescribe values for n, w, a and $\tilde{\rho}_G$. The inflow gas density is chosen so that the entering bubbles are in equilibrium:

$$p_G = p_H + \frac{2\sigma}{a}, \qquad w = 0.$$

The normal concentration gradients are required to vanish, so that there is no flux of species across the boundaries. The bubble column is operated in a semi-batch mode. This means that the component B is charged all at once prior to the beginning of aeration and is gradually consumed by chemical reaction, while the component A is fed continuously in the form of bubbles. The initial concentration of the reaction product is assumed to be zero.

Chapter 3

DEVELOPMENT OF FINITE ELEMENT SCHEMES FOR FLUID DYNAMICS

3.1 Motivation

A high caliber of numerical methods to be employed is a prerequisite for validation of the mathematical model and reliable simulation of reactive two-phase flow. Computational results are worthless if they are corrupted by non-physical oscillations and/or excessive numerical diffusion. In particular, artificial diffusion is recognized to have a devastating effect on the void fraction distribution in the reactor. Since the hydrodynamic behavior of bubble columns is extremely sensitive to changes in the local gas holdup, its maldistribution may result in qualitatively incorrect flow patterns [19]. In ensuing sections, we describe the finite element schemes which are the cornerstones of the numerical algorithm developed in Chapter 4. The methods are presented in a general format, since their range of application is not limited to bubble column simulations. The performance of the proposed techniques is exemplified by application to benchmark problems.

To give a flavor of computational difficulties connected with simulation of the startup of a bubble column, we draw attention to the fact that the hyperbolic equations for w, a and m are invalid in bubble-free zones. A fictitious domain approach with some artificial initial values specified at the fixed grid nodes would fail because of the susceptibility of our model to non-physical data. Thus, we have to deal with a moving boundary problem of an essentially Lagrangian nature. In light of the above, the free-Lagrange space-time finite element method [35] appears to be a proper choice for the

gas phase equations. It automatically takes into account the evolution of the domain occupied by gas, since the problem is formulated over the associated space-time domain. At the same time, the characteristic orientation of finite elements ensures that no infamous convective effects plague the numerical solution. Local mesh modifications followed by a simplified mass-conserving projection of data are introduced whenever the quality of the unstructured Lagrangian mesh deteriorates. We complement the method by a strategy for inflow/outflow boundary discretization and imposition of boundary conditions in a consistent and mass-conserving fashion [48].

The liquid phase equations can be solved on a structured mesh of quadrilateral elements. The transport of species is dominated by convection, which brings about spurious node-to-node oscillations if the conventional Galerkin formulation is applied. This can be rectified by performing discretization in time prior to that in space and prearranging it to match the high spatial accuracy achieved by the Galerkin method. Donea [12] was the first to propose this procedure known as the Taylor-Galerkin method. A distinct advantage of this approach is the absence of any free or adjustable parameter. The enhanced stability follows naturally from an improved temporal approximation. We select an explicit second-order accurate Taylor-Galerkin scheme and mention some ways to obtain higher temporal accuracy.

Like most other high-order methods, Taylor-Galerkin schemes are prone to producing spurious undershoots and overshoots in proximity to discontinuities. In many cases the wiggles can be tolerated, but in the present context we may end up having negative concentrations, which is clearly unacceptable. Therefore, it is necessary to take appropriate measures, so as to obtain a non-oscillatory and non-diffusive numerical solution. We propose a novel high-resolution finite element scheme which can be traced back to the concepts of flux-corrected transport (FCT), but differs from the existing FEM-FCT methods [53], [54] in that the high-order solution is corrected pointwise. This simplifies implementation and provides a greater freedom in the choice of high and low-order schemes. Mass conservation is enforced by post-processing. The new method is shown to deliver non-oscillatory results even when it is not quite the case for FEM-FCT.

Finally, we present a fractional-step projection method for the Navier-Stokes equations, which is capable of handling an inhomogeneous continuity constraint such as (2.30). The desired velocity field is obtained in three stages: convection step, viscous diffusion step, and projection step. We advocate an implicit treatment for the viscous stress terms and perform projection at the continuous level, which enables us to use an equal-order interpolation for the velocity and pressure.

3.2 Free-Lagrange space-time FEM

3.2.1 Overview

Finite element methods for solving CFD problems can be classified into Eulerian, Lagrangian and Arbitrary Lagrangian-Eulerian (ALE) ones. The Eulerian formulation is based on a fixed mesh and allows strong distortions in the fluid motion. Its drawbacks are the presence of the convective term, which is notoriously difficult to treat numerically, and the limited applicability to problems with free and moving boundaries. In the Lagrangian formulation, the mesh nodes move with the flow. This provides a natural treatment of moving boundaries and interfaces, and no detrimental convective effects occur. However, the mesh can become severely distorted with time, so that at some point calculations may have to be stopped and restarted after remeshing and interpolation of data onto the new grid. To some extent, ALE methods, where a mesh with fixed topology moves with velocity not necessarily equal to the fluid velocity, combine the advantages of the Eulerian and Lagrangian formulations.

Lagrangian ideas have been traditionally utilized in the finite element context by employing the concept of characteristics. This has led to a family of Eulerian-Lagrangian methods (ELM) based on exact transport + projection (see [41] and references therein). Eulerian-Lagrangian localized adjoint methods (ELLAM) [70], [71], [72] using a space-time finite element framework were introduced as a generalization of ELM that conserves mass and systematically incorporates a wide range of boundary conditions. The power of space-time finite elements has also been exploited in the characteristic streamline diffusion (CSD) type methods [30], [31], [40], [56], [83], [84]. This approach consists in organizing the space-time mesh in slabs and taking the basis functions to be discontinuous in time, so that each slab may have a distinct triangulation, e.g. oriented to follow some features of the exact solution. In particular, one may align the element edges along the (approximate) characteristics to obtain a method which is Lagrangian locally in time during one time step. In fact, arbitrary space-time meshes are allowed, and the ALE nature of this method makes it particularly suitable for problems in deforming domains involving moving boundaries and interfaces and/or fluid-structure interaction [31], [83], [84].

If the CSD method is used with matching meshes at slab interfaces, so that the initial configuration of the spatial domain in the current slab is identical to the final configuration in the previous slab [34], [35], [91], [92], a globally Lagrangian method is recovered, and projection errors induced by

the transfer of data between non-matching meshes are eliminated. As mentioned above, this approach may eventually lead to mesh tangling. Hansbo [35] proposed a free-Lagrange method, where the mesh quality is maintained by performing local remeshing followed by a simplified mass-conserving projection of data to the locally modified grid.

The elegance of the free-Lagrange method (and that of other CSD-type methods) was somewhat compromised for problems in typical Eulerian domains, such as a pipe flow with moving objects. For instance, elements with all nodes outside the computational domain used to be dropped, which resulted in a jagged outflow boundary [35]. Similarly, the inflow boundary was handled in some *ad hoc* manner. The implementation of boundary conditions was not addressed in the original paper.

In this section we extend the free-Lagrange method [35] by proposing a technique for inflow/outflow boundary discretization. First, we derive the variational formulation for both divergence and non-divergence forms of the convection-diffusion equation and obtain a conservative finite element scheme with consistently imposed boundary conditions. Next, we outline a strategy for constructing a proper space-time mesh over a two-dimensional domain with inlet/outlet and discuss implementation aspects connected with the assembly of stiffness matrix. Finally, numerical results for convection-diffusion of a step function in the Couette flow between two parallel walls are presented.

3.2.2 Finite element formulation for convection-diffusion

Continuous problem

Consider a variable domain $\Omega(t) \in \mathbf{R}^2$, $0 \leq t \leq T$, with boundary $\Gamma(t)$. The linear convection-diffusion equation may appear in one of two alternative forms. The non-divergence form is given by

$$
\begin{aligned}
&\frac{\partial u}{\partial t} + \mathbf{v} \cdot \nabla u = \epsilon \Delta u \quad \text{in } \mathcal{D} = \bigcup_{t \in (0,T)} \Omega(t), \\
&u = g \quad \text{on } \partial\mathcal{D}_D = \bigcup_{t \in (0,T)} \Gamma_D(t), \\
&-\epsilon \nabla u \cdot \mathbf{n} = h \quad \text{on } \partial\mathcal{D}_N = \bigcup_{t \in (0,T)} \Gamma_N(t), \\
&u = u_0 \quad \text{in } \Omega(0),
\end{aligned}
\tag{3.1}
$$

where $\overline{\Gamma_D \cup \Gamma_N} = \Gamma$, $\Gamma_D \cap \Gamma_N = \emptyset$.

The divergence form is a mass conservation law which reads

$$\begin{aligned}
&\frac{\partial u}{\partial t} + \nabla \cdot (\mathbf{v}u) = \nabla \cdot (\epsilon \nabla u) \quad \text{in } \mathcal{D} = \bigcup_{t\in(0,T)} \Omega(t), \\
&u = g \quad \text{on } \partial\mathcal{D}_D = \bigcup_{t\in(0,T)} \Gamma_D(t), \\
&(\mathbf{v}u - \epsilon\nabla u)\cdot \mathbf{n} = h \quad \text{on } \partial\mathcal{D}_F = \bigcup_{t\in(0,T)} \Gamma_F(t), \\
&u = u_0 \quad \text{in } \Omega(0),
\end{aligned} \tag{3.2}$$

where $\overline{\Gamma_D \cup \Gamma_F} = \Gamma$, $\Gamma_D \cap \Gamma_F = \emptyset$.

Here $\mathbf{v} = \mathbf{v}(\mathbf{x}, t)$ is the velocity field, ϵ is the diffusion coefficient, $\mathbf{n}$ is the outward unit normal to Γ, and the boundary conditions are Dirichlet, Neumann and given total flux on Γ_D, Γ_N and Γ_F, respectively. The choice of the Neumann boundary condition for the non-divergence form as compared to the total flux condition for the divergence form is not essential. These natural boundary conditions can be used interchangeably and even coexist in the same boundary value problem (see numerical examples). The corresponding changes in the variational formulation are straightforward.

The velocity field is assumed to be available, for example, by resorting to an analytical solution or solving the concomitant momentum equations numerically in a parallel manner. For divergence-free velocity fields the conservative and non-conservative formulations are equivalent.

In the case of pure convection, when $\epsilon = 0$, the boundary conditions are prescribed only on the inflow boundary $\Gamma_{\text{in}} = \{\mathbf{x} \in \Gamma : \mathbf{v}\cdot\mathbf{n} < 0\}$:

$$u = g \quad \text{on } \partial\mathcal{D}_{\text{in}} = \bigcup_{t\in(0,T)} \Gamma_{\text{in}}(t). \tag{3.3}$$

In what follows we will assume that $\Gamma_D = \Gamma_{\text{in}}$, which is the case for the majority of practical applications.

The equations above are formulated in the Eulerian form, so that the unknowns are computed at fixed spatial points. In the Lagrangian approach, we track fluid particles identified by their positions $\bar{\mathbf{x}}$ at some reference time $\bar{t}$. The particle paths $\mathbf{x} = \mathbf{x}(\bar{\mathbf{x}}, \bar{t}, t)$ follow characteristic curves defined by the relations

$$\frac{\partial \mathbf{x}}{\partial t} = \mathbf{v}(\mathbf{x}, t), \quad \mathbf{x}(\bar{\mathbf{x}}, \bar{t}, \bar{t}) = \bar{\mathbf{x}}. \tag{3.4}$$

By the chain rule of calculus

$$\frac{\partial \bar{u}}{\partial t} = \frac{\partial u}{\partial t} + \mathbf{v}\cdot\nabla u, \tag{3.5}$$

where $\bar{u}(\bar{\mathbf{x}}, \bar{t}, t) = u(\mathbf{x}, t)$. Thus, the bad-behaved convective term vanishes in the Lagrangian formulation.

Finite element spaces

To introduce the space-time finite element framework for the approximate solution of problems (3.1) and (3.2), let $0 = t_0 < t_1 < t_2 < \ldots < t_N = T$ be a sequence of discrete time levels. Furthermore, let $\Omega_n = \Omega(t_n)$ and $\Omega_{n+1} = \Omega(t_{n+1})$. The space-time slab S_n is defined as the region enclosed between Ω_n, Ω_{n+1} and Σ_n, where Σ_n is the surface described by the boundary $\Gamma(t)$ as t varies between t_n and t_{n+1}. The restriction of the space-time inflow boundary to the time interval $[t_n, t_{n+1}]$ is denoted by $\Sigma_n^{\text{in}} \subseteq \Sigma_n$.

Consider a conforming finite element triangulation $\mathcal{T}_n = \{\tau\}$ of $\Sigma_n^{\text{in}} \cup \Omega_n$ endowed with the function space

$$\bar{V}_n = \{\bar{v} \in C^0(\overline{\Sigma_n^{\text{in}} \cup \Omega_n}) : \bar{v}|_\tau \in P_1(\tau),\ \forall \tau \in \mathcal{T}_n\}. \tag{3.6}$$

Here $C^0(\bar{\Omega})$ designates the space of continuous functions on $\bar{\Omega}$ and $P_i(\tau)$ denotes the set of polynomials of degree i on τ.

The oriented space-time mesh is introduced by the mapping

$$\begin{aligned} &(\mathbf{x}, t) = F_n(\bar{\mathbf{x}}, \bar{t}, t) = (\bar{\mathbf{x}} + (t - \bar{t})\mathbf{v}(\bar{\mathbf{x}}, \bar{t}), t) \\ &(\mathbf{x}, t) \in S_n, \quad (\bar{\mathbf{x}}, \bar{t}) \in \Sigma_n^{\text{in}} \cup \Omega_n. \end{aligned} \tag{3.7}$$

Applying this mapping to the triangulation $\mathcal{T}_n$, we cover the slab S_n with a union of tilted triangular prisms, pyramids and tetrahedra. A practical algorithm for the space-time mesh generation is elaborated below in the subsection devoted to implementation aspects.

The trial function space for the slab S_n is defined as follows

$$V_n = \{v \in C^0(\bar{S}_n) : v(\mathbf{x}, t) = \bar{v}(\bar{\mathbf{x}}, \bar{t}),\ \bar{v} \in \bar{V}_n,\ (\mathbf{x}, t) = F_n(\bar{\mathbf{x}}, \bar{t}, t)\}. \tag{3.8}$$

This yields an approximation which is continuous piecewise-linear in space and discontinuous piecewise-constant in time. Higher-order temporal approximations can also be constructed (see e.g. [31] for a general temporal representation of the solution within a slab).

Variational formulation

It is common knowledge that the conventional Galerkin method lacks stability when applied to convection-diffusion problems with dominating convection. A possible remedy is the streamline diffusion modification of weighting

functions. However, the Lagrangian approach alleviates stability problems, so that a standard finite element discretization in space-time will suffice.

The time-discontinuous Galerkin method for the non-divergence form (3.1) of the convection-diffusion equation can be formulated as follows:

For $n = 0, 1, \ldots, N-1$, find $U \in V_n$ such that

$$\begin{aligned} &\int_{S_n} \left(\frac{\partial U}{\partial t} + \mathbf{v} \cdot \nabla U \right) w \, dxdydt + \int_{S_n} \epsilon \nabla U \cdot \nabla w \, dxdydt \\ &- \int_{\Sigma_n^D} \epsilon \nabla U \cdot \mathbf{n} \, w \, dS - \int_{\Sigma_n^D} \mathbf{v} \cdot \mathbf{n} \, (U - g) w \, dS \\ &+ \int_{\Sigma_n^N} hw \, dS + \int_{\Omega_n} (U_+^n - U_-^n) w_+^n \, dxdy = 0, \quad \forall \, w \in V_n. \end{aligned} \tag{3.9}$$

At the time level t_n, there are two grids: one valid immediately before t_n and the other immediately after. U_-^n and U_+^n denote the solution on the meshes before and after t_n, respectively. The computations start with $U_-^0 = u_0$. Similarly, for the weighting functions we have $w_\pm^n = \lim_{s \to 0\pm} w(t_n + s)$. The data is transported from one slab to the next via a built-in L_2-projection in the jump term

$$\int_{\Omega_n} (U_+^n - U_-^n) w_+^n \, dxdy.$$

This term is rather expensive to compute for arbitrary non-matching meshes. However, in the free-Lagrange method the meshes are modified locally and only when absolutely necessary (see below). The transfer of data is achieved by a simplified mass-conserving projection, and mass lumping can be used to reduce the computational cost [33], [35].

The boundary conditions are Dirichlet on Σ_n^D and Neumann on Σ_n^N, where $\overline{\Sigma_n^D \cup \Sigma_n^N} = \Sigma_n$ and $\Sigma_n^D \cap \Sigma_n^N = \emptyset$. Note that the essential boundary conditions are imposed weakly, see e. g. Johnson ([39], p. 178). The corresponding integral plays a role analogous to that of the jump term, with the only difference that it transports boundary data rather than the solution from the top of the previous slab. Conversely, the jump term can be interpreted as a weak form of the inlet boundary condition $u = U_-^n$ on Ω_n with $\mathbf{v} \cdot \mathbf{n} = -1$, where $\mathbf{v} = (v_x, v_y, 1)$ and $\mathbf{n} = (0, 0, -1)$ are the space-time velocity and normal at the bottom of the slab.

The characteristic orientation of our space-time finite element mesh implies that functions from V_n are constant in time along characteristics. Thus, the convective derivative entering the first integral in the weak formulation (3.9) vanishes, and the problem simplifies substantially. In fact, if the characteristics are not followed exactly, there will be some residual convection, but it is assumed to be negligible.

In much the same way, we can derive the variational formulation for the divergence form (3.2) of the convection-diffusion equation. Integration by parts on the space-time slab S_n yields

$$\int_{S_n} \left(\frac{\partial U}{\partial t} + \nabla \cdot (\mathbf{v}U) \right) w \, dxdydt = - \int_{S_n} U \left(\frac{\partial w}{\partial t} + \mathbf{v} \cdot \nabla w \right) dxdydt$$
$$+ \int_{\Omega_{n+1}} Uw \, dxdy + \int_{\Sigma_n} \mathbf{v} \cdot \mathbf{n} \, Uw \, dS - \int_{\Omega_n} Uw \, dxdy.$$

Integrating by parts also the diffusion term, we obtain the following discrete problem:

For $n = 0, 1, \ldots, N-1$, find $U \in V_n$ such that

$$- \int_{S_n} U \left(\frac{\partial w}{\partial t} + \mathbf{v} \cdot \nabla w \right) dxdydt + \int_{S_n} \epsilon \nabla U \cdot \nabla w \, dxdydt$$
$$+ \int_{\Sigma_n^D} (\mathbf{v}g - \epsilon \nabla U) \cdot \mathbf{n} \, w \, dS + \int_{\Sigma_n^F} hw \, dS \tag{3.10}$$
$$+ \int_{\Omega_{n+1}} Uw \, dxdy - \int_{\Omega_n} U_-^n w_+^n \, dxdy = 0, \quad \forall \, w \in V_n.$$

Dirichlet boundary conditions are prescribed on Σ_n^D, and the total flux is given on Σ_n^F, where $\overline{\Sigma_n^D \cup \Sigma_n^F} = \Sigma_n$ and $\Sigma_n^D \cap \Sigma_n^F = \emptyset$. The first integral in (3.10) will vanish due to the characteristic orientation of space-time elements.

An important property of this method is mass conservation. Indeed, the weighting functions are set up so that their sum is identically 1 on S_n. Consequently, when equations (3.10) are summed, we obtain a statement of mass conservation

$$\int_{\Omega_{n+1}} U \, dxdy = \int_{\Omega_n} U_-^n \, dxdy - \int_{\Sigma_n} (\mathbf{v}U - \epsilon \nabla U) \cdot \mathbf{n} \, dS, \tag{3.11}$$

which represents the balance of fluxes through the surface of the space-time volume S_n. The mass at $t = t_{n+1}$ is equal to the mass at $t = t_n$ augmented by the net influx of mass across the boundary.

3.2.3 Implementation aspects

Model problem

In order to assess the performance of the method and elucidate some relevant implementation details, we consider a model problem of the Couette flow in

the rectangle $0 < x < X$, $0 < y < Y$. The parabolic velocity profile is given by

$$v_x = 0, \quad v_y = v_{\max}\left[1 - \left(\frac{2x - X}{X}\right)^2\right], \tag{3.12}$$

where $v_{\max}$ is the maximum velocity, which is attained at $x = X/2$.

The inflow boundary is defined by $x_L \le x \le x_R$, $y = 0$, where $0 \le x_L < x_R \le X$. In the examples below, we use $X = 4$, $Y = 6$, $x_L = 1$, $x_R = 3$ and $v_{\max} = 1$. Initially the spatial domain of interest is an empty set, but it evolves in time advancing toward the outlet $x_L \le x \le x_R$, $y = Y$. This moving boundary problem will serve as a prototype for the startup of a bubble column.

Local remeshing and projection

At the beginning of each time step, we examine the spatial mesh over Ω_n and modify it where necessary until it is of fair quality. We use the algorithm developed by Hansbo [35], which is outlined below.

Node insertion. If an element side is too long, it is bisected, and the midpoint is connected to the vertices opposing the divided edge, see Figure 3.1 (left). If three element sides are too long, the original element is replaced by four new elements with one element in the interior, see Figure 3.1 (right). The elements that result from this refinement are tested again. The solution values at the new nodes are obtained by interpolation.

Node removal. The criteria for node deletion are the lengths of element sides, the element area, and the minimum angle which should not fall below some prescribed values. If an element fails the test, a node (internal if there is a choice) connected to the shortest element side is removed. The patch of elements to which the node belongs constitutes the polygonal domain ω to be remeshed. Diagonal swapping is used to cut off the sharpest angles from

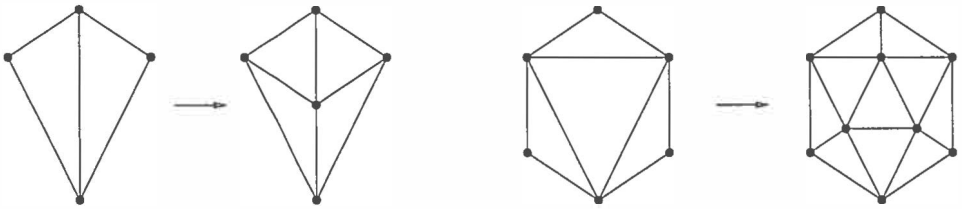

FIGURE 3.1 Insertion of nodes.

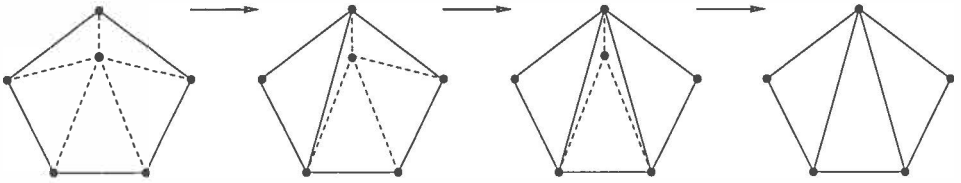

FIGURE 3.2 Removal of an interior node.

the domain until only three triangles remain, see Figure 3.2. Then the node is removed, and the new elements are tested again. If a boundary node has to be removed, adding an artificial element reduces the problem to that for an interior node, see [35] for details.

After the remeshing is complete, it is necessary to transfer data to the new grid. The consistent L_2-projection conserves mass, but it is expensive to carry out. Moreover, it may produce spurious oscillations in the presence of discontinuities. Therefore, local mesh modifications are combined with simplified mass-conserving projections as proposed by Hansbo [33], [35].

Simplified projection. Each element that results from remeshing is assigned a constant mean concentration defined as

$$U_* = \frac{\int_{\omega_-} U_-^n \, dxdy}{\int_{\omega_+} dxdy}, \tag{3.13}$$

where ω_- is the element patch before remeshing, and ω_+ is the element patch after remeshing. Note that ω_- is generally different from ω_+, for instance, when we clip or fill corners at the moving boundary. In this case, we may observe a local rise or fall of concentration near the boundary, since the same mass is spread over a domain smaller (larger) than the original one. An alternative approach would be to have an integral over ω_- in the denominator. Here we face a tradeoff between mass distribution and conservation, and we choose to enforce the former for the non-divergence form and the latter for the divergence form of the convection-diffusion equation. If an element over which the solution integral is evaluated is itself a product of remeshing, then its contribution equals the associated mean concentration times the element area.

Further, the free-Lagrange method can be split into the projection step and the solution step as follows. Once all local mesh modifications are made and mean concentrations computed, a mass-conserving $\bar{U} \in \bar{V}_n$ is found by

solving

$$\int_{\Omega_n} \bar{U} w_+^n \, dxdy - \int_{\Sigma_n^D} \mathbf{v}\cdot\mathbf{n}\, \bar{U} w \, dS = \int_{\Omega_n \setminus \Omega_*} U_-^n w_+^n \, dxdy$$
$$- \int_{\Sigma_n^D} \mathbf{v}\cdot\mathbf{n}\, g w \, dS + \int_{\Omega_*} U_* w_+^n \, dxdy, \quad \forall\, w \in \bar{V}_n, \tag{3.14}$$

where Ω_* is the set of remeshed regions. This strategy is applied within a global assembly procedure, so that the left-hand side is assembled to the mass matrix and the right-hand side to the global load vector. Mass lumping is used in order to avoid matrix inversion and obtain a monotone scheme.

With $\bar{U}^n \in \bar{V}_n$ defined on the current mesh, the approximate solution $U \in V_n$ of the convection-diffusion equation must satisfy

$$\int_{S_n} \left(\frac{\partial U}{\partial t} + \mathbf{v}\cdot\nabla U \right) w \, dxdydt + \int_{S_n} \epsilon \nabla U \cdot \nabla w \, dxdydt$$
$$- \int_{\Sigma_n^D} \epsilon \nabla U \cdot \mathbf{n}\, w \, dS - \int_{\Sigma_n^D} \mathbf{v}\cdot\mathbf{n}\, (U - \bar{U}) w \, dS \tag{3.15}$$
$$+ \int_{\Sigma_n^N} h w \, dS + \int_{\Omega_n} (U - \bar{U}) w \, dxdy = 0, \quad \forall\, w \in V_n$$

for the non-divergence form, and

$$- \int_{S_n} U \left(\frac{\partial w}{\partial t} + \mathbf{v}\cdot\nabla w \right) \, dxdydt + \int_{S_n} \epsilon \nabla U \cdot \nabla w \, dxdydt$$
$$+ \int_{\Sigma_n^D} (\mathbf{v}\bar{U} - \epsilon \nabla U)\cdot\mathbf{n}\, w \, dS + \int_{\Sigma_n^F} h w \, dS \tag{3.16}$$
$$+ \int_{\Omega_{n+1}} U w \, dxdy - \int_{\Omega_n} \bar{U} w \, dxdy = 0, \quad \forall\, w \in V_n$$

for the divergence form.

Space-time mesh generation

Inflow boundary. The space-time inlet Σ_n^{in} for the slab S_n is the rectangle $x_L \le x \le x_R$, $y = 0$, $t_n \le t \le t_{n+1}$. For simplicity, assume a uniform spatial grid of N_x elements with increment $\Delta x = \frac{x_R - x_L}{N_x}$

$$x_i = x_L + i\Delta x, \quad i = 0, 1, \ldots, N_x.$$

In order to prevent generation of excessively large elements, we discretize the inflow boundary also in time. Let $\nu = \left[v_{\text{in}} \frac{\Delta t}{\Delta x} \right]$ be the integer part of

the inflow Courant number, where v_{in} is the average velocity on the inflow boundary and $\Delta t = t_{n+1} - t_n$ is the time step. Then $[t_n, t_{n+1}]$ is partitioned into $N_t = \max\{1, \nu\}$ intervals as follows

$$t_j = t_n + \frac{j}{N_t}\Delta t, \quad j = 0, 1, \ldots, N_t.$$

This yields a Cartesian grid of $N_x \times N_t$ rectangular elements. The triangulation is completed by inserting diagonals. We choose to draw both diagonals in order to preserve symmetry, see Figure 3.5 (bottom).

Top mesh. The nodes of triangulation $\mathcal{T}_n$ covering $\Sigma_n^{\text{in}} \cup \Omega_n$ are advanced along the characteristics to define a top mesh with nodal coordinates

$$\begin{aligned} x_i &= \bar{x}_i + (t_{n+1} - \bar{t}_i) v_x(\bar{x}_i, \bar{y}_i, \bar{t}_i), \\ y_i &= \bar{y}_i + (t_{n+1} - \bar{t}_i) v_y(\bar{x}_i, \bar{y}_i, \bar{t}_i), \\ t_i &= t_{n+1}. \end{aligned} \tag{3.17}$$

The mesh connectivity remains the same as for $\mathcal{T}_n$. Because of substantial element stretching in the Couette flow, the effect of remeshing is pronounced.

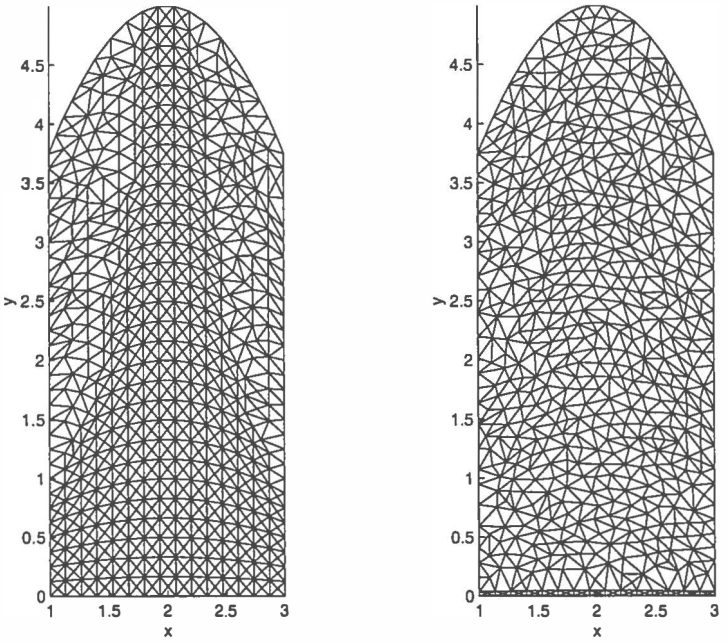

FIGURE 3.3 The top mesh for $t = 5$ and $\Delta t = 0.5$ (left), $\Delta t = 0.05$ (right).

Unless the time step is too small, acceptable elements are generated at the inlet, see Figure 3.3 (left). We see that elements in the central area are intact, but observe regions of vigorous remeshing closer to the walls. Even if the time step is too small, remeshing on the bottom mesh cures the situation, and at most one layer of slender triangles is produced next to the inflow boundary on the top mesh, see Figure 3.3 (right).

The bottom mesh will always be of reasonable quality owing to remeshing. However, the top mesh may tangle if the time step is too large and the velocity field is nonsmooth. Therefore, it is necessary to design a mechanism for control of mesh distortion. Consider an element $\bar{T}$ of triangulation spanning Ω_n and its image T belonging to the top mesh. Let the node numbers be i, j and k. The signed area of a triangle is introduced by the relation [68]

$$\mathcal{A}(T) = \frac{1}{2} \begin{vmatrix} 1 & 1 & 1 \\ x_i & x_j & x_k \\ y_i & y_j & y_k \end{vmatrix}. \tag{3.18}$$

The determinant is positive if the nodes are traversed counterclockwise and negative if the opposite holds. No mesh tangling occurs as long as

$$\mathcal{A}(T) \times \mathcal{A}(\bar{T}) > 0. \tag{3.19}$$

If this criterion is violated for any element, we dispose of the newly generated mesh over the slab inlet and repeat the procedure with a smaller time step. Alternatively, a local or global velocity smoothing can be applied.

Outflow boundary. The top mesh defined by (3.17) may cover a larger domain than Ω_{n+1}. Then the line $y = Y$ splits some elements into two triangles or a triangle and a quadrilateral. In the latter case, we choose the shorter diagonal to divide the quadrilateral into two triangles. This yields a top mesh consisting of an interior triangulation covering Ω_{n+1} and an exterior triangulation with nodes outside the spatial domain, see Figure 3.4 (left). The new nodes are backtracked along characteristics to the time level t_n, and their images in Ω_n and corresponding elements are added to the bottom mesh.

The decomposition of triangulation into the interior and exterior ones may produce poor elements in proximity to the outflow boundary. If this happens, we invoke local remeshing to restore the mesh quality, see Figure 3.4 (right). At that the line $y = Y$ on the top mesh is treated as an internal interface. To remove a node on that line, we add an artificial node with the same coordinates. The original node turns its elements belonging

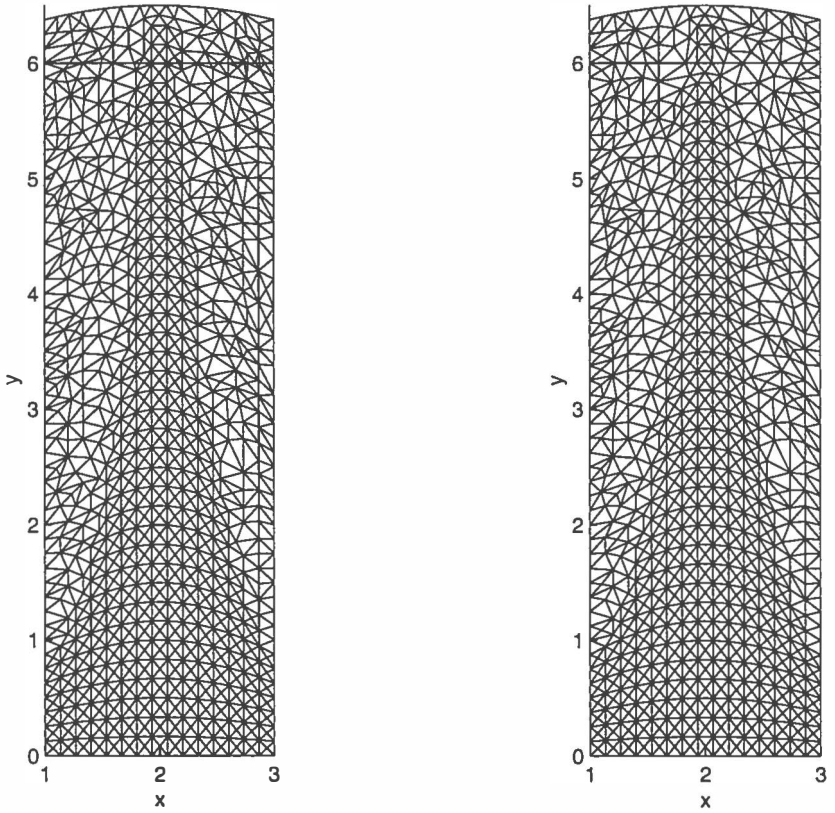

FIGURE 3.4 Outflow boundary fitting, $t = 10,\ \Delta t = 0.5$.

to the exterior triangulation over to the artificial node and keeps those belonging to the interior triangulation. Next, each node receives an artificial element and can be removed as an internal node. Remeshing applies both to the top mesh and to the bottom mesh.

Finally, we put the nodes of exterior triangulation back where they belong, and namely on the space-time outflow boundary Σ_n^{out}, by means of the following coordinate transformation

$$\begin{aligned} t_i &= \bar{t}_i + (Y - \bar{y}_i)/v_y(\bar{x}_i, \bar{y}_i, \bar{t}_i), \\ x_i &= \bar{x}_i + (t_i - \bar{t}_i)v_x(\bar{x}_i, \bar{y}_i, \bar{t}_i), \\ y_i &= Y. \end{aligned} \tag{3.20}$$

This completes the process of space-time mesh generation. The surface meshes for $t = 10,\ \Delta t = 0.5$ are displayed in Figure 3.5. The triangulations of $\Sigma_n^{\text{in}} \cup \Omega_n$ and $\Omega_{n+1} \cup \Sigma_n^{\text{out}}$ are connected by joining the associated

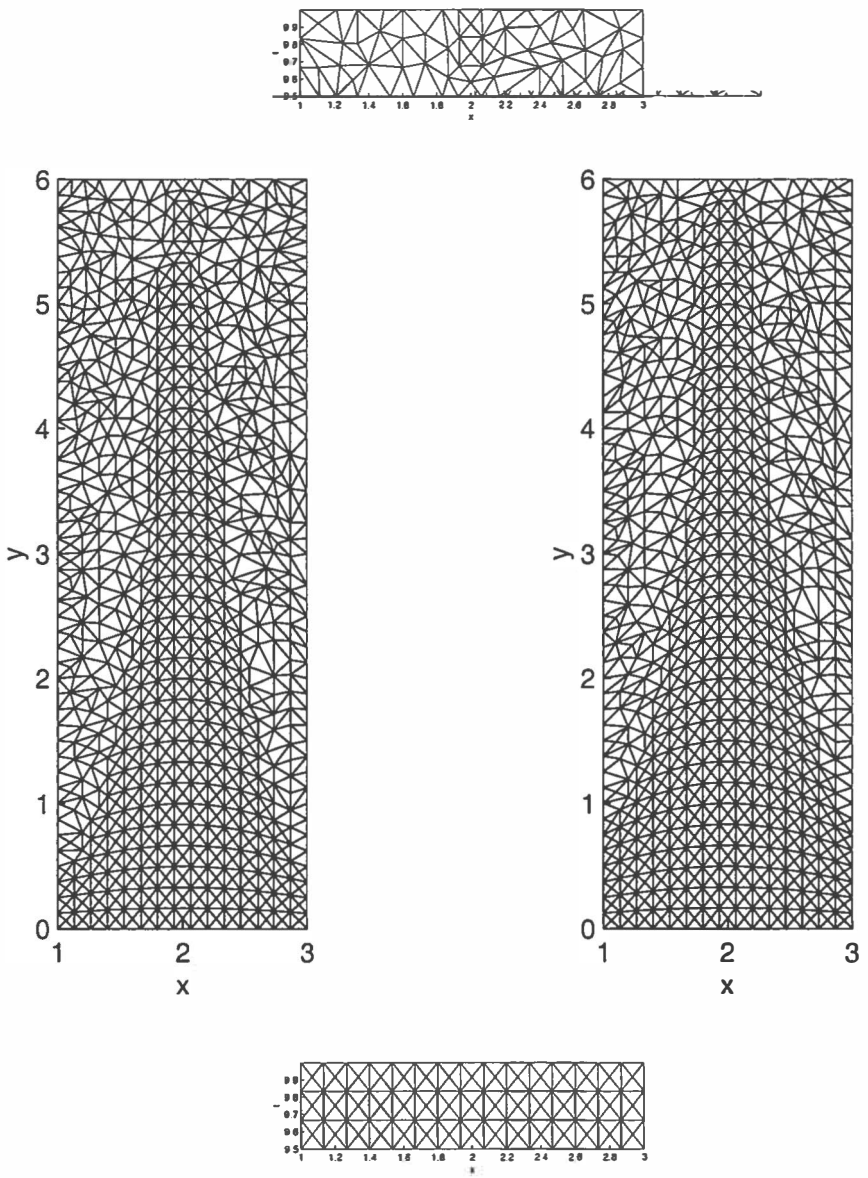

FIGURE 3.5 Triangulation of the slab surface: inlet mesh (bottom), bottom mesh (left), top mesh (right) and outlet mesh (top).

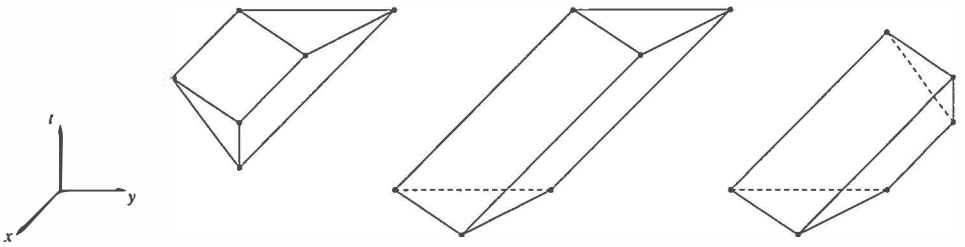

FIGURE 3.6 Space-time finite elements.

nodes $(\bar{x}_i, \bar{y}_i, \bar{t}_i)$ and (x_i, y_i, t_i), which yields the desired three-dimensional mesh over the slab S_n. Some typical space-time finite elements that arise are sketched in Figure 3.6. The six-node inflow (left) and outflow (right) elements may degenerate into pyramids or tetrahedra. The geometry of interior elements (middle) is the same as for standard CSD-type methods.

Stiffness matrix assembly

Following a common practice in finite element computations, we map the space-time finite elements to their reference counterparts and introduce local coordinate systems. The stiffness matrix is assembled element-by-element with integration performed on the reference elements rather than on the deformed physical ones.

All elements in Figure 3.6 are topologically equivalent and are transformed to a unit right triangular prism, see Figure 3.7 (left). Pyramids and tetrahedra are mapped to those shown in Figure 3.7 (middle and right, respectively). The plane $\tau = 0$ corresponds to the elements of triangulation $\mathcal{T}_n$ of $\Sigma_n^{\text{in}} \cup \Omega_n$. The local basis functions have the same form for all three

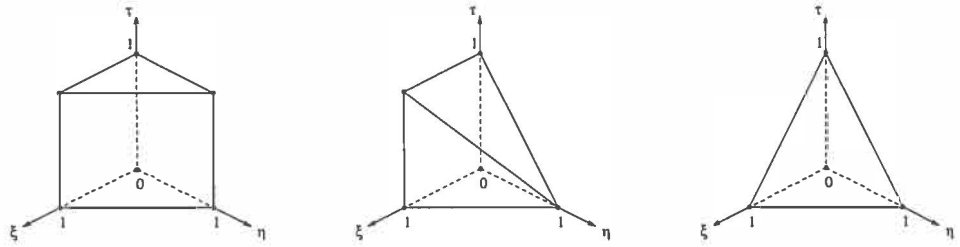

FIGURE 3.7 Reference elements.

types of reference elements, and namely

$$\hat{\varphi} = \begin{bmatrix} 1-\xi-\eta \\ \xi \\ \eta \end{bmatrix}. \tag{3.21}$$

Note that $\hat{\varphi}_i$ are independent of τ which implies that the global basis functions are constant in time along the characteristics.

Consider a transformation

$$F(\xi,\eta,\tau) = \sum_i (x_i, y_i, t_i)\psi_i(\xi,\eta,\tau), \quad (\xi,\eta,\tau) \in \hat{K}, \tag{3.22}$$

where $\hat{K}$ is the reference element, (x_i, y_i, t_i) are the nodal coordinates on the physical element K, and ψ_i are the mapping functions which depend on the element type as given by

$$\psi_{TP} = \begin{bmatrix} (1-\xi-\eta)(1-\tau) \\ \xi(1-\tau) \\ \eta(1-\tau) \\ (1-\xi-\eta)\tau \\ \xi\tau \\ \eta\tau \end{bmatrix}; \qquad \psi_P = \begin{bmatrix} (1-\xi)(1-\tau)-\eta \\ \xi(1-\tau) \\ \eta \\ (1-\xi)\tau \\ \xi\tau \end{bmatrix};$$

$$\psi_T = \begin{bmatrix} 1-\xi-\eta-\tau \\ \xi \\ \eta \\ \tau \end{bmatrix} \tag{3.23}$$

for the triangular prism, the pyramid and the tetrahedron, respectively. Then we have

$$K = F(\hat{K}) = \{(x,y,t) \in \mathbf{R}^3 : (x,y,t) = F(\xi,\eta,\tau),\ (\xi,\eta,\tau) \in \hat{K}\}.$$

The entries of the element stiffness matrix are

$$a_{ij}^K = \int_K \epsilon\ \nabla\varphi_i \cdot \nabla\varphi_j\ dxdydt, \quad i,j = 1,2,3. \tag{3.24}$$

By the chain rule

$$\nabla\varphi_i = \begin{bmatrix} \frac{\partial}{\partial x} \\ \frac{\partial}{\partial y} \end{bmatrix} \varphi_i = \begin{bmatrix} \frac{\partial\xi}{\partial x} & \frac{\partial\eta}{\partial x} \\ \frac{\partial\xi}{\partial y} & \frac{\partial\eta}{\partial y} \end{bmatrix} \begin{bmatrix} \frac{\partial}{\partial\xi} \\ \frac{\partial}{\partial\eta} \end{bmatrix} \hat{\varphi}_i = D\hat{\nabla}\hat{\varphi}_i. \tag{3.25}$$

The Jacobian of the mapping and its inverse are given by

$$J = \begin{bmatrix} \frac{\partial x}{\partial \xi} & \frac{\partial x}{\partial \eta} & \frac{\partial x}{\partial \tau} \\ \frac{\partial y}{\partial \xi} & \frac{\partial y}{\partial \eta} & \frac{\partial y}{\partial \tau} \\ \frac{\partial t}{\partial \xi} & \frac{\partial t}{\partial \eta} & \frac{\partial t}{\partial \tau} \end{bmatrix} = \begin{bmatrix} \sum_i \frac{\partial \psi_i}{\partial \xi} x_i & \sum_i \frac{\partial \psi_i}{\partial \eta} x_i & \sum_i \frac{\partial \psi_i}{\partial \tau} x_i \\ \sum_i \frac{\partial \psi_i}{\partial \xi} y_i & \sum_i \frac{\partial \psi_i}{\partial \eta} y_i & \sum_i \frac{\partial \psi_i}{\partial \tau} y_i \\ \sum_i \frac{\partial \psi_i}{\partial \xi} t_i & \sum_i \frac{\partial \psi_i}{\partial \eta} t_i & \sum_i \frac{\partial \psi_i}{\partial \tau} t_i \end{bmatrix}$$

and

$$J^{-1} = \begin{bmatrix} \frac{\partial \xi}{\partial x} & \frac{\partial \xi}{\partial y} & \frac{\partial \xi}{\partial t} \\ \frac{\partial \eta}{\partial x} & \frac{\partial \eta}{\partial y} & \frac{\partial \eta}{\partial t} \\ \frac{\partial \tau}{\partial x} & \frac{\partial \tau}{\partial y} & \frac{\partial \tau}{\partial t} \end{bmatrix}.$$

Hence,

$$D = \frac{1}{\det J} \begin{bmatrix} J_{22}J_{33} - J_{23}J_{32} & J_{23}J_{31} - J_{21}J_{33} \\ J_{13}J_{32} - J_{12}J_{33} & J_{11}J_{33} - J_{13}J_{31} \end{bmatrix} = \frac{1}{\det J} D_*.$$

Finally, the matrix elements can be computed by evaluating integrals over the reference element $\hat{K}$:

$$a_{ij}^K = \int_{\hat{K}} \epsilon \, (D_* \hat{\nabla} \hat{\varphi}_i) \cdot (D_* \hat{\nabla} \hat{\varphi}_j) \frac{1}{|\det J|} \, d\xi d\eta d\tau, \quad i,j = 1,2,3. \tag{3.26}$$

Relation (3.25) is also used to obtain the diffusive flux at quadrature points when computing the corresponding boundary integral.

3.2.4 Numerical examples

We apply the free-Lagrange method to the model problem with a time-dependent Dirichlet boundary condition

$$g = \begin{cases} 2, & 5 \le t \le 8, \\ 1, & \text{otherwise} \end{cases} \tag{3.27}$$

at the inlet, the homogeneous Neumann boundary condition at the outlet and the vanishing total flux condition on the rest of the boundary. Since the velocity field is divergence-free, the two forms of the convection-diffusion equation are equivalent, and we choose the conservative formulation.

Figure 3.8 plots the solution values at $t = 10$ over the top mesh. The upper subplots correspond to pure convection of the step function, while the lower ones show the effect of diffusion with $\epsilon = 5 \times 10^{-3}$.

The approximate solution produced by the free-Lagrange method (left) is compared to that obtained by a purely Lagrangian method (right) where

remeshing is only done to fit triangulation to the outflow boundary. The comparison indicates that frequent remeshing with a lumped-mass piecewise-constant simplified projection may introduce significant amounts of artificial diffusion into the numerical scheme. In some cases this feature may turn out to be beneficial, e.g. by providing a natural and efficient shock capturing [32]. However, if artificial diffusion is undesirable, it is prudent to consider employing alternative projection schemes [33], [35].

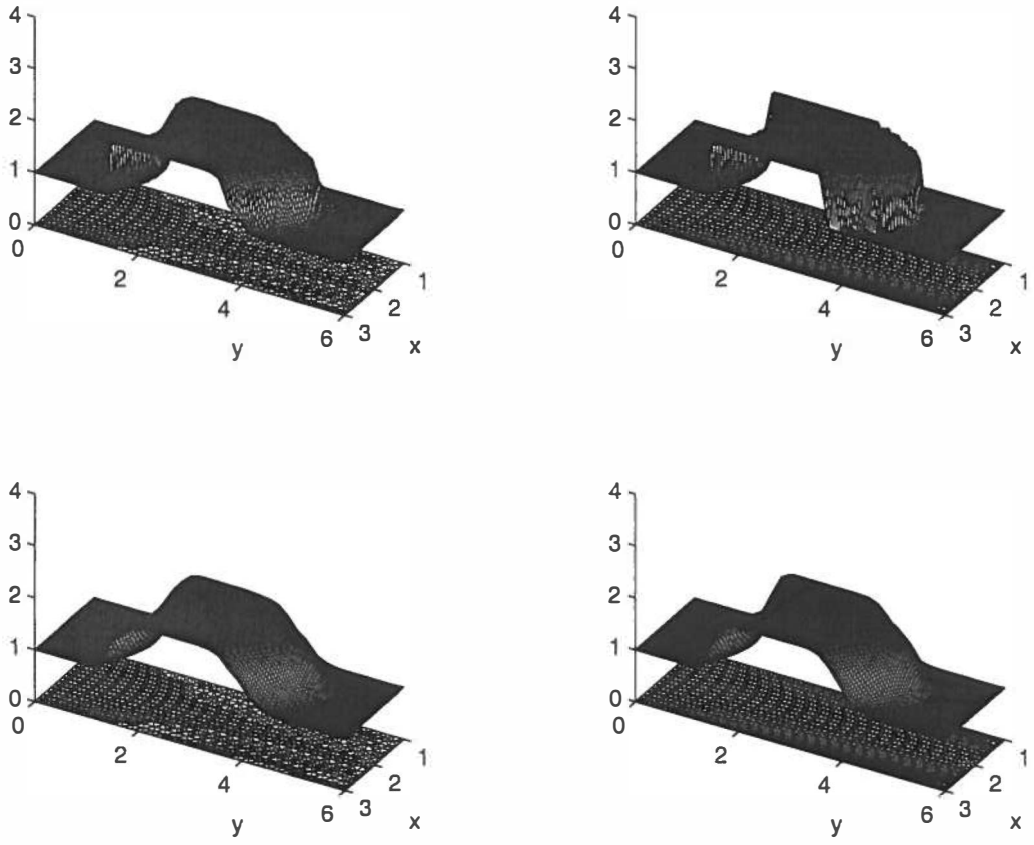

FIGURE 3.8 Pure convection (top) and convection-diffusion (bottom) with (left) and without (right) remeshing.

3.3 High-resolution finite element schemes: PCT versus FCT

3.3.1 Overview

The pioneering concept of flux-corrected transport (FCT) was introduced by Boris and Book in their renowned paper [4], which has paved the way for development of a whole class of high-resolution methods for convection-dominated problems. The essence of flux limiting is the replacement of a formally high-order method by a monotone low-order method in proximity to discontinuities, where spurious undershoots and overshoots are likely to arise. The resulting numerical solution is monotonicity-preserving and exhibits a sharp resolution of shocks and contact discontinuities.

The original method of Boris and Book was formulated in the finite difference context, and its range of application was limited to one-dimensional problems. Zalesak [95] generalized FCT to the multidimensional case and proposed a strategy for alleviating peak clipping inherent in the original one-dimensional flux limiter. In the finite element framework, flux correction was first applied by Parrott and Christie [59]. The potential of FCT was further exploited by Löhner *et al.* [53], [54] who extended it to what is known as the finite element methodology for flux-corrected transport (FEM-FCT) suitable for implementation on completely unstructured grids in combination with adaptive mesh refinement techniques.

Conventional FCT schemes rest on the assumption that the difference between the low-order solution and the high-order solution can be represented as a sum of fluxes (element contributions). In this section, we show that it is possible to waive this requirement and still guarantee mass conservation, which is crucial to a correct propagation of shocks. The new algorithm involves a pointwise correction of the high-order solution rather than manipulations with fluxes or element contributions. Hence, we call this method *pointwise-corrected transport* (PCT) to distinguish it from FEM-FCT. Mass conservation is enforced by applying a straightforward post-processing technique. The low-order scheme is used only to determine weights during the restoration of lost mass. Hence, the high and low-order schemes can be chosen arbitrarily, so that more stable and accurate combinations of methods can be considered. Another advantage of PCT is that it enables us to employ a sharper estimate for the range of admissible solution values. Last but not least, PCT appears to simplify bookkeeping and offer considerable savings in storage as compared to FEM-FCT. The presented numerical results for one and two-dimensional benchmark problems compare favorably

with those obtained by a FEM-FCT method.

3.3.2 High and low-order schemes

Consider a domain Ω with boundary Γ. Let a scalar quantity u be transported by a prescribed velocity field $\mathbf{v} = \mathbf{v}(\mathbf{x})$. The pure convection equation reads

$$u_t + \mathbf{v} \cdot \nabla u = 0 \quad \text{in } \Omega. \tag{3.28}$$

If the problem of interest contains other spatial differential operators, the above equation becomes an integral part of a fractional-step method (see the next chapter). The concomitant Dirichlet boundary condition is

$$u = g \quad \text{on } \Gamma_{\text{in}}, \tag{3.29}$$

where g is a known function, and $\Gamma_{\text{in}} = \{\mathbf{x} \in \Gamma : \mathbf{v} \cdot \mathbf{n} < 0\}$ denotes the inflow boundary, $\mathbf{n}$ being the outward unit normal to Γ. No boundary condition is imposed on the outflow boundary $\Gamma_{\text{out}} = \Gamma \backslash \Gamma_{\text{in}}$. The initial distribution of u in Ω is given by

$$u = u^0 \quad \text{at } t = 0. \tag{3.30}$$

A good candidate for the high-order scheme is a one-step Taylor-Galerkin method which was labeled the Lax-Wendroff finite element scheme (LWFE) by Donea *et al.* [16]. First, the spatial variables are left continuous, and equation (3.28) is discretized in time using a Taylor series expansion in the time step $\Delta t = t_{n+1} - t_n$ up to the second order

$$u^{n+1} = u^n + \Delta t\, u_t^n + \frac{1}{2}(\Delta t)^2 u_{tt}^n + \mathcal{O}[(\Delta t)^3]. \tag{3.31}$$

The first-order time derivative is provided directly by (3.28), whereas the second-order derivative can be obtained by differentiating the governing equation as follows:

$$u_{tt} = -\mathbf{v} \cdot \nabla u_t = \mathbf{v} \cdot \nabla(\mathbf{v} \cdot \nabla u).$$

The spatial discretization is performed by the standard Galerkin method. Substituting for temporal derivatives, taking the product with weighting functions w vanishing on the inflow boundary, and integrating over the domain Ω, we obtain the weak formulation

$$\int_\Omega w(u^{n+1} - u^n)\, d\mathbf{x} = -\Delta t \int_\Omega w\mathbf{v} \cdot \nabla u^n\, d\mathbf{x} + \frac{1}{2}(\Delta t)^2 \int_\Omega w\mathbf{v} \cdot \nabla(\mathbf{v} \cdot \nabla u^n)\, d\mathbf{x}. \tag{3.32}$$

The last term is integrated by parts using the formula

$$\begin{aligned}\int_\Omega w\mathbf{v}\cdot\nabla(\mathbf{v}\cdot\nabla u)\,d\mathbf{x} &= -\int_\Omega \nabla\cdot(w\mathbf{v})\;\mathbf{v}\cdot\nabla u\,d\mathbf{x}+\int_{\Gamma_{\text{out}}} w\mathbf{v}\cdot\mathbf{n}\;\mathbf{v}\cdot\nabla u\,dS\\ &= -\int_\Omega \mathbf{v}\cdot\nabla w\;\mathbf{v}\cdot\nabla u\,d\mathbf{x}-\int_\Omega w\nabla\cdot\mathbf{v}\;\mathbf{v}\cdot\nabla u\,d\mathbf{x}\\ &+ \int_{\Gamma_{\text{out}}} w\mathbf{v}\cdot\mathbf{n}\;\mathbf{v}\cdot\nabla u\,dS, \qquad (3.33)\end{aligned}$$

which follows from the identity

$$\nabla\cdot(a\mathbf{b}) = a\nabla\cdot\mathbf{b}+\mathbf{b}\cdot\nabla a.$$

The integrals catering for the second-order temporal accuracy admit the following interpretation. The most important term is

$$-\frac{1}{2}(\Delta t)^2\int_\Omega \mathbf{v}\cdot\nabla w\;\mathbf{v}\cdot\nabla u^n\,d\mathbf{x}.$$

It introduces streamline diffusion intrinsic to the Lax-Wendroff time discretization. In contrast to the classical streamline upwind method, no artificial parameter needs to be fitted. The term

$$-\frac{1}{2}(\Delta t)^2\int_\Omega w\nabla\cdot\mathbf{v}\;\mathbf{v}\cdot\nabla u^n\,d\mathbf{x}$$

vanishes for divergence-free velocity fields which often occur in practice. Finally, the variationally generated surface integral

$$\frac{1}{2}(\Delta t)^2\int_{\Gamma_{\text{out}}} w\mathbf{v}\cdot\mathbf{n}\;\mathbf{v}\cdot\nabla u^n\,dS$$

precludes the arising of spurious reflections at outflow boundaries for transient calculations [16].

Remark 3.1. Higher-order explicit Taylor-Galerkin schemes can be constructed. A two-step procedure for solution of nonlinear multidimensional hyperbolic problems was proposed by Selmin [75]. His original third-order method culminated in the fourth-order Taylor-Galerkin schemes of Quartapelle and Selmin [63]. A fractional-step strategy was also employed by Safjan and Oden [73]. They introduced a family of high-order semi-implicit Taylor-Galerkin schemes which were used in conjunction with an $h-p$ adaptive finite element method for spatial approximation. These schemes are unconditionally stable and of order $2s$ for s stages. Smolianski and Kuzmin

[77] demonstrated that a yet higher temporal accuracy can be achieved by consideration of additional time layers. Two explicit multilayer schemes were derived, which are of order $3s$ for s stages ($s = 1, 2$). However, for our purposes the second-order LWFE method will do.

The approximate solution at the time level t_n is expressed in the form

$$u^n(\mathbf{x}) = \sum_i U_i^n \varphi_i(\mathbf{x}), \tag{3.34}$$

where $U^n = \{U_i^n\}$ is the vector of nodal values, and $\varphi = \{\varphi_i\}$ is the vector of trial functions. Substituting this expansion into the variational formulation, we obtain the fully discretized equations which can be written in a matrix notation as follows:

$$M_C \Delta U = R, \tag{3.35}$$

in which

$$M_C = \int_\Omega \varphi\varphi^T \, d\mathbf{x}$$

denotes the consistent mass matrix,

$$\Delta U = U^{n+1} - U^n$$

is the vector of nodal increments, and R is assembled from element contributions evaluated at the previous time level. At $t = 0$, we have $U_i^0 = u^0(\mathbf{x}_i)$.

The consistent mass matrix possesses an excellent condition number, which makes attractive the use of iterative techniques. The following multipass procedure is frequently employed [14], [53], [54]

$$M_L \Delta U^{k+1} = R + (M_L - M_C)\Delta U^k, \quad k = 0, 1, \ldots, \quad \Delta U^0 = 0. \tag{3.36}$$

Typically, three iterations will suffice. In the above,

$$M_L = \text{diag}\left\{\int_\Omega \varphi_i \, d\mathbf{x}\right\}$$

is the unique diagonal mass matrix having the conservation property. It is obtained by row-sum lumping which corresponds to numerical integration by a low-order quadrature scheme [33].

The converged solution to problem (3.35) satisfies

$$M_L \Delta U^H = R + (M_L - M_C)\Delta U^H, \tag{3.37}$$

where the superscript H refers to the high-order scheme. We will see shortly that this representation facilitates the computation of antidiffusive element contributions for the FCT method.

Arguing as Löhner *et al.*, we obtain a monotone low-order scheme by introducing an appropriate amount of "mass diffusion" into the lumped-mass LWFE [53], [54]

$$M_L \Delta U^L = R + c_d(M_C - M_L)U^n. \tag{3.38}$$

Here the superscript L denotes the low-order scheme, and c_d is a constant coefficient. The matrix $M_C - M_L$ represents a discrete diffusion operator. Subtracting (3.38) from (3.37) yields

$$\Delta U^H - \Delta U^L = M_L^{-1}(M_L - M_C)(c_d U^n + \Delta U^H). \tag{3.39}$$

This relation gives the difference between the high and low-order solutions, which is assembled element-by-element.

3.3.3 Flux-corrected transport

In this subsection, the standard FEM-FCT procedure is outlined. We adhere to the notation of Löhner *et al.* [53], [54]. The process of flux correction involves the following six algorithmic steps:

1. Compute HEC, the high-order element contributions.
2. Compute LEC, the low-order element contributions.
3. Define AEC, the antidiffusive element contributions, as

$$AEC = HEC - LEC. \tag{3.40}$$

4. Advance the solution in time by the low-order scheme:

$$U_i^L = U_i^n + \sum_{j \in E_i} LEC_j^{(i)}, \quad i = 1, \ldots, N. \tag{3.41}$$

5. Limit the AEC so that the end-of-step solution U^{n+1} is free of extrema not detected in U^L or U^n:

$$\overline{AEC}_j = C_j \times AEC_j, \quad 0 \leq C_j \leq 1. \tag{3.42}$$

6. Apply the corrected AEC to the low-order solution:

$$U_i^{n+1} = U_i^L + \sum_{j \in E_i} \overline{AEC}_j^{(i)}, \quad i = 1, \ldots, N. \tag{3.43}$$

In the above, E_i is the set of elements surrounding node i, and N denotes the total number of nodes.

The ultimate performance of the method is determined by the limiting strategy employed in step 5. The choice $C_j \equiv 1$ yields the high-order solution, whereas for $C_j \equiv 0$ the low-order solution is recovered. The objective is to use the antidiffusive element contributions to the greatest extent possible without generating wiggles. Six auxiliary quantities are defined:

- $P_i^{\pm}$, the sum of all positive (negative) antidiffusive element contributions to node i:
$$P_i^{\pm} = \sum_{j \in E_i} \begin{matrix} \max \\ \min \end{matrix} \{0, AEC_j^{(i)}\}. \tag{3.44}$$

- $Q_i^{\pm}$, the maximum (minimum) admissible increment for node i:
$$Q_i^{\pm} = U_i^{\begin{matrix} \max \\ \min \end{matrix}} - U_i^L, \tag{3.45}$$
where $U_i^{\begin{matrix} \max \\ \min \end{matrix}}$ denotes the maximum (minimum) value that the unknown U_i^{n+1} is allowed to attain (see below).

- $R_i^{\pm}$, defined in terms of $P_i^{\pm}$ and $Q_i^{\pm}$ as follows:
$$R_i^{\pm} = \begin{cases} \min\{1, Q_i^{\pm}/P_i^{\pm}\}, & \text{if } P_i^{+} > 0,\ P_i^{-} < 0, \\ 0, & \text{if } P_i^{\pm} = 0. \end{cases} \tag{3.46}$$

The non-physical undershoots and overshoots produced by the high-order scheme are suppressed if the limiter is conservative enough. For each element, the correction factor C_j is computed as

$$C_j = \min_{k \in N_j} \begin{cases} R_k^{+}, & \text{if } AEC_j^{(k)} \geq 0, \\ R_k^{-}, & \text{if } AEC_j^{(k)} < 0, \end{cases} \tag{3.47}$$

where N_j is the set of element's node numbers. Finally, the admissible solution range is obtained in three steps:

- Take the maximum (minimum) over nodal values of U^L and U^n:
$$U_i^{*} = \begin{matrix} \max \\ \min \end{matrix} \{U_i^L, U_i^n\}. \tag{3.48}$$

- Take the maximum (minimum) over element nodes:
$$U_j^{**} = \begin{matrix} \max \\ \min \end{matrix} U_k^{*}, \quad k \in N_j. \tag{3.49}$$

- Take the maximum (minimum) over elements containing node i:

$$U_i^{\substack{\max \\ \min}} = \underset{\min}{\max} U_j^{**}, \quad j \in E_i. \tag{3.50}$$

This wraps up the general description of the conventional FEM-FCT limiting procedure. Now we proceed to derivation of an alternative formulation.

3.3.4 Pointwise-corrected transport

For the pure convection equation (3.28), the solution at $t = t_{n+1}$ is simply the transported solution at $t = t_n$. We can use this knowledge to obtain a better estimate for $U^{\max}$ and $U^{\min}$. Since the Courant number is restricted by stability considerations, the exact solution will always reside at the previous time level at most one mesh size away. We give up U^L as extrema indicator and search for maxima and minima only in elements located "upwind":

$$U_i^{\substack{\max \\ \min}} = \underset{\min}{\max} U_k^n, \quad k \in N_{upw}. \tag{3.51}$$

At the inflow boundary, both $U^{\max}$ and $U^{\min}$ are set equal to the boundary data. The term "upwind" needs a more precise definition. In the one-dimensional case with positive velocity, the choice is obvious: $[x_{i-1}, x_i]$ will be the upwind element for node i. In multiple dimensions we advance the nodes of each element $j \in E_i$ along the characteristics:

$$\hat{\mathbf{x}}_k = \mathbf{x}_k + \mathbf{v}_k \Delta t, \quad k \in N_j \tag{3.52}$$

and check if the so defined image of the element contains the point with coordinates $\mathbf{x}_i$. If it does, we have found an upwind element. An efficient algorithm exists for determining whether or not a point is inside a given element [52], [60]. Let the coordinates of the point be represented by the formula

$$\mathbf{x}_p = \sum_i \mathbf{x}_i \varphi_i. \tag{3.53}$$

Furthermore, the sum of shape functions should equal unity:

$$\sum_i \varphi_i = 1. \tag{3.54}$$

For triangular elements, the values of local basis functions can be readily computed by solving the following system of equations:

$$\begin{bmatrix} x_1 & x_2 & x_3 \\ y_1 & y_2 & y_3 \\ 1 & 1 & 1 \end{bmatrix} \begin{bmatrix} \varphi_1 \\ \varphi_2 \\ \varphi_3 \end{bmatrix} = \begin{bmatrix} x_p \\ y_p \\ 1 \end{bmatrix}. \tag{3.55}$$

The point belongs to the element if and only if

$$0 \leq \varphi_i \leq 1, \qquad i = 1, 2, 3. \tag{3.56}$$

The easiest way to determine if a point is inside a quadrilateral element is to split it into two triangles and proceed as before.

The limiting process simplifies to

$$\bar{U}_i^H = \min\{U_i^{\max}, \max\{U_i^H, U_i^{\min}\}\}, \quad i = 1, \ldots, N. \tag{3.57}$$

The pointwise-corrected high-order solution $\bar{U}^H$ generally does not conserve mass. This may have disastrous consequences for nonlinear conservation laws (e.g. the Burgers equation), since there is no guarantee that shocks will move with correct speed. Therefore, it is necessary to put the mass back where it belongs, which can be accomplished by a simple post-processing technique devised by Hansbo [35]. The method was originally developed for restoration of mass lost during a non-conserving projection between two arbitrary meshes.

A lumped-mass weighted L_2-projection with conservation imposed as a constraint yields the mass-conserving end-of-step solution U^{n+1} in the form

$$U^{n+1} = \bar{U}^H - \lambda w, \tag{3.58}$$

in which w is the vector of lumped weights, and λ is the Lagrange multiplier computed from

$$\lambda = \frac{m^T(\bar{U}^H - U^L)}{m^T w}, \tag{3.59}$$

where m is the vector of diagonal entries of the lumped mass matrix M_L. The numerator $\Delta m = m^T(\bar{U}^H - U^L)$ represents the total loss or gain of mass. By virtue of (3.58) and (3.59) we have $m^T U^{n+1} = m^T U^L$ no matter what the weights are. Since the low-order solution presumably conserves mass, so does U^{n+1}.

Finally, we address the selection of nodal weights w. It is natural to assign a smaller weight in regions where $\bar{U}^H$ is close to U^L and a greater weight otherwise. We set

$$w_i = \max\{0, \operatorname{sign}(\Delta m) \times (\bar{U}_i^H - U_i^L)^3\}. \tag{3.60}$$

Note that mass is added only where $\bar{U}^H$ is less than U^L and subtracted only where the opposite holds. The difference $\bar{U}_i^H - U_i^L$ is raised to the third power in order to avoid excessive smoothing.

The proposed PCT algorithm can be summarized as follows:

1. Compute U^H, the high-order solution.
2. Compute U^L, the low-order solution.
3. Locate the upwind elements and compute $U_{\min}^{\max}$.
4. Limit the high-order solution pointwise.
5. Restore the lost mass by post-processing.

Remark 3.2. It is not possible to use estimate (3.51) within a FEM-FCT method, since the low-order solution does not necessarily satisfy $U_i^{\min} \leq U_i^L \leq U_i^{\max}$. Thus, U^{n+1} may also fail to do so for any choice of correction factors C_j.

3.3.5 Numerical examples

Convection of a step function

As a simple one-dimensional test problem, consider convection of a step function in the positive direction of the x-axis with unit velocity. We use a uniform mesh of 100 linear elements in the interval $[0, 1]$. The time step is

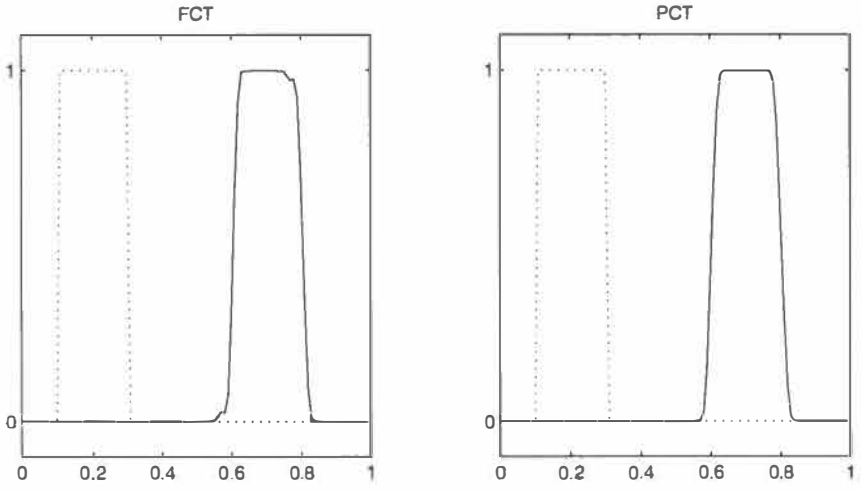

FIGURE 3.9 Convection of a step function. Initial data and solution at $t = 0.5$.

chosen so that the Courant number ν equals 0.2. The initial profile (dotted) and numerical solutions at $t = 0.5$ are shown in Figure 3.9. Both FEM-FCT (left) and PCT (right) yield accurate non-diffusive results. However, the former method produces slight oscillations in the upper right and lower left corners. The ripples are due to the spurious local extrema that the FCT limiter fails to detect because they do not violate the solution bounds given by (3.48)–(3.50). In the one-dimensional case, the wiggles can be eliminated by invoking Zalesak's preprocessing of antidiffusive fluxes ([95], eq. (14)).

Burgers equation

A standard model problem for nonlinear convection in one dimension is the inviscid Burgers equation

$$u_t + uu_x = 0. \tag{3.61}$$

The employed mesh and time step are the same as in the previous example. The initial data and results for the FCT and PCT methods at $t = 0.4$ are depicted in Figure 3.10. Again, a small residual wiggle is observed in the FCT solution, while the PCT solution is completely free of oscillations. In either case, the shock is seen to propagate with correct speed, which is due to the fact that both formulations are conservative.

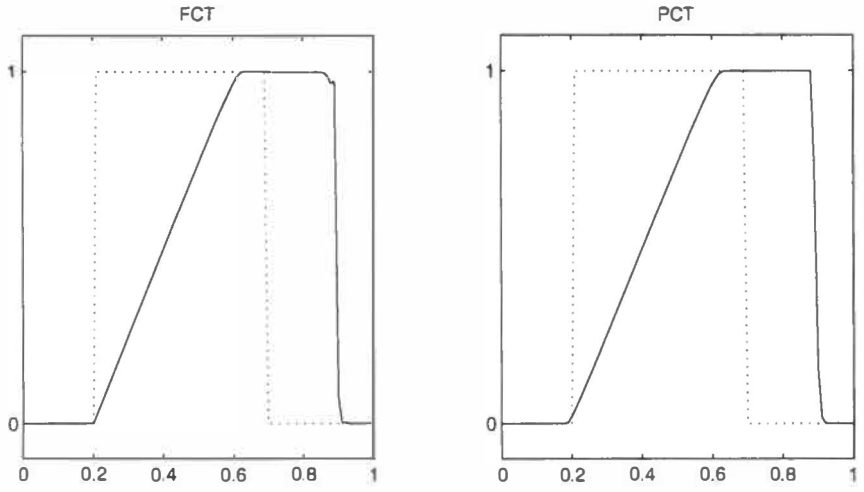

FIGURE 3.10 Burgers equation. Initial data and solution at $t = 0.4$.

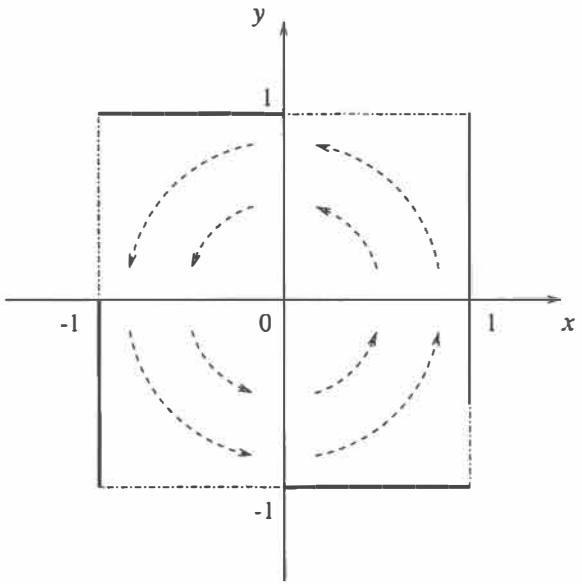

FIGURE 3.11 Rotation of a cylinder. Computational domain.

Rotation of a cylinder

Consider a rotating two-dimensional velocity field

$$v_x = -y, \qquad v_y = x$$

in a square domain $(-1,1)\times(-1,1)$ of the plane (x,y). The counterclockwise rotation takes place about the origin. The location of inflow boundaries (bold lines) is shown in Figure 3.11. The initial configuration of u is a cylinder with a slot depicted in Figure 3.12 and given by

$$u^0(x,y) = \begin{cases} 1, & R < 1/3 \text{ and } (|x| > 0.05 \text{ or } y > 0.5), \\ 0, & \text{otherwise,} \end{cases}$$

where

$$R = \sqrt{x^2 + (y - 1/3)^2}.$$

We use a mesh of 100×100 bilinear elements and the time step $\Delta t = 5\times10^{-3}$. Computational results after one full revolution are presented in Figure 3.13. The FCT solution exhibits some imperfections, whereas the PCT method performs remarkably well.

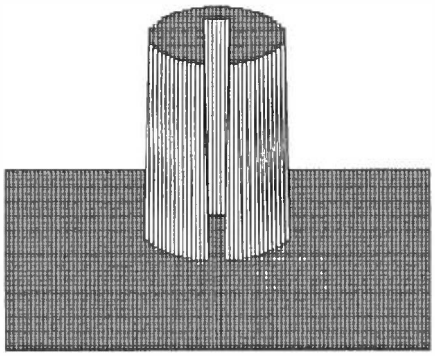

FIGURE 3.12 Rotation of a cylinder. Initial data.

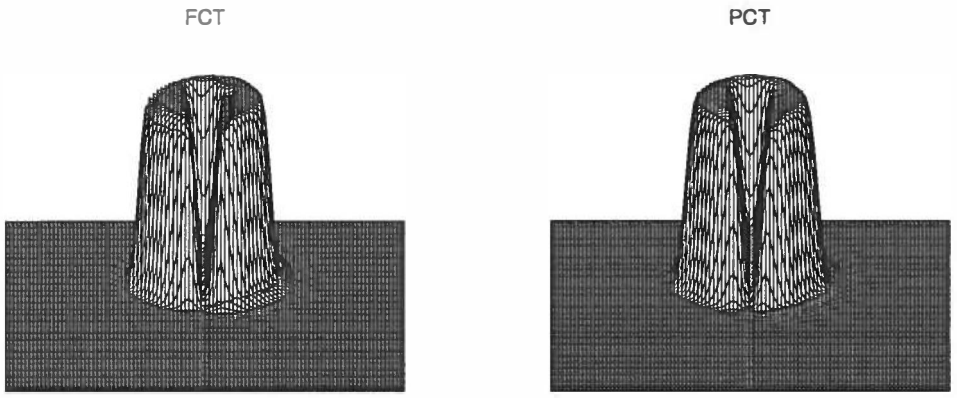

FIGURE 3.13 Rotation of a cylinder. Solution after one full revolution.

3.4 Fractional-step projection method

3.4.1 Overview

The time-dependent Navier-Stokes equations formulated in terms of primitive variables (velocity and pressure) define an unwieldy nonlinear saddle point problem with pressure playing the role of a Lagrange multiplier for the continuity constraint. Mathematical analysis for the Stokes problem reveals that the approximation spaces for velocity and pressure must satisfy an *inf-sup* compatibility condition also referred to as the LBB condition (named after Ladyzhenskaya, Babuška and Brezzi). If the finite dimensional spaces

fail to comply with this condition, the numerical solution can be corrupted by spurious pressure modes. A stabilized version of an *a priori* unstable algorithm can be derived by appropriately modifying the discrete equations (see [64] for a survey of such techniques).

Since there exists no explicit evolutionary equation for the pressure, the continuity and momentum equations must be solved simultaneously to obtain both velocity and pressure. However, the coupled solution procedure based on a stable spatial discretization engenders very large algebraic systems with unfavorable properties. The computational burden can be drastically reduced by employing a fractional-step approach to time integration of the Navier-Stokes equations. To this end, the so-called projection methods were introduced in the late 1960s by Chorin [6], [7] and Temam [81], [82] to decouple velocity and pressure. These schemes (also known as fractional-step, splitting or pressure correction methods) possess an intrinsic stabilization mechanism which makes it possible to circumvent the restrictive LBB condition and use equal-order interpolation under certain circumstances. Hence, a cost-effective solution of large-scale transient problems is feasible.

The classical finite-difference projection schemes were carried over to finite elements by Donea *et al.* [13] and successfully applied by many others. Van Kan [42] is credited with a popular pressure correction scheme which is second-order accurate in time. Fractional-step projection methods are based on a solid theoretical background, which can be found e.g. in the book by Quartapelle [62]. An often cited heuristic study of semi-implicit finite element projection schemes was performed by Gresho [23], [24] (see also [26]). For a rigorous finite element error analysis of projection methods for the incompressible Navier-Stokes equations, the reader is referred to a recent monograph by Prohl [61] and references therein. Computational aspects were addressed by Turek [88] who introduced a class of discrete projection methods which unite the coupled approach and splitting/projection schemes in the framework of special iterative techniques for the Schur complement equation for the pressure [86], [87].

A fractional-step projection scheme of extremely simple algorithmic structure was proposed by Laval and Quartapelle [51]. In this section, we present a modification of their method which involves an implicit treatment of viscous terms and promotes projection at the continuous rather than discrete level. Penalty functions are employed to reinforce the Neumann boundary condition for the pressure Poisson equation. A straightforward extension to the case of an inhomogeneous continuity constraint is carried out. Numerical results for the lid-driven cavity and the standing vortex problem illustrate the performance of the algorithm.

3.4.2 Initial-boundary value problem

Let Ω be a bounded domain of $\mathbf{R}^2$ with a piecewise-smooth boundary Γ. The unsteady pseudo-compressible Navier-Stokes equations read

$$\frac{\partial \mathbf{u}}{\partial t} + (\mathbf{u} \cdot \nabla)\mathbf{u} = -\nabla p + \nabla \cdot (\nu[\nabla \mathbf{u} + (\nabla \mathbf{u})^T]), \tag{3.62}$$

$$\nabla \cdot \mathbf{u} = \delta \quad \text{in } \Omega, \tag{3.63}$$

where $\mathbf{u} = \mathbf{u}(\mathbf{x}, t)$ is the velocity, p is the modified pressure, ν is the kinematic viscosity, and δ takes account of pseudo-compressibility (if any).

Denote two segments of the boundary Γ by Γ_n and Γ_τ. These segments may be empty, overlapping or even equal. Equations (3.62)–(3.63) are supplemented by the boundary conditions

$$\mathbf{n} \cdot \mathbf{u} = u_n \quad \text{on } \Gamma_n, \tag{3.64}$$

$$\tau \cdot \mathbf{u} = u_\tau \quad \text{on } \Gamma_\tau, \tag{3.65}$$

$$-p + \nu\, \mathbf{n} \cdot [\nabla \mathbf{u} + (\nabla \mathbf{u})^T] \cdot \mathbf{n} = s_n = s_n^{(p)} + s_n^{(u)} \quad \text{on } \Gamma \backslash \Gamma_n, \tag{3.66}$$

$$\nu\, \tau \cdot [\nabla \mathbf{u} + (\nabla \mathbf{u})^T] \cdot \mathbf{n} = s_\tau \quad \text{on } \Gamma \backslash \Gamma_\tau. \tag{3.67}$$

Here $\mathbf{n}$ is the outward unit normal to Γ and τ is the unit tangent vector. Furthermore, $s_n^{(p)}$ and $s_n^{(u)}$ designate the pressure and viscous part, respectively, of the prescribed normal stress. The possible combinations of boundary conditions are as follows:

- velocity specified on $\Gamma_n \cap \Gamma_\tau$,
- stress vector prescribed on $\Gamma \backslash (\Gamma_n \cup \Gamma_\tau)$,
- normal velocity and tangential stress specified on $\Gamma_n \backslash (\Gamma_n \cap \Gamma_\tau)$,
- tangential velocity and normal stress prescribed on $\Gamma_\tau \backslash (\Gamma_n \cap \Gamma_\tau)$.

The initial condition consists in the specification of the velocity field at the time $t = 0$, namely,

$$\mathbf{u}(\mathbf{x}, 0) = \mathbf{u}_0(\mathbf{x}) \quad \text{in } \Omega, \tag{3.68}$$

where it is required that

$$\nabla \cdot \mathbf{u}_0 = \delta \quad \text{in } \Omega. \tag{3.69}$$

No initial condition for the pressure is needed.

The boundary and initial data must satisfy the following compatibility condition

$$\mathbf{n} \cdot \mathbf{u}_0 = u_n \quad \text{on } \Gamma_n. \tag{3.70}$$

Finally, another solvability constraint arises if $\Gamma_n = \Gamma$:

$$\int_\Gamma u_n \, dS = \int_\Omega \delta \, d\mathbf{x}. \tag{3.71}$$

This follows from integrating the continuity equation (3.63) over Ω and using the divergence theorem. In this case, the pressure is determined up to an arbitrary additive constant.

3.4.3 Projection guidelines

Fractional-step projection methods separate the effect of viscous diffusion from that of incompressibility (pseudo-compressibility). This leads to an uncoupled formulation, so that the velocity and pressure are obtained by solving a sequence of smaller subproblems at each time step. The procedure comprises the following algorithmic steps:

1. Guess the pressure gradient and plug it into the momentum equations.
2. Relax the continuity constraint and solve the vector Burgers equation for an intermediate velocity field.
3. Solve the implied pressure Poisson equation or its discrete counterpart.
4. Project the intermediate velocity onto the subspace of functions satisfying the continuity equation.

The last step takes advantage of a theorem of orthogonal decomposition due to Ladyzhenskaya [49]:

Theorem. *Any vector field* $\mathbf{v}$ *defined in* Ω *admits the unique orthogonal decomposition*

$$\mathbf{v} = \mathbf{w} + \nabla\varphi, \tag{3.72}$$

where $\mathbf{w}$ *is a solenoidal vector field with normal component vanishing on the boundary* Γ *of* Ω.

Proof. See e.g. [62].

This fundamental result suggests the notation $\mathbf{w} = \mathcal{P}\mathbf{v}$, $\nabla\varphi = \mathcal{Q}\mathbf{v}$, where $\mathcal{P}$ and $\mathcal{Q} = \mathcal{I} - \mathcal{P}$ are the operators of orthogonal projection onto the subspace

of divergence-free vectors and the subspace of curl-free vectors, respectively. The projection operators possess the following properties

$$\mathcal{P}^2 = \mathcal{P}, \quad \mathcal{Q}^2 = \mathcal{Q}, \quad \mathcal{P}\mathcal{Q} = \mathcal{Q}\mathcal{P} = 0.$$

The quantity φ is the unique (up to an arbitrary additive constant) solution to the elliptic problem [62]

$$\Delta\varphi = \nabla \cdot \mathbf{v}, \qquad \mathbf{n} \cdot \nabla\varphi|_\Gamma = \mathbf{n} \cdot \mathbf{v}, \tag{3.73}$$

whose solvability condition $\int_\Omega \nabla \cdot \mathbf{v}\ d\mathbf{x} = \int_\Gamma \mathbf{n} \cdot \mathbf{v}\ dS$ is satisfied by the divergence theorem.

Now let $\mathbf{v}$ represent the intermediate velocity field. For the sake of simplicity, consider $\Gamma_n = \Gamma$. Our objective is to process $\mathbf{v}$ so as to extract a final velocity $\mathbf{u}$ which must satisfy the continuity constraint and assume a prescribed boundary value for the normal component. Decomposition (3.72) is ostensibly equivalent to

$$\mathbf{v} = \mathbf{w} + \nabla\varphi_\delta + \nabla(\varphi - \varphi_\delta), \tag{3.74}$$

where the scalar function φ_δ is determined uniquely by solving

$$\Delta\varphi_\delta = \delta, \qquad \mathbf{n} \cdot \nabla\varphi_\delta|_\Gamma = u_n. \tag{3.75}$$

The solvability condition of the above Neumann problem is satisfied by virtue of constraint (3.71). It follows that

$$\mathbf{u} = \mathbf{v} - \nabla\Phi, \tag{3.76}$$

where $\mathbf{u} \stackrel{\text{def}}{=} \mathbf{w} + \nabla\varphi_\delta = \mathcal{P}\mathbf{v} + \nabla\varphi_\delta$ and $\Phi \stackrel{\text{def}}{=} \varphi - \varphi_\delta$.

Before embarking on the details of the fractional-step projection method for (3.62)–(3.68), we elucidate some ins and outs of projection schemes as applied to the incompressible Navier-Stokes equations with Dirichlet boundary conditions. Taking $\delta \equiv 0$ and $\Gamma_n = \Gamma_\tau = \Gamma$ reduces the problem to

$$\frac{\partial \mathbf{u}}{\partial t} + (\mathbf{u} \cdot \nabla)\mathbf{u} = -\nabla p + \nu\Delta\mathbf{u}, \tag{3.77}$$

$$\nabla \cdot \mathbf{u} = 0 \quad \text{in } \Omega, \tag{3.78}$$

$$\mathbf{n} \cdot \mathbf{u}|_\Gamma = u_n, \quad \tau \cdot \mathbf{u}|_\Gamma = u_\tau, \quad \mathbf{u}|_{t=0} = \mathbf{u}_0. \tag{3.79}$$

Assuming sufficient regularity, the divergence of (3.77) yields the so-called consistent pressure Poisson equation [26]

$$-\Delta p = \nabla \cdot [(\mathbf{u} \cdot \nabla)\mathbf{u} - \nu\Delta u] \quad \text{in } \Omega. \tag{3.80}$$

The concomitant Neumann boundary condition is derived by applying the normal component of the momentum equation at the boundary

$$\mathbf{n} \cdot \nabla p = \mathbf{n} \cdot \left[\nu \Delta \mathbf{u} - (\mathbf{u} \cdot \nabla)\mathbf{u} - \frac{\partial \mathbf{u}}{\partial t} \right] \quad \text{on } \Gamma. \tag{3.81}$$

Gresho and Sani [25] assert that if all solvability conditions are satisfied, the system given by (3.77)–(3.79) is equivalent to that with (3.78) replaced by (3.80)–(3.81).

The celebrated Chorin projection scheme for (3.77)–(3.79) reads [6], [61]

1. Start with initial data $\mathbf{u}^0 = \mathbf{u}_0$.

2. For $n \geq 0$, find $\tilde{\mathbf{u}}^{n+1}$ as the solution of

$$\frac{\tilde{\mathbf{u}}^{n+1} - \mathbf{u}^n}{\Delta t} + (\mathbf{u}^n \cdot \nabla)\tilde{\mathbf{u}}^{n+1} = \nu \Delta \tilde{\mathbf{u}}^{n+1}, \tag{3.82}$$

$$\mathbf{n} \cdot \tilde{\mathbf{u}}^{n+1}|_\Gamma = u_n, \quad \tau \cdot \tilde{\mathbf{u}}^{n+1}|_\Gamma = u_\tau. \tag{3.83}$$

3. Given $\tilde{\mathbf{u}}^{n+1}$, compute the couple $\{\mathbf{u}^{n+1}, p^{n+1}\}$ from

$$\frac{\mathbf{u}^{n+1} - \tilde{\mathbf{u}}^{n+1}}{\Delta t} = -\nabla p^{n+1}, \tag{3.84}$$

$$\nabla \cdot \mathbf{u}^{n+1} = 0, \quad \mathbf{n} \cdot \mathbf{u}^{n+1}|_\Gamma = u_n. \tag{3.85}$$

Remark 3.3. The pressure term is omitted in the semi-discretized momentum equation (3.82), i.e. the intermediate velocity $\tilde{\mathbf{u}}^{n+1}$ is computed using the simplest possible guess for the pressure, and namely $p \equiv 0$.

Remark 3.4. Equations (3.84)-(3.85) define an inviscid flow problem. Therefore, the Dirichlet boundary condition is imposed only for the normal component of the final velocity $\mathbf{u}^{n+1}$. Tangential slip is permitted, but it can be expected to remain small, since owing to (3.83) both components of the intermediate velocity $\tilde{\mathbf{u}}^{n+1}$ match the prescribed boundary data.

For computational purposes, a Poisson equation for p^{n+1} can be derived by applying the divergence operator to (3.84) and using the incompressibility constraint. The attendant boundary condition is obtained by taking the normal component of the inviscid momentum equation on the boundary and recalling that $\mathbf{u}^{n+1}|_\Gamma = \tilde{\mathbf{u}}^{n+1}|_\Gamma = u_n$. This yields

$$-\Delta p^{n+1} = -\frac{1}{\Delta t} \nabla \cdot \tilde{\mathbf{u}}^{n+1}, \qquad \mathbf{n} \cdot \nabla p^{n+1}|_\Gamma = 0. \tag{3.86}$$

The homogeneous Neumann boundary condition is non-physical, since the exact pressure satisfies the problem (3.80)-(3.81). This discrepancy gives rise to a spurious pressure boundary layer of width $\mathcal{O}(\sqrt{\nu\Delta t})$. However, the product of kinematic viscosity and the time step is small for most of the practical applications. Thus, p^{n+1} is indeed a reasonable approximation to the exact pressure $p(t_{n+1})$.

The coveted solenoidal velocity field is given by the explicit relation

$$\mathbf{u}^{n+1} = \tilde{\mathbf{u}}^{n+1} - \Delta t \, \nabla p^{n+1}. \tag{3.87}$$

In order to analyze the stability properties of Chorin's projection method based on a pressure Poisson equation, it is convenient to recast it in terms of intermediate velocities as a semi-explicit pressure stabilization scheme [66]

$$\frac{\tilde{\mathbf{u}}^{n+1} - \tilde{\mathbf{u}}^{n}}{\Delta t} + (\mathbf{u}^{n} \cdot \nabla)\tilde{\mathbf{u}}^{n+1} = -\nabla p^{n} + \nu \Delta \tilde{\mathbf{u}}^{n+1}, \tag{3.88}$$

$$\mathbf{n} \cdot \tilde{\mathbf{u}}^{n+1}|_{\Gamma} = u_n, \quad \tau \cdot \tilde{\mathbf{u}}^{n+1}|_{\Gamma} = u_\tau, \tag{3.89}$$

$$\nabla \cdot \tilde{\mathbf{u}}^{n+1} = \Delta t \, \Delta p^{n+1}, \quad \mathbf{n} \cdot \nabla p^{n+1}|_{\Gamma} = 0. \tag{3.90}$$

This resembles the stabilized finite element method of Brezzi and Pitkäranta [5]. If the above equations are discretized using an equal-order interpolation for velocity and pressure, e.g. Q_1/Q_1 elements, the stability of the scheme is secured provided the time step is not too small [29], [61]:

$$\Delta t \geq C h^{m+1}, \tag{3.91}$$

where h is the spatial mesh size, m is the interpolation degree, and C is a constant. Of course, Δt is not subject to any stability restrictions whenever the finite element pair satisfies the LBB condition.

Projection step can also be realized by first discretizing the coupled system (3.84)–(3.85) in space and then applying the discrete differential operators to obtain [62]

$$C^T M^{-1} C P^{n+1} = \frac{1}{\Delta t} C^T \tilde{U}^{n+1} \tag{3.92}$$

followed by

$$U^{n+1} = \tilde{U}^{n+1} - \Delta t \, M^{-1} C P^{n+1}. \tag{3.93}$$

Here C is the gradient matrix, $-C^T$ is the divergence matrix, and M is the consistent mass matrix. It should be emphasized that equation (3.92) is not the discretized pressure Poisson equation (3.86).

The pros and cons of discrete projection methods are as follows. On the one hand, no artificial boundary condition for the pressure is required, and equation (3.92) admits discontinuous pressure approximations, i.e. it has access to a larger class of solutions than the pressure Poisson equation. On the other hand, the discrete 'Laplacian' matrix $C^T M^{-1} C$ is global and cannot be assembled element-by-element. Moreover, the involved inverse of the consistent mass matrix is dense. Mass lumping is a possible remedy for that problem, but matrix assembly remains cumbersome anyway. Mixed interpolation is mandatory for discrete projection methods. The "slightly unstable but highly usable" [26] Q_1/Q_0 element (bilinear velocity, piecewise constant pressure) was found to work well in practice [13], [24], [51]. Also the nonconforming $\tilde{Q}_1/Q_0$ element (rotated bilinear velocity, piecewise constant pressure) of Rannacher and Turek [67] is to be recommended.

Equal-order interpolation is a tangible asset when it comes to obtaining a continuous pressure field at a low cost. In addition, there exist many robust and efficient finite element techniques and software for numerical solution of the Poisson equation. Therefore, in the sequel we will stick to the continuous projection methodology.

3.4.4 Fractional-step algorithm

Following Laval and Quartapelle [51], we employ an operator-splitting approach to isolate the effects of convection, viscous diffusion and pseudo-compressibility from one another and treat them separately with properly designed numerical schemes. This contributes to the efficiency of computations and facilitates implementation of advanced solution techniques for individual algorithmic steps as they become available. The time-stepping is tailored to maximize accuracy and/or stability. In particular, the stability of equal-order interpolations can be further enhanced by enforcing condition (3.91) for the projection step while leaving the time step unconstrained for convection-diffusion [29]. A fractional-step algorithm consisting of three distinct computational stages is outlined below.

Convection step

The nonlinear convective part of the problem is obtained by relieving the momentum equation (3.62) of the stress terms. This yields the following equation for evolution of a self-advecting velocity field

$$\frac{\partial \mathbf{u}}{\partial t} + (\mathbf{u} \cdot \nabla)\mathbf{u} = 0. \tag{3.94}$$

Because of the hyperbolic nature of this equation, boundary values can be prescribed only on the inflow boundary $\Gamma_{\text{in}} = \{\mathbf{x} \in \Gamma_n : \ u_n < 0\}$. Thus, an appropriate boundary condition for the convection step is

$$\mathbf{n} \cdot \mathbf{u}|_{\Gamma_{\text{in}}} = u_n, \qquad \tau \cdot \mathbf{u}|_{\Gamma_{\text{in}}} = u_\tau. \tag{3.95}$$

Note that in general Γ_{in} is not a subset of Γ_τ. In order to earn a Dirichlet boundary condition for the tangential component of velocity, we can either assign the solution from the previous time step on $\Gamma_{\text{in}} \backslash \Gamma_\tau$ or require that $\Gamma_{\text{in}} \subset \Gamma_\tau$.

The nonlinearity of the convective term calls for the use of an explicit procedure for time discretization of equation (3.94). An appropriate time-stepping is furnished by a second-order accurate Taylor-Galerkin method referred to as the LWFE scheme in the previous section. A Taylor series expansion in the time step Δt provides

$$\mathbf{u}^{n+1} = \mathbf{u}^n + \Delta t \ \mathbf{u}_t^n + \frac{1}{2}(\Delta t)^2 \mathbf{u}_{tt}^n + \mathcal{O}[(\Delta t)^3]. \tag{3.96}$$

The governing equation (3.94) and its derivative with respect to the time imply that

$$\begin{aligned} \mathbf{u}_t &= -(\mathbf{u} \cdot \nabla)\mathbf{u}, \\ \mathbf{u}_{tt} &= -(\mathbf{u}_t \cdot \nabla)\mathbf{u} - (\mathbf{u} \cdot \nabla)\mathbf{u}_t \\ &= \{[(\mathbf{u} \cdot \nabla)\mathbf{u}] \cdot \nabla\}\mathbf{u} + (\mathbf{u} \cdot \nabla)[(\mathbf{u} \cdot \nabla)\mathbf{u}]. \end{aligned}$$

Substitution of the above expressions into the Taylor series (3.96) leads to the following time-discretized equation

$$\begin{aligned} \frac{\mathbf{u}^* - \mathbf{u}^n}{\Delta t} &= -(\mathbf{u}^n \cdot \nabla)\mathbf{u}^n + \frac{1}{2}\Delta t \ \{[(\mathbf{u}^n \cdot \nabla)\mathbf{u}^n] \cdot \nabla\}\mathbf{u}^n \\ &+ \frac{1}{2}\Delta t (\mathbf{u}^n \cdot \nabla)[(\mathbf{u}^n \cdot \nabla)\mathbf{u}^n], \end{aligned} \tag{3.97}$$

where $\mathbf{u}^*$ stands for the intermediate velocity after the convection step.

Let $\mathbf{H}^1(\Omega)$ denote the Sobolev space of vector-valued functions defined on Ω which are square integrable and have square integrable first derivatives with respect to the spatial coordinates. A weak form of equation (3.97) is obtained by taking the scalar product with weighting functions $\mathbf{w} \in \mathbf{H}^1(\Omega)$ such that $\mathbf{w}|_{\Gamma_{\text{in}}} = 0$ and integrating over the domain Ω. In order to employ finite elements with only C^0 continuity, the terms involving second-order spatial derivatives are integrated by parts using straightforward albeit tedious vectorial transformations [15], [62]. The resulting variational formulation reads:

Find $\mathbf{u}^* \in \mathbf{H}^1(\Omega)$ such that

$$\begin{aligned}\langle \mathbf{w}, \mathbf{u}^* - \mathbf{u}^n \rangle / \Delta t = &-\langle \mathbf{w}, (\mathbf{u}^n \cdot \nabla)\mathbf{u}^n \rangle \\ &-\frac{1}{2}\Delta t \left[\langle (\mathbf{u}^n \cdot \nabla)\mathbf{w}, (\mathbf{u}^n \cdot \nabla)\mathbf{u}^n \rangle - \langle (\mathbf{n} \cdot \mathbf{u}^n)\mathbf{w}, (\mathbf{u}^n \cdot \nabla)\mathbf{u}^n \rangle_{\Gamma_{\text{out}}} \right] \\ &+\frac{1}{2}\Delta t \langle \mathbf{w} \times \nabla \times \mathbf{u}^n + (\mathbf{w} \cdot \nabla)\mathbf{u}^n - \mathbf{w}(\nabla \cdot \mathbf{u}^n), (\mathbf{u}^n \cdot \nabla)\mathbf{u}^n \rangle, \\ &\qquad \forall \mathbf{w} \in \mathbf{H}^1(\Omega), \quad \mathbf{w}|_{\Gamma_{\text{in}}} = 0. \end{aligned} \tag{3.98}$$

Here $\langle \cdot, \cdot \rangle$ denotes the integration over Ω, and $\langle \cdot, \cdot \rangle_{\Gamma_{\text{out}}}$ over the outflow boundary $\Gamma_{\text{out}} = \Gamma \backslash \Gamma_{\text{in}}$. Efficiency considerations make it worthwhile to rearrange the last scalar product and solve an equivalent problem [51]:

Find $\mathbf{u}^* \in \mathbf{H}^1(\Omega)$ such that

$$\begin{aligned}\langle \mathbf{w}, \mathbf{u}^* - \mathbf{u}^n \rangle / \Delta t = &-\langle \mathbf{w}, (\mathbf{u}^n \cdot \nabla)\mathbf{u}^n \rangle \\ &-\frac{1}{2}\Delta t \left[\langle (\mathbf{u}^n \cdot \nabla)\mathbf{w}, (\mathbf{u}^n \cdot \nabla)\mathbf{u}^n \rangle - \langle (\mathbf{n} \cdot \mathbf{u}^n)\mathbf{w}, (\mathbf{u}^n \cdot \nabla)\mathbf{u}^n \rangle_{\Gamma_{\text{out}}} \right] \\ &+\frac{1}{2}\Delta t \left[\langle \mathbf{w}, \{ [(\mathbf{u}^n \cdot \nabla)\mathbf{u}^n] \cdot \nabla \} \mathbf{u}^n \rangle - \langle \mathbf{w}(\nabla \cdot \mathbf{u}^n), (\mathbf{u}^n \cdot \nabla)\mathbf{u}^n \rangle \right], \\ &\qquad \forall \mathbf{w} \in \mathbf{H}^1(\Omega), \quad \mathbf{w}|_{\Gamma_{\text{in}}} = 0. \end{aligned} \tag{3.99}$$

An analysis and physical interpretation of the second-order terms arising in weak formulations (3.98) and (3.99) can be found in [15], [51], [62].

Viscous diffusion step

At this stage, the viscous stress term is retained in the Navier-Stokes equations, whereas the nonlinear convection term and the pressure gradient are omitted:

$$\frac{\partial \mathbf{u}}{\partial t} = \nabla \cdot (\nu [\nabla \mathbf{u} + (\nabla \mathbf{u})^T]). \tag{3.100}$$

The boundary conditions to be imposed are those for the complete problem, and namely (3.64)–(3.67).

This equation craves for an implicit treatment, since otherwise the time steps have to be chosen impractically small to guarantee stability [86], [87]. We discretize in time by the one-step θ-scheme

$$\begin{aligned}\frac{\mathbf{u}^{**} - \mathbf{u}^*}{\Delta t} &= \theta \, \nabla \cdot (\nu [\nabla \mathbf{u}^{**} + (\nabla \mathbf{u}^{**})^T]) \\ &+ (1 - \theta) \nabla \cdot (\nu [\nabla \mathbf{u}^* + (\nabla \mathbf{u}^*)^T]), \end{aligned} \tag{3.101}$$

where $\mathbf{u}^{**}$ is the intermediate velocity after the diffusion step. The parameter $\theta \in (0,1]$ characterizes the implicit time-stepping scheme. The choice $\theta = 1$ corresponds to the first-order backward Euler method, and $\theta = \frac{1}{2}$ to the second-order Crank-Nicolson scheme. Multiplying the semi-discretized equation by suitable weighting functions and integrating over Ω, we obtain the associated weak formulation:

Find $\mathbf{u}^{**} \in \mathbf{H}^1(\Omega)$ such that

$$\begin{aligned}\langle \mathbf{w}, \mathbf{u}^{**} - \mathbf{u}^{*} \rangle / \Delta t = &-\frac{\theta}{2} \langle [\nabla \mathbf{w} + (\nabla \mathbf{w})^T], \nu [\nabla \mathbf{u}^{**} + (\nabla \mathbf{u}^{**})^T] \rangle \\ &-\frac{1-\theta}{2} \langle [\nabla \mathbf{w} + (\nabla \mathbf{w})^T], \nu [\nabla \mathbf{u}^{*} + (\nabla \mathbf{u}^{*})^T] \rangle \\ &+ \langle \mathbf{n} \cdot \mathbf{w}, s_n^{(u)} \rangle_{\Gamma \setminus \Gamma_n} + \langle \tau \cdot \mathbf{w}, s_\tau \rangle_{\Gamma \setminus \Gamma_\tau}, \\ &\forall \mathbf{w} \in \mathbf{H}^1(\Omega), \quad \mathbf{n} \cdot \mathbf{w}|_{\Gamma_n} = 0, \quad \tau \cdot \mathbf{w}|_{\Gamma_\tau} = 0. \end{aligned} \tag{3.102}$$

The surface integrals originating from integration by parts accommodate the natural boundary conditions (3.66) and (3.67).

Projection step

The intermediate velocity field $\mathbf{u}^{**}$ contains the effects of convection and viscous diffusion, but it does not generally satisfy the pseudo-compressibility constraint. The objective of the last stage is twofold: to compute the unknown pressure p^{n+1} and to enforce (3.63) for the end-of-step velocity $\mathbf{u}^{n+1}$. The coupled system of equations reads

$$\frac{\partial \mathbf{u}}{\partial t} = -\nabla p, \qquad \nabla \cdot \mathbf{u} = \delta, \tag{3.103}$$

$$\mathbf{n} \cdot \mathbf{u}|_{\Gamma_n} = u_n, \quad p|_{\Gamma \setminus \Gamma_n} = s_n^{(p)}. \tag{3.104}$$

We have already seen that after time discretization this kind of problem can be reformulated as a Poisson equation for the pressure

$$-\Delta p^{n+1} = \frac{1}{\Delta t}[\delta - \nabla \cdot \mathbf{u}^{**}], \tag{3.105}$$

$$\mathbf{n} \cdot \nabla p^{n+1}|_{\Gamma_n} = 0, \quad p^{n+1}|_{\Gamma \setminus \Gamma_n} = s_n^{(p)} \tag{3.106}$$

followed by the velocity update

$$\mathbf{u}^{n+1} = \mathbf{u}^{**} - \Delta t \, \nabla p^{n+1}. \tag{3.107}$$

In the finite element framework, natural boundary conditions are satisfied in a weak sense only. This may turn out to be insufficient to guarantee that $\mathbf{n} \cdot \nabla p^{n+1}|_{\Gamma_n} = 0$ and, consequently, $\mathbf{n} \cdot \mathbf{u}^{n+1}|_{\Gamma_n} = u_n$. In particular, a non-physical penetration of solid walls can occur. Therefore, we alter the discrete form of the pressure Poisson equation by adding a penalty term on the portion of the boundary where the homogeneous Neumann boundary condition must apply. A similar approach was used by Hansbo [31] to reinforce stress boundary conditions.

The modified variational formulation results from minimization of the penalized energy functional

$$J_\alpha(p) = \frac{1}{2}\langle \nabla p, \nabla p \rangle - \langle p, \delta - \nabla \cdot \mathbf{u}^{**} \rangle / \Delta t + \frac{\alpha}{2} \langle \mathbf{n} \cdot \nabla p, \mathbf{n} \cdot \nabla p \rangle_{\Gamma_n},$$

where α is a large positive penalty number [90],[96]. Here p represents a C^0 finite element approximation of pressure. Setting the first variation of J_α equal to zero, we obtain the following problem:

Find p^{n+1} such that

$$\langle \nabla q, \nabla p^{n+1} \rangle + \alpha \langle \mathbf{n} \cdot \nabla q, \mathbf{n} \cdot \nabla p^{n+1} \rangle_{\Gamma_n} = \langle q, \delta - \nabla \cdot \mathbf{u}^{**} \rangle / \Delta t,$$
$$q|_{\Gamma \setminus \Gamma_n} = 0. \qquad (3.108)$$

The weak form of equation (3.107) for the final velocity field is obtained in the standard way:

Find $\mathbf{u}^{n+1} \in \mathbf{H}^1(\Omega)$ such that

$$\langle \mathbf{w}, \mathbf{u}^{n+1} - \mathbf{u}^{**} \rangle / \Delta t = -\langle \mathbf{w}, \nabla p^{n+1} \rangle, \qquad \forall \mathbf{w} \in \mathbf{H}^1(\Omega). \qquad (3.109)$$

Mass lumping by the row-sum technique is employed to avoid solving a consistent mass matrix problem.

3.4.5 Numerical examples

Lid-driven cavity

The laminar incompressible flow in a square cavity with a moving wall is a standard model problem for evaluating numerical techniques for the Navier-Stokes equations. The computational domain is a unit square $(0,1) \times (0,1)$ in the plane (x, y). Initially the fluid is at rest, and at $t = 0$ the upper wall is impulsively set into motion with unit velocity. In this setting, the Reynolds number Re is inversely proportional to the kinematic viscosity ν. We use

a uniform mesh of 50×50 Q_1/Q_1 elements and the time step $\Delta t = 0.01$. The Neumann problem for the pressure is singular. For a unique solution to exist, the pressure value at the bottom right corner of the cavity is set equal to zero.

Evolution of the streamlines and pressure field for $Re = 1000$ is shown in Figures 3.14–3.17. A steady-state regime is reached by the time $t = 50$. The center of the primary vortex is slightly displaced towards the top right corner. As the Reynolds number increases, the vortex center approaches the geometric center of the domain, see Figures 3.18-3.19. For $Re \geq 5000$ its location becomes virtually invariant. Secondary vortices develop in the corners of the cavity. It will be noted that some interesting flow details are not resolved because of the relatively coarse mesh employed. The presented results agree well with those reported by Ghia *et al.* [22] whose work may be consulted for a comprehensive study of the incompressible flow in a lid-driven cavity at high Reynolds numbers.

Standing vortex

This benchmark problem is commonly used to assess how much dissipation a numerical scheme introduces. The flow is inviscid, and the domain of interest is a unit square. As before, zero pressure is maintained at the bottom right corner of the box. The initial velocity profile is axisymmetric with zero radial velocity:

$$u_r = 0.$$

The circumferential velocity is given by

$$u_\theta = \begin{cases} 5r, & r < 0.2, \\ 2 - 5r & 0.2 \leq r \leq 0.4, \\ 0, & r > 0.4, \end{cases}$$

where

$$r = \sqrt{(x - 0.5)^2 + (y - 0.5)^2}.$$

This initial condition shown in Figure 3.20 is also the exact steady-state solution. Thus, the numerical formulation should preserve the original vortex as accurately as possible.

The velocity field and pressure contours at $t = 3$ obtained with a uniform mesh of 30×30 Q_1/Q_1 elements and the time step $\Delta t = 0.01$ are displayed in Figure 3.21. We see that the fractional-step projection method is stable and only slightly dissipative, so that the numerical solution looks very reasonable.

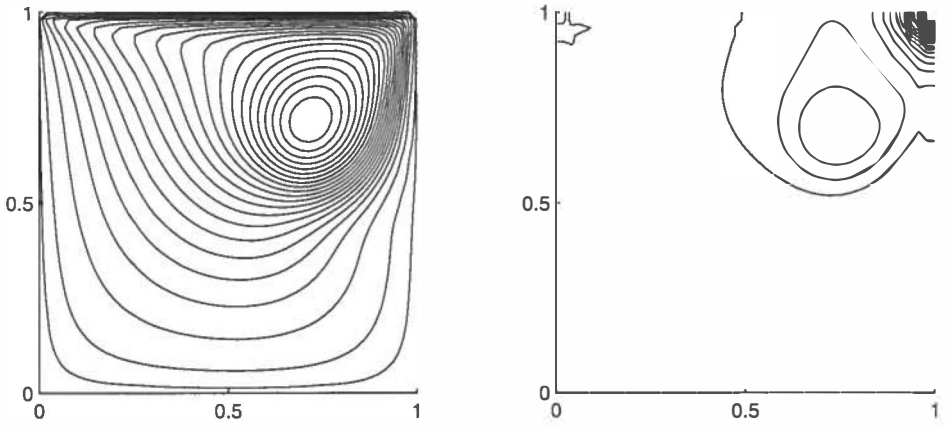

FIGURE 3.14 Driven cavity, $Re = 1000$. Streamlines and pressure field at $t = 5$.

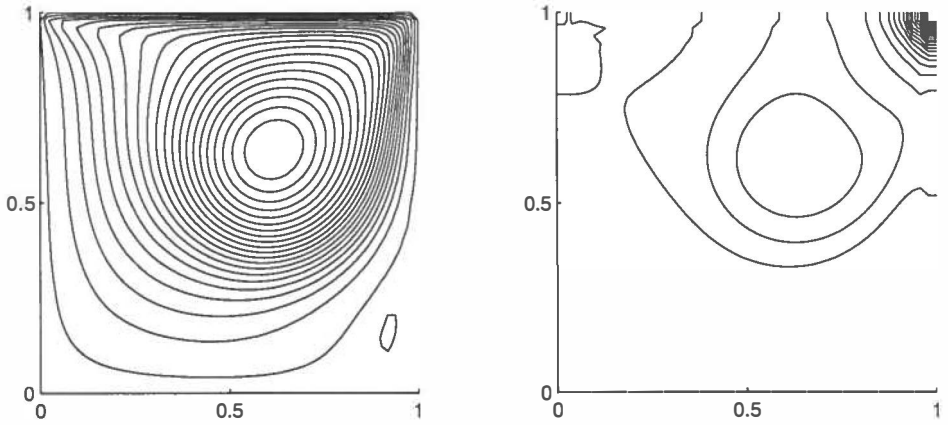

FIGURE 3.15 Driven cavity, $Re = 1000$. Streamlines and pressure field at $t = 10$.

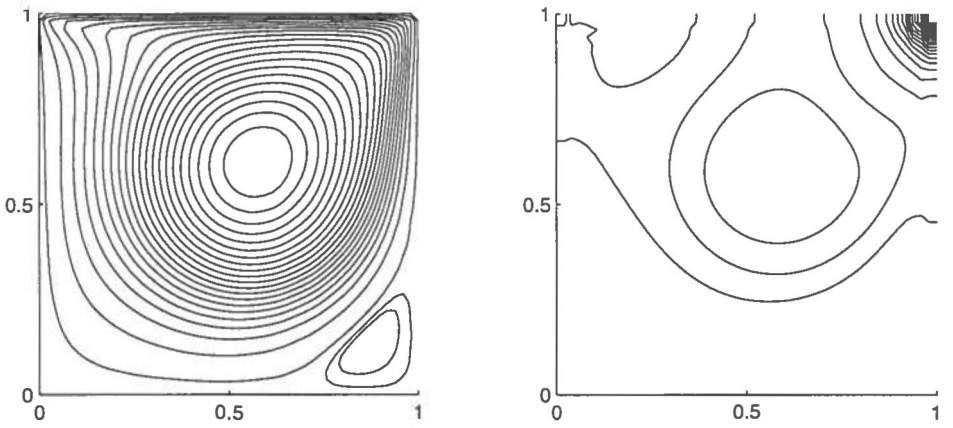

FIGURE 3.16 Driven cavity, $Re = 1000$. Streamlines and pressure field at $t = 15$.

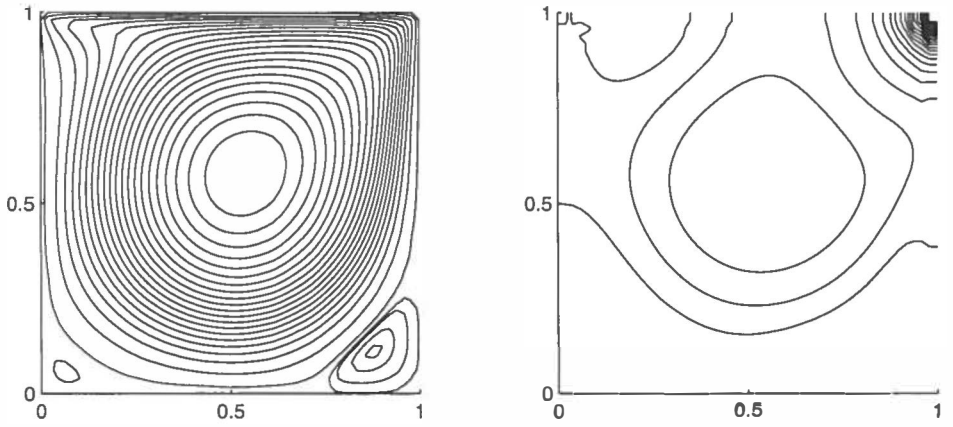

FIGURE 3.17 Driven cavity, $Re = 1000$. Streamlines and pressure field at $t = 50$.

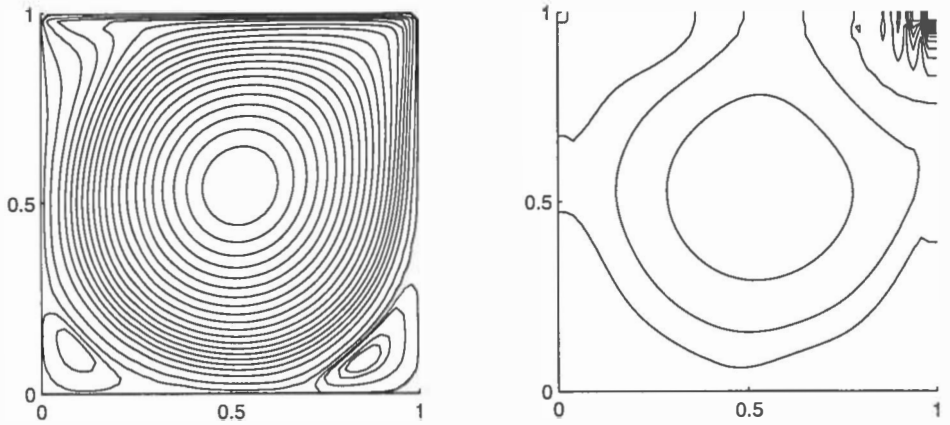

FIGURE 3.18 Driven cavity, $Re = 5000$. Streamlines and pressure field at $t = 50$.

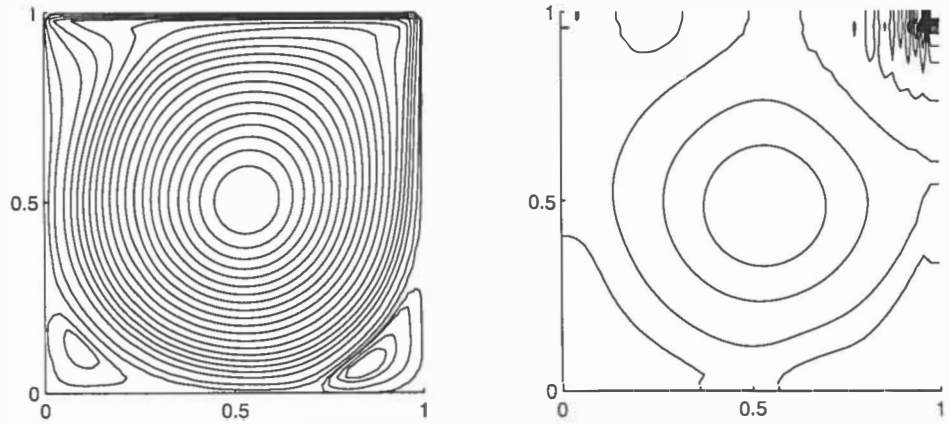

FIGURE 3.19 Driven cavity, $Re = 10000$. Streamlines and pressure field at $t = 50$.

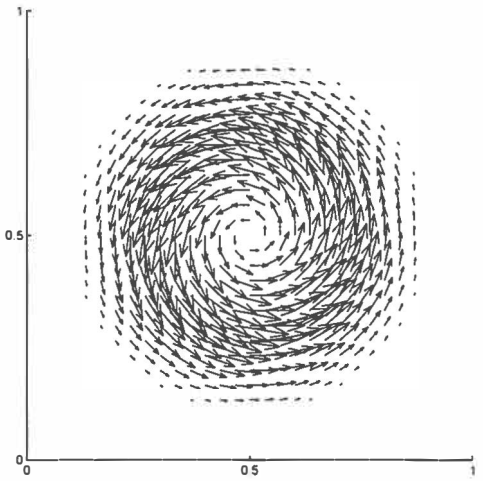

FIGURE 3.20 Standing vortex. Velocity field at $t = 0$.

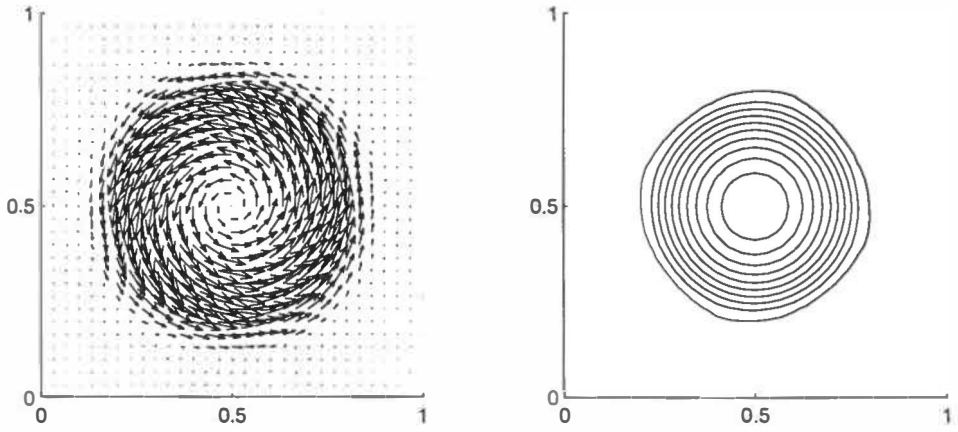

FIGURE 3.21 Standing vortex. Streamlines and pressure field at $t = 3$.

Chapter 4

NUMERICAL ALGORITHM

4.1 Operator-splitting

The numerical algorithm presented in this chapter makes an extensive use of operator-splitting techniques to divide-and-conquer various physical effects. In the preceding chapter, we have already seen an example of a fractional-step method which employed a straightforward splitting procedure to handle nonlinear convection, viscous diffusion and pseudo-compressibility one at a time. This approach to time discretization of complicated initial-boundary value problems proves very useful in a variety of other settings as well. In fact, operator-splitting is even indispensable in some cases. For instance, the consistent Taylor-Galerkin method for the convection-diffusion equation leads to an incremental form of the Crank-Nicolson time-stepping scheme and degenerates into the unstable Galerkin formulation if applied in transient situations which eventually reach a highly convective steady state. This pitfall can be circumvented if convection and diffusion are treated separately by optimal Taylor-Galerkin methods [14].

The splitting of differential operators can be performed either at the algebraic or at the differential level [64]. In this thesis, we adhere to the latter strategy, whereby the original problem is reformulated as a sequence of subproblems endowed with consistent boundary conditions. Consider a generic time-dependent partial differential equation

$$\begin{aligned} &\frac{\partial u}{\partial t} + \mathcal{A}u = 0 \quad \text{in } \Omega \times (0,T), \\ &u|_{t=0} = u_0 \quad \text{in } \Omega. \end{aligned} \tag{4.1}$$

Furthermore, assume that the spatial differential operator $\mathcal{A}$ admits decomposition into a sum of components of simpler structure:

$$\mathcal{A} = \sum_{\alpha=1}^{m} \mathcal{A}_\alpha. \tag{4.2}$$

According to Marchuk [55], a general approach to component-by-component operator-splitting consists in the following approximation of problem (4.1) on each time interval $[t_n, t_{n+1}]$

$$\frac{\partial u_\alpha}{\partial t} + \mathcal{A}_\alpha u_\alpha = 0 \quad \text{in } \Omega \times (t_n, t_{n+1}), \qquad \alpha = 1, 2, \ldots, m \tag{4.3}$$

in which

$$u_\alpha^n = u_{\alpha-1}^{n+1}, \qquad u_0^{n+1} = u^n, \qquad u_m^{n+1} = u^{n+1}.$$

Both the complete problem (4.1) and each auxiliary problem (4.3) must be supplemented by suitable boundary conditions.

Operator-splitting methods are particularly attractive for solution of coupled systems of nonlinear convection-diffusion-reaction equations, because transport and reactions often occur at quite different rates [94]. The same applies to other relevant physical phenomena such as expansion or shrinkage of bubbles. An attempt to take account of all effects simultaneously would inevitably become a source of inefficiency. Having the finite element methods from Chapter 3 and operator-splitting tools at our disposal, we can proceed to solve the system of equations derived in Chapter 2.

4.2 Gas phase variables

In light of the above, the hyperbolic equations for the gas phase variables are split into four independent pure convection problems

$$\frac{\partial n}{\partial t} + \nabla \cdot (n \mathbf{v}_G) = 0, \qquad n|_{\Gamma_{\text{in}}} = n_{\text{in}}, \tag{4.4}$$

$$\frac{\partial w}{\partial t} + \mathbf{v}_G \cdot \nabla w = 0, \qquad w|_{\Gamma_{\text{in}}} = w_{\text{in}}, \tag{4.5}$$

$$\frac{\partial a}{\partial t} + \mathbf{v}_G \cdot \nabla a = 0, \qquad a|_{\Gamma_{\text{in}}} = a_{\text{in}}, \tag{4.6}$$

$$\frac{\partial \rho}{\partial t} + \nabla \cdot (\rho \mathbf{v}_G) = 0, \qquad \rho|_{\Gamma_{\text{in}}} = \rho_{\text{in}}, \tag{4.7}$$

and a system of nonlinear ordinary differential equations for each node

$$\frac{dw}{dt} = \frac{1}{a\rho_L}\left(p_G - p_H - 4\mu\frac{w}{a} - \frac{2\sigma}{a}\right) - \frac{3}{2}\frac{w^2}{a}, \tag{4.8}$$

$$\frac{da}{dt} = w - \frac{\eta\mathcal{N}}{\rho_L}, \tag{4.9}$$

$$\frac{d\rho}{dt} = -4\pi a^2 n\eta\mathcal{N}. \tag{4.10}$$

For notational simplicity, the subproblem indices are dropped and the effective density of the gas phase is denoted by ρ in the above equations. Recall that p_G is proportional to ρ and inversely proportional to a^3, whereas $\mathcal{N}$ is a function of p_G.

Convection of the quantities at hand is accomplished by the free-Lagrange method capable of dealing with evolution of the domain occupied by the gas phase. The conservative formulation (3.10) lends itself to treatment of equations (4.4) and (4.7), while the non-conservative formulation (3.9) is appropriate for discretization of equations (4.5) and (4.6). Note that, due to the absence of the diffusion term, integration is limited to the surface of the space-time slab and can be performed as for two-dimensional problems.

The coupled equations (4.8)–(4.10) are solved by GRK4T, an embedded Runge-Kutta method of fourth order with automatic step size control for stiff ODE systems [43]. We use an error norm based solely on the bubble size and build in a safeguard preventing the bubble radius or effective gas density from taking on negative values.

4.3 Velocity fields

The liquid phase velocity and the modified pressure are computed by the fractional-step projection method. A fixed mesh of Q_1/Q_1 elements is used for spatial discretization. In accordance with the declared operator-splitting strategy, the simplified system of macroscopic continuity and momentum equations is decomposed into three subproblems:

Convection step

$$\frac{\partial \mathbf{v}_L}{\partial t} + (\mathbf{v}_L \cdot \nabla)\mathbf{v}_L = 0, \tag{4.11}$$

Viscous diffusion step

$$\frac{\partial \mathbf{v}_L}{\partial t} = \nabla \cdot (\nu[\nabla \mathbf{v}_L + (\nabla \mathbf{v}_L)^T]) - \epsilon\mathbf{g}, \qquad \mathbf{v}_L|_\Gamma = 0, \tag{4.12}$$

Projection step

$$\frac{\partial \mathbf{v}_L}{\partial t} = -\nabla p, \qquad \nabla \cdot \mathbf{v}_L = 0, \qquad \mathbf{n} \cdot \mathbf{v}_L|_\Gamma = 0, \tag{4.13}$$

which are successively solved by the finite element techniques expounded in Chapter 3. An explicit treatment is adopted for the buoyancy force.

The gas phase velocity can be determined from the relation

$$\mathbf{v}_G = \mathbf{v}_L + \mathbf{v}_{\text{slip}} + \mathbf{v}_{\text{disp}} \tag{4.14}$$

provided $\mathbf{v}_{\text{slip}}$ and $\mathbf{v}_{\text{disp}}$ are known. The standard slip velocity is recovered using a lumped-mass L_2-projection of the form

$$\langle \mathbf{w}, \mathbf{v}_{\text{slip}} \rangle = -\frac{\rho_L}{C_W} \langle \mathbf{w}, \nabla p + \mathbf{g} \rangle, \qquad \forall \mathbf{w} \in \mathbf{H}^1(\Omega). \tag{4.15}$$

The computation of the dispersive contribution to the gas phase velocity is a little bit more involved. By definition, $\mathbf{v}_{\text{disp}}$ should approximately satisfy

$$\epsilon \mathbf{v}_{\text{disp}} = -D \nabla \epsilon. \tag{4.16}$$

First we illustrate how this can be achieved in one dimension. Consider a uniform mesh of size Δx and a piecewise-linear nonnegative function $\epsilon = \epsilon(x)$ with nodal values ϵ_i. The problem at hand is akin to that of superconvergent gradient recovery by averaging [46], [47]. Since the derivative of ϵ is discontinuous at nodes, the dispersive velocity $v = v(x)$ is evaluated at the element midpoints and averaged to yield the nodal values:

$$v_i = \frac{v_{i-1/2} + v_{i+1/2}}{2}, \tag{4.17}$$

where

$$v_{i-1/2} = \begin{cases} 0, & \epsilon_{i-1} = \epsilon_i, \\ \frac{2D}{\Delta x} \frac{\epsilon_{i-1} - \epsilon_i}{\epsilon_{i-1} + \epsilon_i}, & \text{otherwise}, \end{cases} \tag{4.18}$$

and

$$v_{i+1/2} = \begin{cases} 0, & \epsilon_i = \epsilon_{i+1}, \\ \frac{2D}{\Delta x} \frac{\epsilon_i - \epsilon_{i+1}}{\epsilon_i + \epsilon_{i+1}}, & \text{otherwise}. \end{cases} \tag{4.19}$$

Here we take advantage of the fact that ϵ can vanish in the interior of an element only if so does its derivative. Applying the above formulae in each coordinate direction, we obtain a continuous $\mathbf{v}_{\text{disp}}$.

4.4 Concentrations of species

The problem for effective concentrations of species in the liquid phase can be logically split into a transport step and a reaction step. The magnitude of molecular diffusion coefficients is typically of the order $\mathcal{O}(10^{-9})$, so that diffusion does not have any appreciable influence on the numerical solution. Thus, we can omit the diffusion terms and deal with

$$\frac{\partial \tilde{c}_A}{\partial t} + \mathbf{v}_L \cdot \nabla \tilde{c}_A = 0, \tag{4.20}$$

$$\frac{\partial \tilde{c}_B}{\partial t} + \mathbf{v}_L \cdot \nabla \tilde{c}_B = 0, \tag{4.21}$$

$$\frac{\partial \tilde{c}_P}{\partial t} + \mathbf{v}_L \cdot \nabla \tilde{c}_P = 0 \tag{4.22}$$

followed by

$$\frac{d\tilde{c}_A}{dt} = -\tilde{k}_2 c_A c_B + 4\pi a^2 n \mathcal{N}, \tag{4.23}$$

$$\frac{d\tilde{c}_B}{dt} = -\nu_B \tilde{k}_2 c_A c_B, \tag{4.24}$$

$$\frac{d\tilde{c}_P}{dt} = \nu_P \tilde{k}_2 c_A c_B. \tag{4.25}$$

The incompressibility condition was invoked to obtain the non-divergence formulation for the pure convection step.

Equations (4.20)–(4.22) are solved by the high-resolution PCT scheme. Bilinear interpolation is employed on the same mesh as for velocities and pressure. The explicit Euler method will suffice for discretization of ordinary differential equations (4.23)–(4.25).

4.5 Projection between meshes

The simultaneous existence of two different meshes (an unstructured Lagrangian grid for the gas phase variables and a structured Cartesian grid for the modified pressure, velocities and concentrations) raises the issue of efficient intergrid transfer of data. The gas phase velocity can be simply interpolated from the Eulerian grid. At the same time, it is necessary to ensure the conservation of quantities to be projected from the Lagrangian to the Eulerian mesh (the gas holdup and the interphase mass transfer term). In this section, we devise a simplified mass-conserving projection scheme for a cost-effective transfer of data between grids.

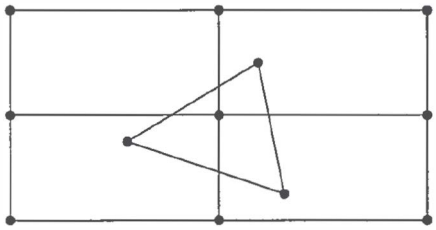

FIGURE 4.1 Intersection of a triangle with Cartesian grid elements.

Let u^L be a piecewise-linear function defined on the Lagrangian mesh. Each triangular element T_i holds the mass

$$m(T_i) = \int_{T_i} u^L \, d\mathbf{x} = \bar{u}_i^L |T_i|, \tag{4.26}$$

where $\bar{u}_i^L$ is the value of u^L at the centroid of T_i, and $|\cdot|$ denotes the area of a polygon. The basic idea is to distribute $m(T_i)$ among the quadrilateral elements of the Eulerian mesh which T_i intersects (see Figure 4.1). Each quadrilateral Q_j receives a mass fraction proportional to the intersection area. This procedure yields an array $\bar{u}^E$ of mean concentrations associated with elements of the background mesh. Finally, the piecewise-constant $\bar{u}^E$ is post-processed to obtain a continuous mass-conserving function u^E defined on the Eulerian mesh.

The proposed simplified projection algorithm reads

1. Start with a trivial mass distribution: $\bar{u}^E \equiv 0$.

2. For $i = 1, \ldots, N_T$ and $j = 1, \ldots, N_Q$ update the mean concentrations:

$$\bar{u}_j^E = \bar{u}_j^E + \bar{u}_i^L \frac{|T_i \cap Q_j|}{|Q_j|}. \tag{4.27}$$

3. Given a piecewise-constant $\bar{u}^E$, recover a bilinear u^E by means of a lumped-mass L_2-projection:

$$\int_\Omega u^E w \, d\mathbf{x} = \int_\Omega \bar{u}^E w \, d\mathbf{x}, \tag{4.28}$$

for all suitable weighting functions w.

In the above notation, N_T is the total number of triangles, and N_Q is the total number of quadrilaterals. Owing to the simple structure of the Eulerian

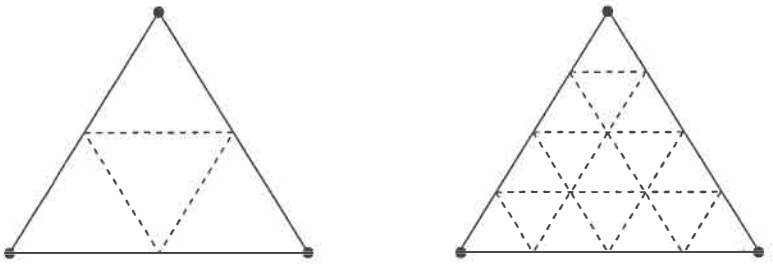

FIGURE 4.2 Refinement of a triangle into 4^k subelements ($k = 1, 2$).

mesh, it is easy to locate elements for which $T_i \cap Q_j \neq \emptyset$. The intersection of two convex polygons can be computed in linear time by the algorithm of O'Rourke *et al.* [68], [69].

The quality of our simplified mass-conserving projection depends on the ratio of mesh sizes. If the elements of the Lagrangian grid are large as compared to elements of the Eulerian grid, then we recursively subdivide each triangle T_i as shown in Figure 4.2, obtain the function values at the new nodes by interpolation and carry out (4.27) for all subelements of T_i. The mesh refinement is valid only during the projection step, so that the actual unstructured grid remains intact.

4.6 Summary of the algorithm

Our global numerical algorithm for simulation of reactive bubbly flows can be summarized as follows:

1. Initialize the variables.
2. Interpolate the gas phase velocity from the Eulerian to the Lagrangian mesh.
3. Convect the scalar quantities pertaining to the gas phase.
4. Solve the ODEs governing expansion/contraction of bubbles.
5. Project the gas holdup and the interphase mass transfer term from the Lagrangian to the Eulerian mesh.
6. Solve the Navier-Stokes equations for the liquid phase velocity and the modified pressure.

7. Compute the gas phase velocity from the dispersive slip relation.
8. Convect the effective concentrations of species in the liquid phase.
9. Solve the ODEs governing accumulation/consumption of species.
10. Go to step 2.

Remark 4.1. Different time steps can be employed for different subproblems.

Remark 4.2. The algebraic systems resulting from discretization of partial differential equations are solved iteratively by the conjugate gradient method with incomplete Cholesky preconditioning.

Remark 4.3. The reduced model based on equations (2.6) and (2.23) is handled similarly. The forward Euler method is applied to the ordinary differential equation responsible for the dwindling of the average bubble mass as a result of mass transfer into the liquid.

Chapter 5

SIMULATION OF BUBBLE COLUMN REACTORS

In this chapter, we substantiate the proposed mathematical model and numerical algorithm by selected computational results which shed some light on the implications of mass transfer and chemical reactions in bubble columns. As we are about to see, these phenomena have a strong influence on the two-phase flow hydrodynamics and vice versa.

Let us first examine a fast model reaction in a locally aerated bubble column. The apparatus dimensions and sparging pattern are the same as in the test case studied by Sokolichin *et al.* [79]. We consider a two-dimensional rectangular geometry with height 150 cm and width 50 cm. A 3 cm wide gas sparger is mounted at the bottom of the reactor at the distance of 15 cm from the left wall. It generates carbon dioxide bubbles with diameters of approximately 3 mm. The superficial gas velocity is $w_G^0 = 0.18\ mm/s$ (inflow gas holdup 1.5%). The dynamic viscosity is set equal to 0.1 $\frac{kg}{m\,s}$, which is 100 times greater than the laminar viscosity of water. We add physical effects one at a time to see what impact they have on the two-phase flow in the bubble column. All results were obtained with an Eulerian mesh of 50×150 bilinear elements. For illustrative purposes, the velocity fields are plotted at a halved spatial resolution.

If there is no bubble path dispersion and the bubble radius is constant, the gas holdup distribution 5 seconds after the onset of aeration looks as shown in Figure 5.1 (left). It is displayed as defined on the Eulerian mesh after the projection. The Lagrangian mesh evolves in essentially the same manner, see Figure 5.1 (right). Similar mushroom-like shapes of the bubble plume during the first seconds of simulation were reported in [19], [50], [79]. Snapshots visualizing the developing flow are presented in Figure 5.2.

Transient circulating flows arise in the upper part of the bubble column, but in the lower part the bubble swarm is invariably heading towards the left wall. This fact was also established experimentally by Becker *et al.* [2]. The void fraction distribution and the liquid phase velocity field one minute after the startup of the bubble column are depicted in Figure 5.3. Three large circulation cells are also observed at later times. Simulation results with bubble path dispersion are presented in Figures 5.4 and 5.5. Dispersion in the vertical direction is assumed to be negligible: $D_1 = 0$. In the horizontal direction, the diffusion coefficient is taken to be $D_2 = 1.04167\ cm^2/s$ [79]. We witness a considerable increase in the spread of the bubble plume, but little differences in the overall flow structure. At lower viscosities, smaller vortices are resolved. They continuously change their size and location, and the flow exhibits a highly dynamic behavior.

Next, we activate the model for expansion and shrinkage of bubbles. In the absence of mass transfer, the bubble radius increases linearly with height, see Figure 5.6. By the time a bubble reaches the top of the reactor, its volume gains as much as 14.5%, and so does the local gas holdup. Under different operating conditions, the bubble expansion can be even more pronounced. Physical absorption with a constant mass transfer coefficient $k_L^0 = 1 \times 10^{-4}\ m/s$ proceeds as shown in Figures 5.8–5.10, which depict the gas holdup distribution, liquid phase velocity fields and effective concentration of the dissolved gas at several time instants. Due to the high solubility of CO_2 in water, the bubble radius at the outlet falls short of its value at the inlet in this case, see Figure 5.7. However, physical absorption alone is ostensibly insufficient to alter the flow patterns significantly.

Consider the dissolution of carbon dioxide in an aqueous solution of sodium hydroxide with simultaneous second-order chemical reaction

$$CO_2 + 2NaOH \rightarrow Na_2CO_3 + H_2O$$

in the liquid phase. The employed reaction rate constant is $k_2 = 10 \frac{m^3}{mol\ s}$. In our general notation (2.35), the stoichiometric coefficient of the reactant B is 2, and that of the product P equals unity. This is a handy model reaction, since it is fast enough to effect considerable gas consumption and thereby bring about remarkable changes in the two-phase flow characteristics. We corroborate this statement by the following example.

Let the initial molarity of the solution be 1 M NaOH. This implies that the bubble column is operated at Hatta numbers $Ha \approx 42.5$ and enhancement factors as large as $E \approx 16$. Hence, the mass transfer is immensely accelerated by chemical reaction, so that the local gas holdup rapidly diminishes with height. According to Figure 5.11, the absorption rate is so

high that the bubbles are completely dissolved at distances greater than 20 cm from the inlet. Consequently, the liquid circulation, mass transfer and chemical reaction take place only in the lower part of the reactor as demonstrated by Figures 5.12 and 5.13. The distribution of sodium carbonate gradually evolves into distinctive snail-like spirals.

If the bubble column is aerated uniformly over its entire bottom, two qualitatively different operating states can be distinguished [10]. At low superficial gas velocities, the bubbles rise uniformly through an essentially stagnant liquid. This is known as the homogeneous flow regime. At high gas throughputs, the two-phase flow switches over to the so-called heterogeneous regime which is characterized by radial gas holdup gradients and a highly irregular motion of randomly appearing vortices. A long-time averaging of velocity fields unveils a regular flow structure with liquid upflow in the center and downflow near the walls, which is well known from experimental studies [50], [78]. As a rule of thumb, the heterogeneous flow regime can be expected at superficial gas velocities above 2 cm/s [79]. Simulation results for the reaction enhanced dissolution of carbon dioxide in a uniformly aerated bubble column were obtained using an Eulerian mesh of 30×90 elements. Bubble path dispersion was neglected in this case.

For moderate gas throughputs ($w_G^0 = 2\ mm/s$), the homogeneous flow regime is preserved even in a strongly reactive environment. Figure 5.14 shows that in case of a high NaOH content the lifetime of a bubble is as small as for the locally aerated bubble column, so that the upper part of the reactor is totally free of gas. The radial gas holdup profiles are flat. The synthesized sodium carbonate is layered in the vicinity of the gas sparger, see Figure 5.15. This kind of reactor behavior marked by the formation of sharp bubble and reaction fronts was also observed by Fleischer *et al.* [21], who investigated the chemisorption of CO_2 into an aqueous solution of NaOH by means of measurements and one-dimensional dynamic numerical simulation. With time, sodium hydroxide in the reaction zone is used up and the fronts slowly move upwards through the bubble column. However, a considerable amount of time elapses before the first bubbles make it to the top of the reactor.

If the superficial gas velocity is increased to the threshold value of 2 cm/s, while the initial concentration of NaOH is kept equal to 1 M, then the void fraction is no longer constant within a reactor cross-section, see Figure 5.16. Due to the fast gas absorption, there is no liquid circulation in the upper part of the bubble column, but instabilities develop close to the gas distributor. Eventually, the gas holdup profiles assume saddle-like shapes and two medium-size vortices are formed as shown in Figure 5.17. They are

responsible for the mixing processes leading to the concentration profiles depicted in Figure 5.18.

Finally, let us devalue the initial concentration of sodium hydroxide to 0.2 M. Figure 5.19 indicates that even though there is no effluent gas flow, in this case the bubbles can travel a relatively long distance before they are completely dissolved. This results in a pronounced liquid circulation which abates with height, see Figure 5.20. The instantaneous concentration fields presented in Figure 5.21 illustrate the progress of backmixing in the liquid phase.

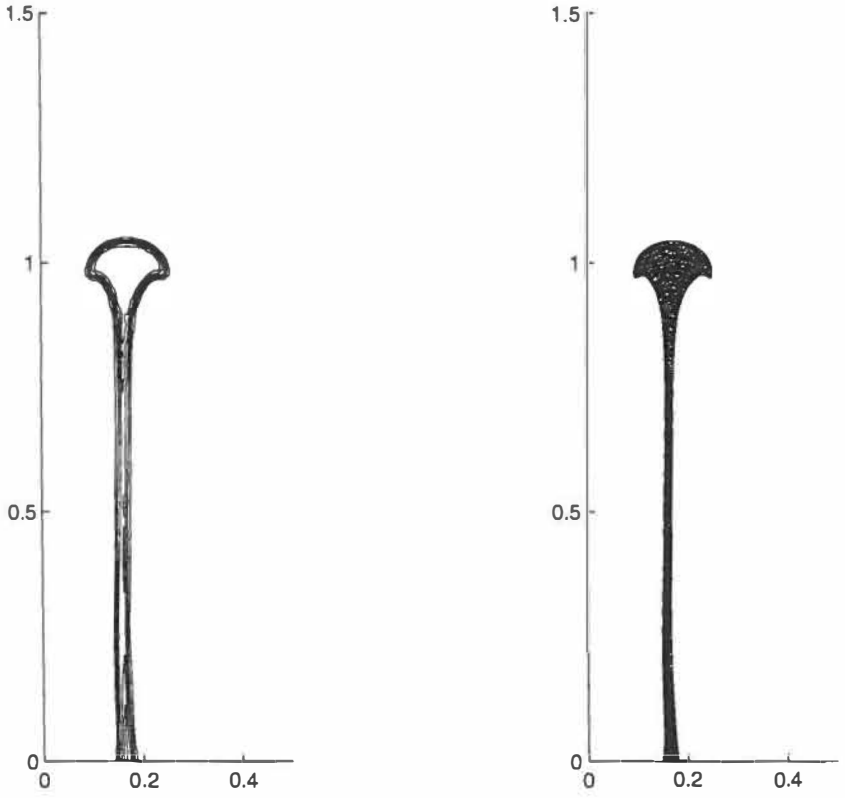

FIGURE 5.1 Gas holdup distribution and Lagrangian mesh at $t = 5$ s, without bubble path dispersion.

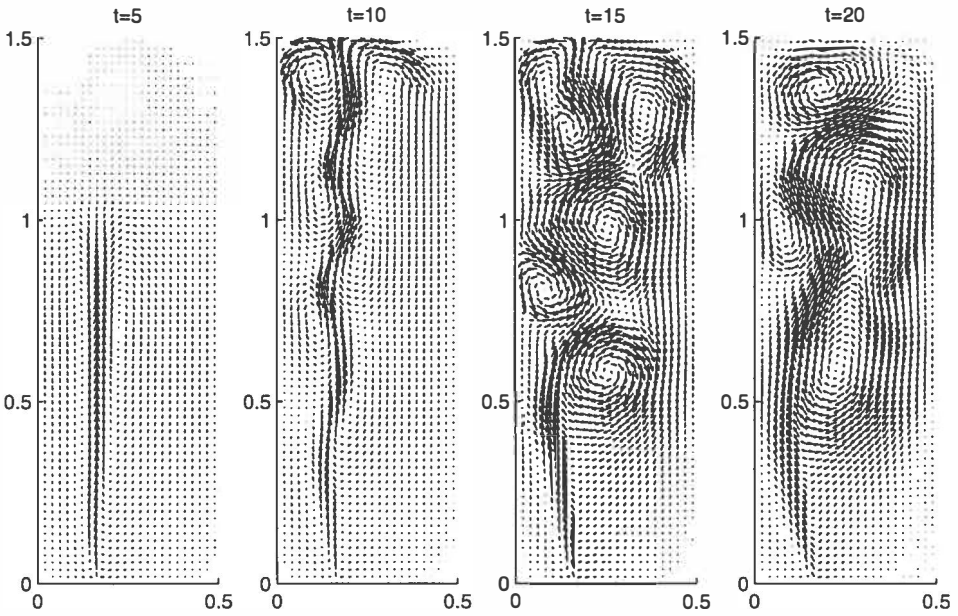

FIGURE 5.2 Startup of a locally aerated bubble column, without bubble path dispersion.

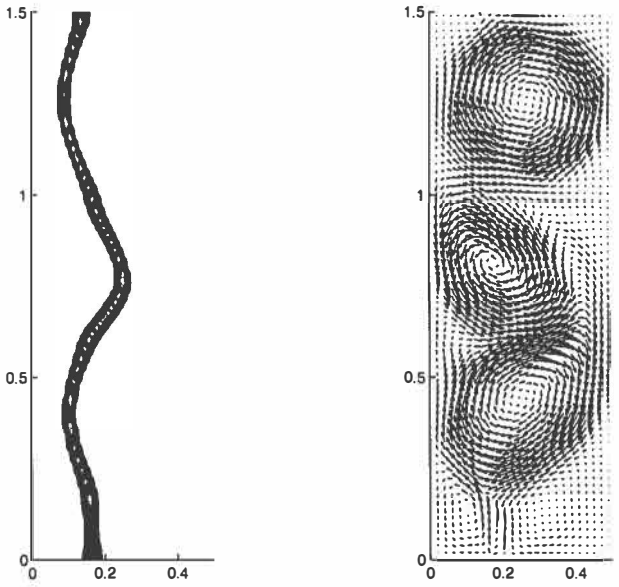

FIGURE 5.3 Gas holdup distribution and velocity field at $t = 60\ s$, without bubble path dispersion.

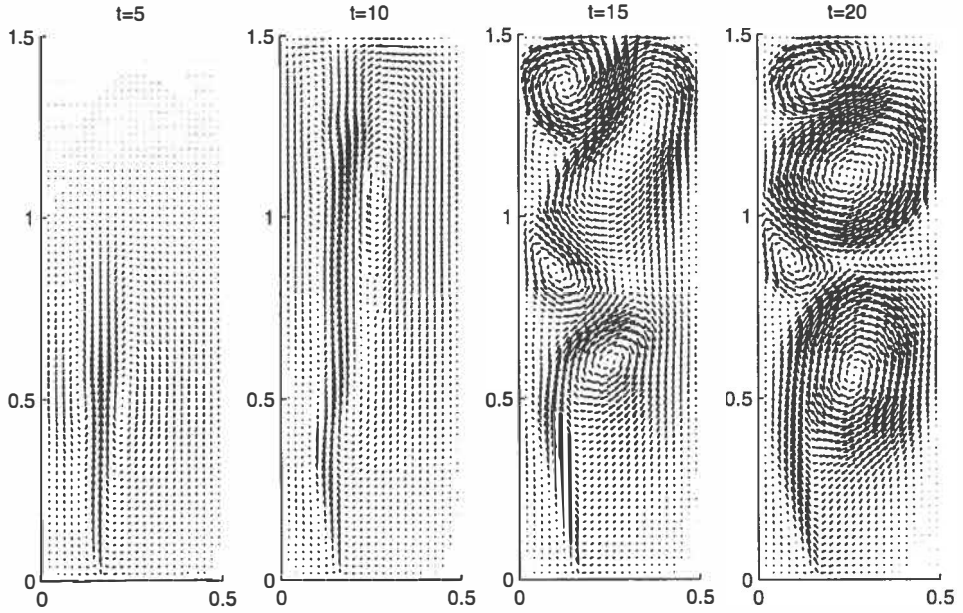

FIGURE 5.4 Startup of a locally aerated bubble column, with bubble path dispersion.

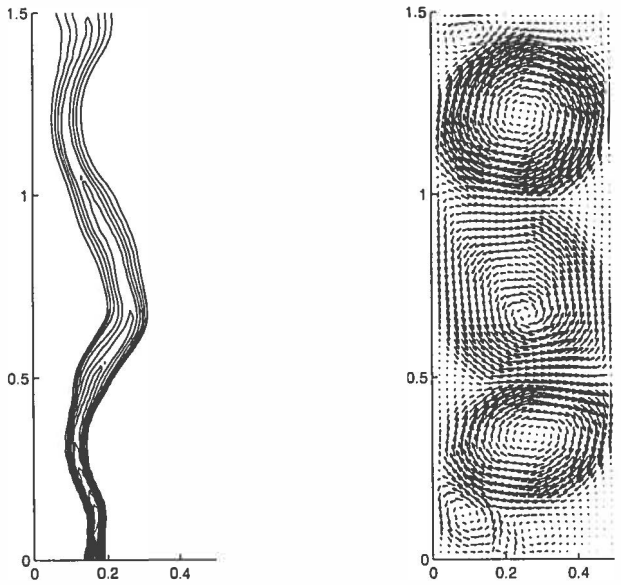

FIGURE 5.5 Gas holdup distribution and velocity field at $t = 60$ s, with bubble path dispersion.

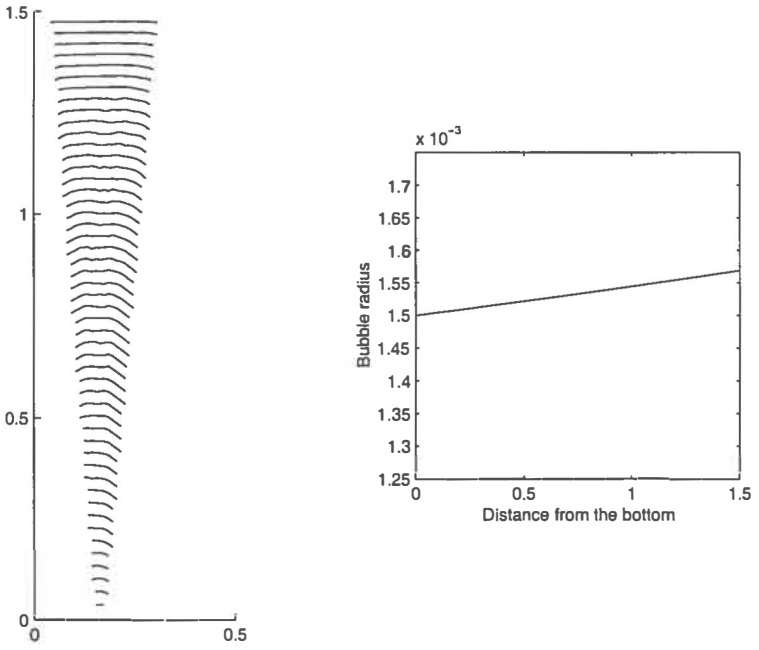

FIGURE 5.6 Bubble size distribution at $t = 10\ s$ (left) and evolution of the radius of a single rising bubble (right), no absorption.

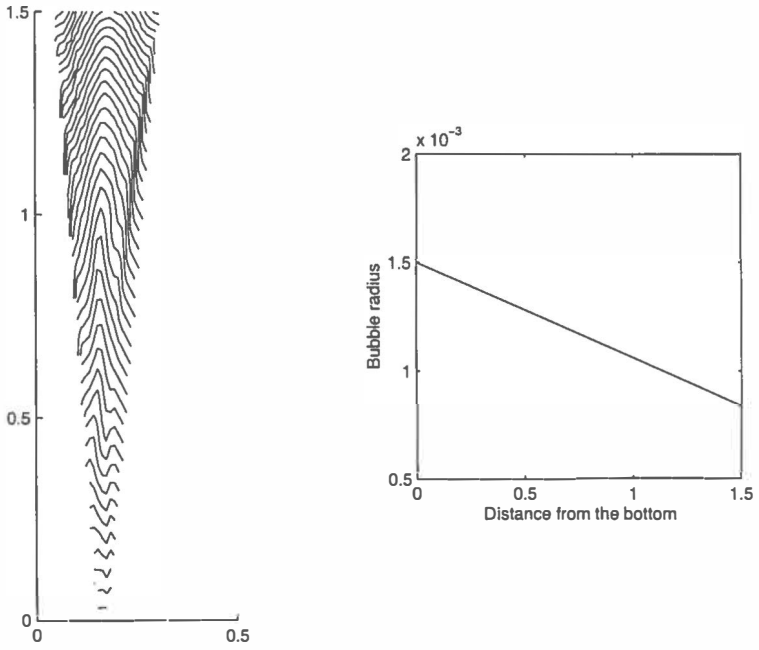

FIGURE 5.7 Bubble size distribution at $t = 10\ s$ (left) and evolution of the radius of a single rising bubble (right), physical absorption.

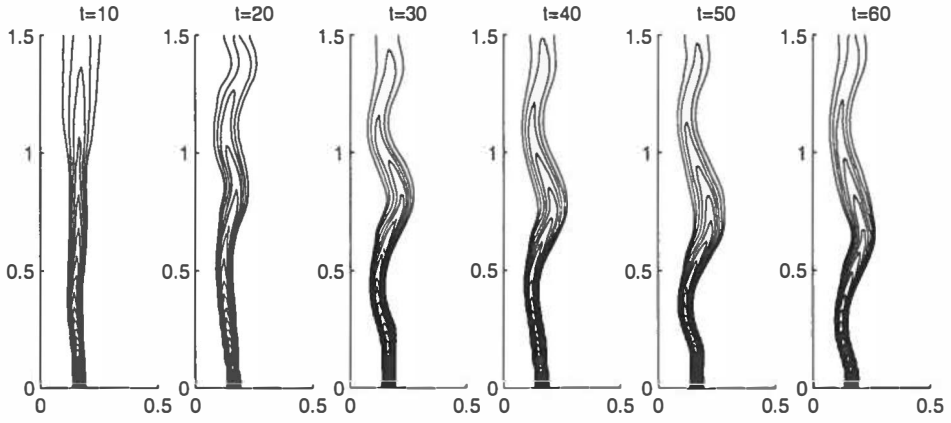

FIGURE 5.8 Gas holdup distribution, physical absorption.

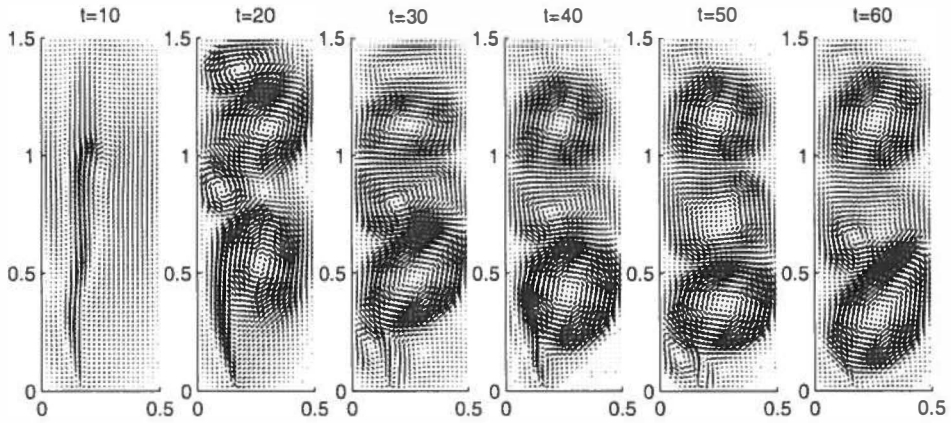

FIGURE 5.9 Velocity fields, physical absorption.

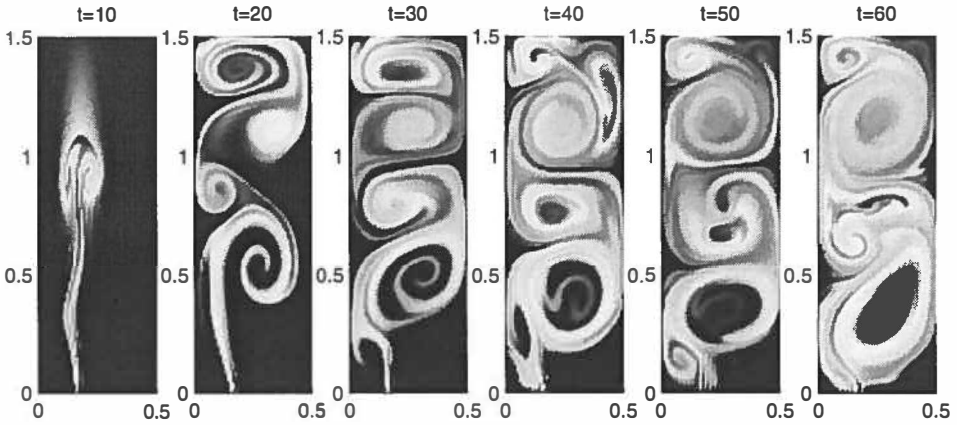

FIGURE 5.10 Effective concentration of CO_2, physical absorption.

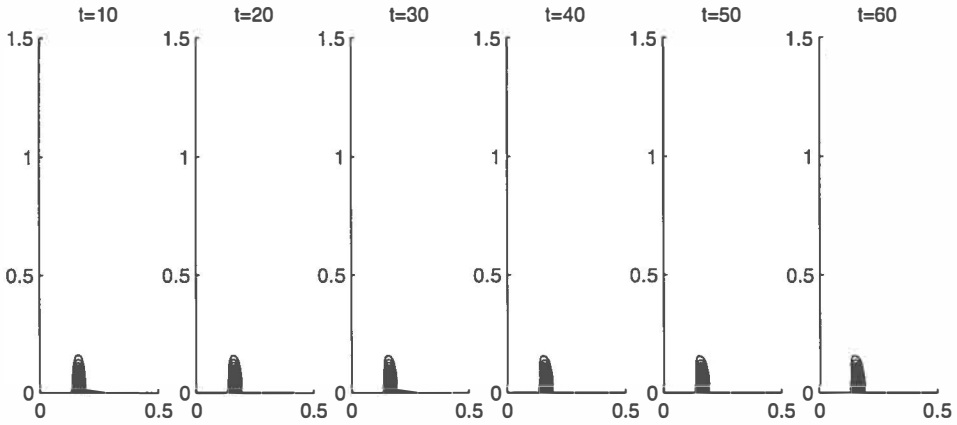

FIGURE 5.11 Gas holdup distribution, $c^0_{\mathrm{NaOH}} = 1\ mol/l$.

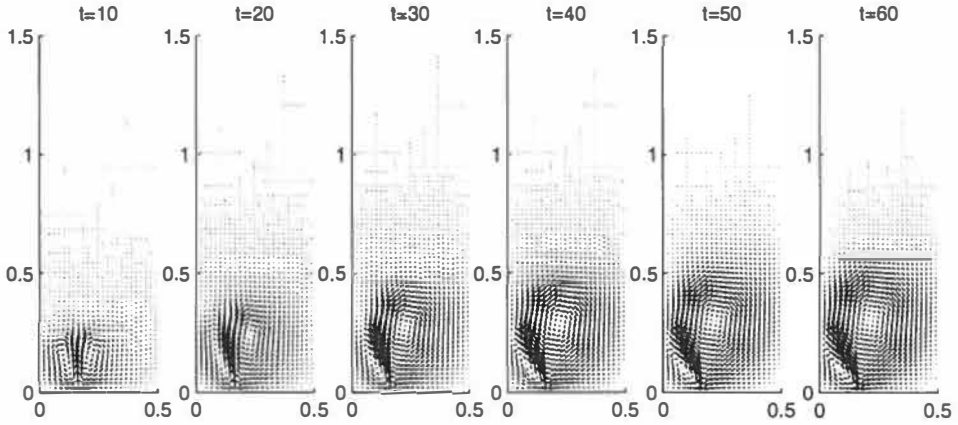

FIGURE 5.12 Velocity fields, $c^0_{\mathrm{NaOH}} = 1\ mol/l$.

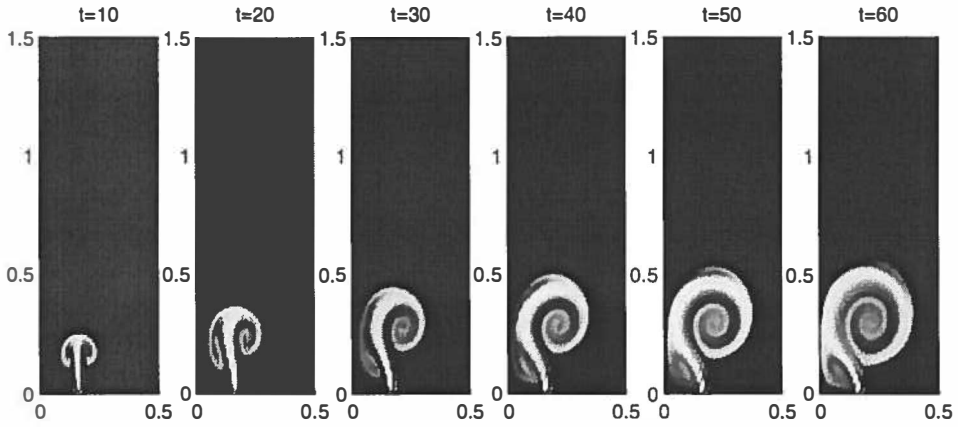

FIGURE 5.13 Effective concentration of Na_2CO_3, $c^0_{\mathrm{NaOH}} = 1\ mol/l$.

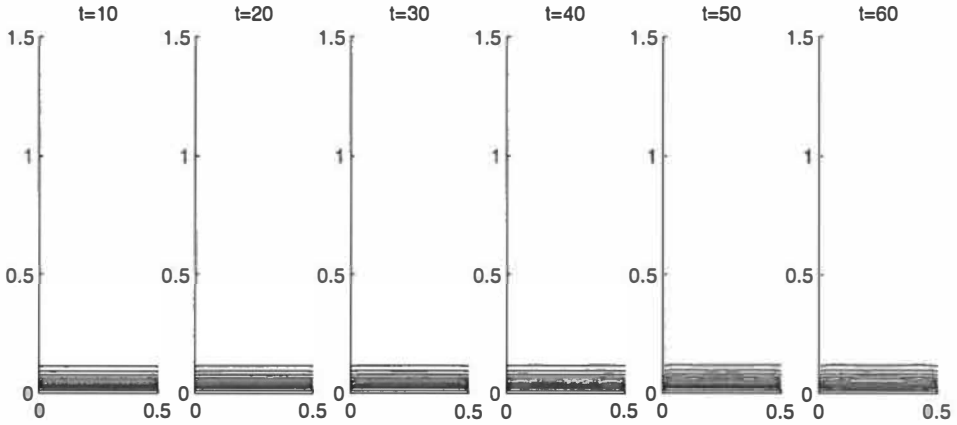

FIGURE 5.14 Gas holdup distribution, $c^0_{\mathrm{NaOH}} = 1\ mol/l,\ w^0_G = 2\ mm/s$.

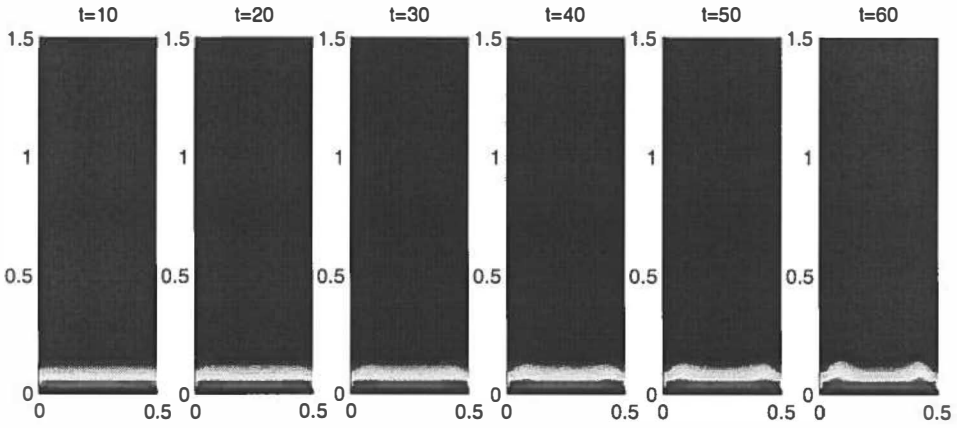

FIGURE 5.15 Effective concentration of Na_2CO_3, $c^0_{\mathrm{NaOH}} = 1\ mol/l,\ w^0_G = 2\ mm/s$.

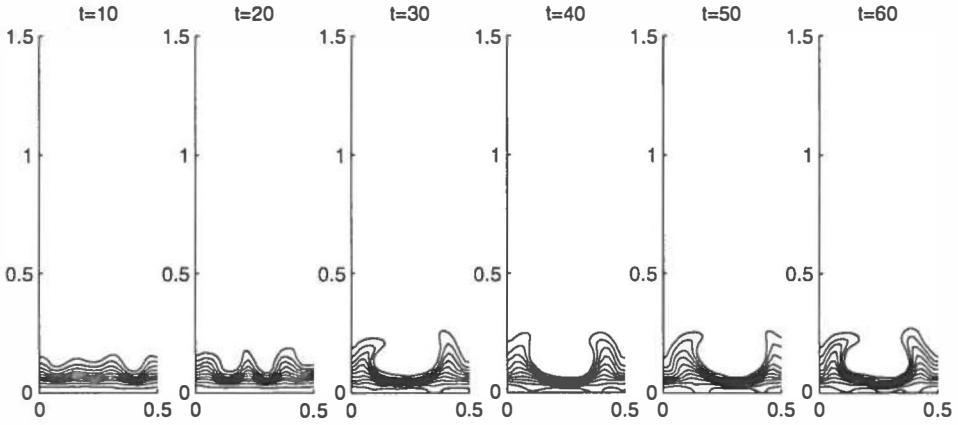

FIGURE 5.16 Gas holdup distribution, $c^0_{\mathrm{NaOH}} = 1\ mol/l,\ w^0_G = 2\ cm/s.$

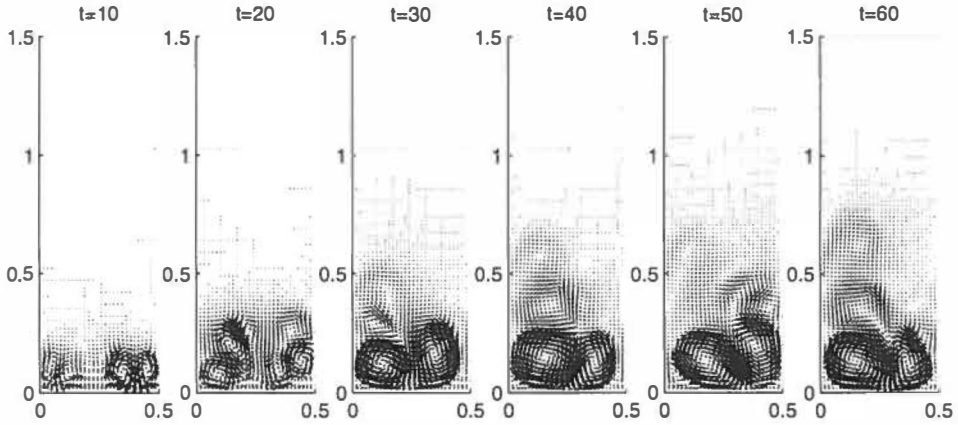

FIGURE 5.17 Velocity fields, $c^0_{\mathrm{NaOH}} = 1\ mol/l,\ w^0_G = 2\ cm/s.$

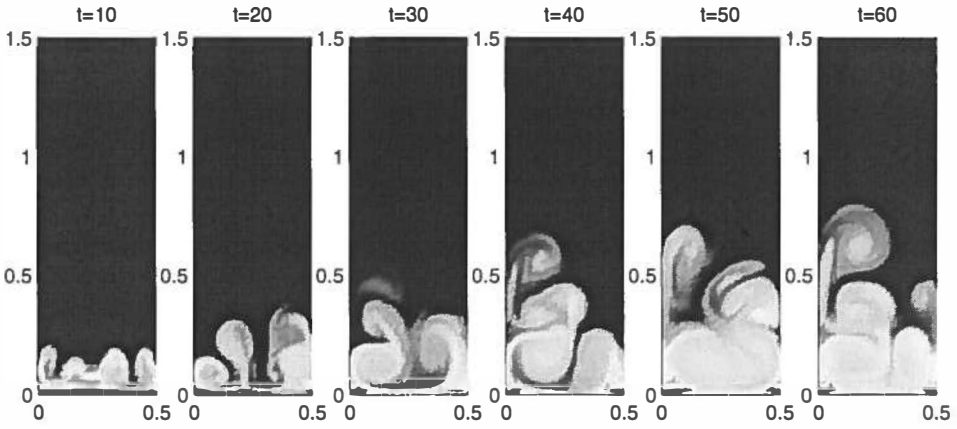

FIGURE 5.18 Effective concentration of Na_2CO_3, $c^0_{NaOH} = 1\ mol/l,\ w^0_G = 2\ cm/s$

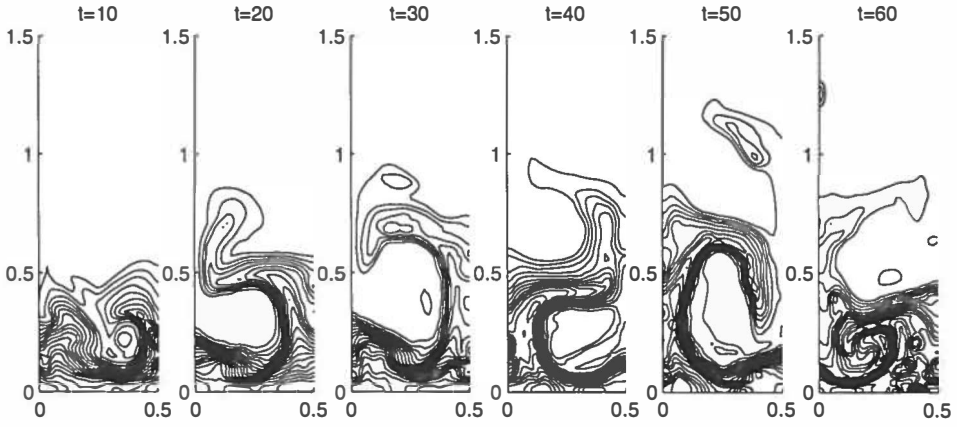

FIGURE 5.19 Gas holdup distribution, $c^0_{NaOH} = 0.2\ mol/l,\ w^0_G = 2\ cm/s$.

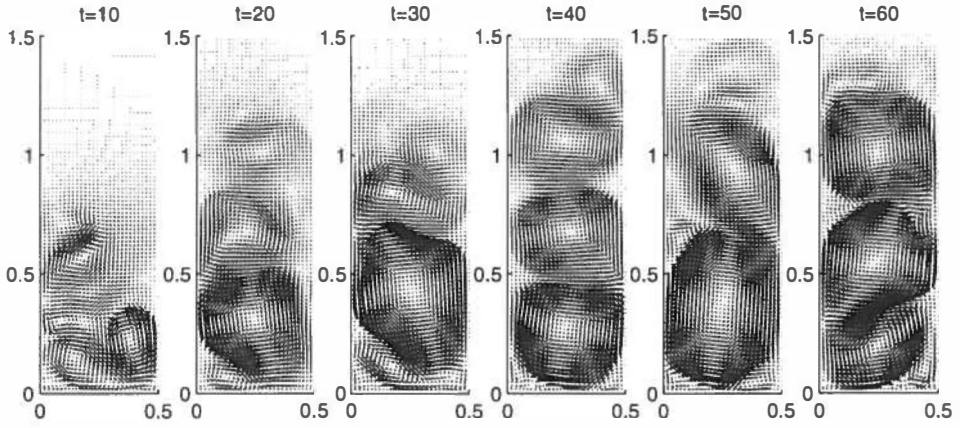

FIGURE 5.20 Velocity fields, $c^0_{\mathrm{NaOH}} = 0.2\ mol/l,\ w^0_G = 2\ cm/s$.

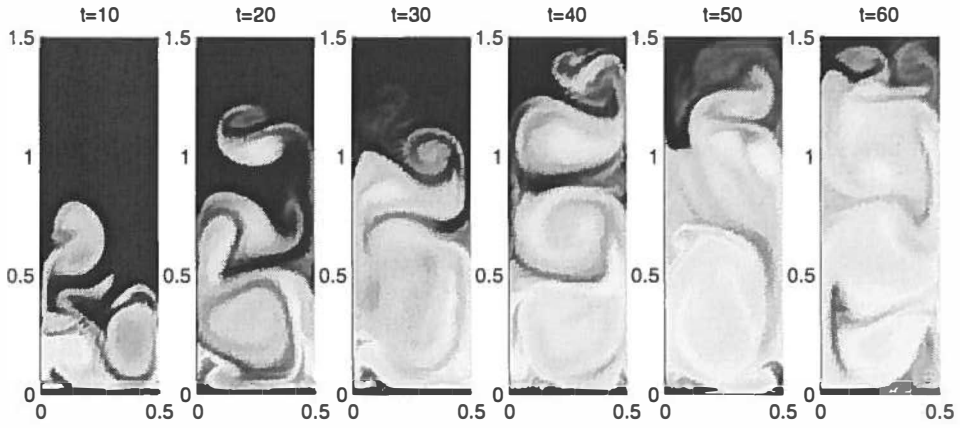

FIGURE 5.21 Effective concentration of Na_2CO_3, $c^0_{\mathrm{NaOH}} = 0.2\ mol/l$, $w^0_G = 2\ cm/s$.

Chapter 6

CONCLUDING REMARKS

In this thesis, we endeavored to develop and implement a mathematical model for unsteady gas-liquid flow in a bubble column reactor. Its major highlight was the coupling of fluid dynamics with gas absorption enhanced by chemical reaction in the liquid phase. Evolution of the bubble radius due to pressure variations and mass transfer into the liquid was taken into account by means of the classical Rayleigh-Plesset equation. An alternative formulation based on the common pressure assumption and a balance equation for the average bubble mass was also proposed. In either case, the impact of gas dissolution and pressure drop on the bubble size was captured duly without consideration of multiple bubble classes [78] albeit at the price of monitoring the evolution of the domain actually occupied by gas. As far as the numerical simulation is concerned, emphasis was laid on the development and improvement of finite element solution techniques. The presented computational results indicate that the model reproduces all essential features of the two-phase flow and provides a correct qualitative description of processes inside the reactor. A strong interdependence of the hydrodynamics, mass transfer and chemical reaction phenomena was established. Some feasible directions for further research are outlined below.

Even though two-fluid models using the Rayleigh-Plesset equation of bubble dynamics to describe the joint deformation of phases emerged in the literature as early as two decades ago [38], [57], the then computing power and state of the art of numerical methods inhibited their realization in bubbly flow simulation software. In order to solve the arising moving boundary problem, we had to employ a laborious Lagrangian space-time finite element method which curtails numerical diffusion in the gas phase and possesses remarkable conservation properties. However, a formidable bottleneck of this procedure is its vulnerability to strongly nonuniform flow

patterns. It can also be envisioned that the presence of built-in internals can become an obstacle from the computational standpoint. This severely limits the range of operating conditions and reactor geometries that can be tackled. Therefore, the Lagrangian approach should be eventually superseded by high-resolution Eulerian methods as applied to systems like (2.4)-(2.5). This would introduce the bubble mass as an additional coordinate but eliminate considerable overhead costs connected with handling the evolution of the Lagrangian mesh. Furthermore, sound mathematical models for coalescence and breakup of bubbles should be devised and incorporated into the equation for the bubble size distribution function. Common sense and experimental observations suggest that these phenomena can play an important role in bubble columns, especially at high superficial gas velocities. Specifically, coalescence can dramatically change the primary bubble size distribution and even counterbalance the shrinkage of bubbles due to mass transfer into the liquid [27], [36]. Direct numerical simulation of multiple bubbles [20], [89] offers a way to construct realistic closure models for the macroscopic equations.

The model studied in this thesis is fairly complex, but it involves several major simplifications and encompasses only a fraction of physical and chemical effects that can be pertinent to a concrete gas-liquid system. For instance, the presence of an inert gas component can hamper mass transfer, cause a mixing of the liquid phase in regions that would otherwise be gas-free and impede the development of bubble and reaction fronts [1]. Chemical reactions often generate or consume heat thereby altering the physical properties of both phases. Thus, in some cases it is necessary to consider the two-phase flow thermodynamics and supply models for the interphase heat transfer. The rich variety of equipment employed in chemical industry is not limited to empty bubble columns. Building on the acquired background, we can turn to investigation of airlift loop or three-phase slurry reactors.

By far the most challenging problem in multiphase fluid dynamics is a proper modeling of turbulence. Reynolds stresses arise in the two-fluid model during the averaging process. In this thesis, they were omitted, since the liquid viscosity was chosen sufficiently large to dampen velocity fluctuations on the microscopic scale. If the laminar model is applied at high Reynolds numbers and the numerical simulation is carried out using increasingly fine spatial meshes, then vortices are resolved which are comparable in size with the diameter of a single bubble. This contradicts to one of the fundamental assumptions underlying the macroscopic model. Hence, the Reynolds stresses must be expressed in terms of averaged quantities and inserted into the momentum equations. However, no unambiguous relation-

ship is available to date. Due to the lack of understanding of mechanisms governing the turbulent gas-liquid flow, single-phase turbulence models are commonly employed [28], [65], [74], [85]. In particular, the standard $k-\epsilon$ model was reported to yield a reasonable agreement with experimental data. As a matter of fact, a three-dimensional simulation is required to obtain realistic results. If the influence of the third dimension is neglected, the effective viscosity is overestimated by orders of magnitude rendering the numerical solution quasi-stationary [19]. The bubble-induced turbulence is sometimes taken into consideration by extra source terms in the transport equations for the turbulent kinetic energy k and its dissipation rate ϵ [3], [37], [80]. Nevertheless, turbulence in the bubbly flow regime remains a relatively unexplored area, so that there is a lot of room for research.

A dynamic three-dimensional numerical simulation with bubble size distribution being a function of the time, spatial coordinates and the bubble mass would entail a substantial increase in computational cost. Therefore, additional effort must be invested into the enhancement of robustness and efficiency of numerical techniques. In particular, it is expedient to incorporate an error-based time step control and $h-p$ adaptivity. The solution of algebraic systems resulting from the finite element discretization can be greatly accelerated by resorting to multigrid methods.

LIST OF SYMBOLS

a	bubble radius	m
c	molar concentration	mol/m^3
c^*	gas solubility	mol/m^3
C_D	drag coefficient	—
C_L	lift coefficient	—
C_{VM}	virtual mass coefficient	—
C_W	drag force constant	$kg/(m^3 s)$
D	diffusion coefficient	m^2/s
E	enhancement factor	—
f	bubble size distribution	m^{-3}
g	gravitational acceleration	m/s^2
h	reactor height	m
H	Henry's law coefficient	J/mol
Ha	Hatta number	—
k_1	first-order reaction rate constant	s^{-1}
k_2	second-order reaction rate constant	$m^3/(mol\ s)$
k_L	liquid-side mass transfer coefficient	m/s
k_L^0	physical mass transfer coefficient	m/s
m	bubble mass	kg
n	number density	m^{-3}
$\mathcal{N}$	molar flux	$mol/(m^2 s)$
p	pressure	N/m^2
P	modified pressure	m^2/s^2
Pe	Peclet number	—
R	gas constant	$J/(K\ mol)$
Re	Reynolds number	—
Sc	Schmidt number	—
t	time	s
T	temperature	K
$\mathbf{v}$	velocity	m/s
w	radial velocity	m/s
w_G^0	superficial gas velocity	m/s
$\mathbf{x}$	spatial coordinates	m

Greek letters

ϵ	gas holdup	—
η	molar mass	kg/mol
μ	dynamic viscosity	$kg/(m\ s)$
ν	kinematic viscosity	m^2/s
ν_B	stoichiometric coefficient for reactant	—
ν_P	stoichiometric coefficient for product	—
ξ	correction coefficient	—
ρ	density	kg/m^3
σ	surface tension	N/m

Subscripts

A	component A
B	component B
G	gas
L	liquid
P	component P

BIBLIOGRAPHY

[1] S. Becker, *Experimentelle Untersuchungen von Blasensäulen als Basis für detallierte Modellrechnungen.* VDI-Verlag, 1997.

[2] S. Becker, A. Sokolichin and G. Eigenberger, Gas-liquid flow in bubble columns and loop reactors: Part II. Comparison of detailed experiments and flow simulations. *Chem. Eng. Sci.* **49** (1994), no. 24B, 5747–5762.

[3] N. Boisson and M. R. Malin, Numerical prediction of two-phase flow in bubble columns. *Int. J. Numer. Meth. Fluids* **23** (1996) 1289–1310.

[4] J. P. Boris and D. L. Book, Flux-corrected transport. I. SHASTA, A fluid transport algorithm that works. *J. Comput. Phys.* **11** (1973) 38–69.

[5] F. Brezzi and J. Pitkäranta, On the stabilization of finite element approximations of the Stokes equations. In: *Efficient Solutions of Elliptic Systems*, Notes Numer. Fluid Mech. **10**, Vieweg & Sohn, Braunschweig, 1984, 11–19.

[6] A. J. Chorin, Numerical solution of the Navier-Stokes equations. *Math. Comp.* **22** (1968) 745–762.

[7] A. J. Chorin, On the convergence of discrete approximations to the Navier-Stokes equations. *Math. Comp.* **23** (1969) 341–353.

[8] R. Clift, J. R. Grace and M. E. Weber, *Bubbles, Drops and Particles.* Academic Press, 1978.

[9] P. V. Danckwerts, *Gas-Liquid Reactions.* McGraw-Hill, 1970.

[10] W.-D. Deckwer, *Bubble Column Reactors.* John Wiley & Sons, 1992.

[11] E. Delnoij, F. A. Lammers, J. A. M. Kuipers and W. P. M. van Swaaij, Dynamic simulation of dispersed gas-liquid two-phase flow using a discrete bubble model. *Chem. Eng. Sci.* **52** (1997), no. 9, 1429–1458.

[12] J. Donea, A Taylor-Galerkin method for convective transport problems. *Int. J. Numer. Meth. Engrg.* **20** (1984) 101–119.

[13] J. Donea, S. Giuliani, H. Laval and L. Quartapelle, Finite element solution of the unsteady Navier-Stokes equations by a fractional step method. *Comput. Meth. Appl. Mech. Engrg.* **30** (1982) 53–73.

[14] J. Donea, S. Giuliani, H. Laval and L. Quartapelle, Time-accurate solution of advection-diffusion problems by finite elements. *Comput. Meth. Appl. Mech. Engrg.* **45** (1984) 123–145.

[15] J. Donea and L. Quartapelle, An introduction to finite element methods for transient advection problems. *Comput. Meth. Appl. Mech. Engrg.* **95** (1992) 169–203.

[16] J. Donea, L. Quartapelle and V. Selmin, An analysis of time discretization in the finite element solution of hyperbolic problems. *J. Comput. Phys.* **70** (1987) 463–499.

[17] D. A. Drew, Mathematical modeling of two-phase flow. *Ann. Rev. Fluid Mech.* **15** (1983) 261-291.

[18] D. A. Drew and S. L. Passman, *Theory of Multicomponent Fluids.* Springer, 1999.

[19] G. Eigenberger and A. Sokolichin, Modellierung und effiziente numerische Simulation von Gas-Flüssigkeits-Reaktoren mit Blasenströmungen nach dem Euler-Euler-Konzept. DFG-Zwischenbericht (1995–1997), *http://pcvt12.verfahrenstechnik.uni-stuttgart.de/alex/icvt2.html.*

[20] A. Esmaeeli, E. Ervin and G. Tryggvason, Numerical simulations of rising bubbles. In: *Bubble Dynamics and Interface Phenomena*, Kluwer Academic Publishers, 1994, 247–255.

[21] C. Fleischer, S. Becker and G. Eigenberger, Detailed modeling of the chemisorption of CO_2 into NaOH in a bubble column. *Chem. Eng. Sci.* **51** (1996), no. 10, 1715–1724.

[22] U. Ghia, K. N. Ghia and C. T. Shin, High-Re solutions for incompressible flow using the Navier-Stokes equations and a multigrid method. *J. Comput. Phys.* **48** (1982) 387–411.

[23] P. M. Gresho, On the theory of semi-implicit projection methods for viscous incompressible flow and its implementation via a finite element method that also introduces a nearly consistent mass matrix. Part 1: Theory. *Int. J. Numer. Methods Fluids* **11** (1990), no. 5, 587–620.

[24] P. M. Gresho and S. T. Chan, On the theory of semi-implicit projection methods for viscous incompressible flow and its implementation via a finite element method that also introduces a nearly consistent mass matrix. Part 2: Implementation. *Int. J. Numer. Methods Fluids* **11** (1990), no. 5, 621–659.

[25] P. M. Gresho and R. L. Sani, On pressure boundary conditions for the incompressible Navier-Stokes equations. *Int. J. Numer. Methods Fluids* **7** (1987) 1111–1145.

[26] P. M. Gresho and R. L. Sani (in collaboration with M. S. Engelman), *Incompressible Flow and the Finite Element Method.* John Wiley & Sons, 1998.

[27] J. Grienberger, *Untersuchung und Modellierung von Blasensäulen.* Dissertation, Erlangen-Nürnberg, 1992.

[28] J. Grienberger and H. Hofmann, Investigations and modelling of bubble columns. *Chem. Eng. Sci.* **47** (1992), no. 9-11, 2215–2220.

[29] J.-L. Guermond and L. Quartapelle, On stability and convergence of projection methods based on pressure Poisson equation. *Int. J. Numer. Methods Fluids* **26** (1998) 1039–1053.

[30] P. Hansbo, The characteristic streamline diffusion method for convection-diffusion problems. *Comput. Methods Appl. Mech. Engrg.* **96** (1992) 239–253.

[31] P. Hansbo, The characteristic streamline diffusion method for the time-dependent incompressible Navier-Stokes equations. *Comput. Methods Appl. Mech. Engrg.* **99** (1992) 171–186.

[32] P. Hansbo, Space-time oriented streamline diffusion methods for nonlinear conservation laws in one dimension. *Commun. Numer. Methods Engrg.* **10** (1994) 203–215.

[33] P. Hansbo, Aspects of conservation in finite element flow computations. *Comput. Methods Appl. Mech. Engrg.* **117** (1994) 423–437.

[34] P. Hansbo, Lagrangian incompressible flow computations in three dimensions by use of space-time finite elements. *Int. J. Numer. Methods Fluids* **20** (1995) 989–1001.

[35] P. Hansbo, A free-Lagrange finite element method using space-time elements. Preprint, *http://www.solid.chalmers.se/hansbo/publications.html.*

[36] G. Hillmer, *Experimentelle Untersuchung und fluiddynamische Modellierung von Suspensionsblasensäulen.* Dissertation, Erlangen-Nürnberg, 1993.

[37] B. H. Hjertager and K. Morud, Computational fluid dynamics simulation of bioreactors. *Mod. Ident. Control* **16** (1995), no. 4, 177–191.

[38] D. Y. Hsieh, Some aspects of dynamics of bubbly liquids. *Appl. Sci. Res.* **38** (1982) 305–312.

[39] C. Johnson, *Numerical Solutions of Partial Differential Equations by the Finite Element Method.* Studentlitteratur, 1987.

[40] C. Johnson, The characteristic streamline diffusion finite element method. *Mat. Aplic. Comp.* **10** (1991), no. 3, 229–242.

[41] C. Johnson, A new approach to algorithms for convection problems which are based on exact transport + projection. *Comput. Methods Appl. Mech. Engrg.* **100** (1992) 45–62.

[42] J. van Kan, A second-order accurate pressure-correction scheme for viscous incompressible flow. *SIAM J. Sci. Statist. Comput.* **7** (1986), no. 3, 870–891.

[43] P. Kaps and P. Rentrop, Generalized Runge-Kutta methods of order four with stepsize control for stiff ordinary differential equations. *Numer. Math.* **33** (1979) 55–68.

[44] J. M. Kay and R. M. Nedderman, *Fluid Mechanics and Transfer Processes.* Cambridge University Press, 1985.

[45] D. W. van Krevelen and P. J. Hoftijzer, *Rec. Trav. Chim.* **67** (1948) 563.

[46] M. Křižek and P. Neittaanmäki, Superconvergence phenomenon in the finite element method arising from averaging gradients. *Numer. Math.* **45** (1984) 105–116.

[47] M. Křižek and P. Neittaanmäki, *Finite Element Approximation of Variational Problems and Applications.* Longman Scientific & Technical, 1990.

[48] D. Kuzmin, The free-Lagrange FEM for problems in time-dependent domains: Boundary discretization. To appear in: proceedings of the *AABVP Meeting*, University of Jyväskylä, 1999.

[49] O. A. Ladyzhenskaya, *The Mathematical Theory of Viscous Incompressible Flow.* Gordon and Breach, New York, 1969.

[50] A. Lapin and A. Lübbert, Numerical simulation of the dynamics of two-phase gas-liquid flows in bubble columns. *Chem. Eng. Sci.* **49** (1994), no. 21, 3661–3674.

[51] H. Laval and L. Quartapelle, A fractional-step Taylor-Galerkin method for unsteady incompressible flows. *Int. J. Numer. Meth. Fluids* **11** (1990) 501–513.

[52] R. Löhner, Robust, vectorized search algorithms for interpolation on unstructured grids. *J. Comput. Phys.* **118** (1995) 380–387.

[53] R. Löhner, K. Morgan, J. Peraire and M. Vahdati, Finite element flux-corrected transport (FEM-FCT) for the Euler and Navier-Stokes equations. *Int. J. Numer. Meth. Fluids* **7** (1987) 1093–1109.

[54] R. Löhner, K. Morgan, M. Vahdati, J. P. Boris and D. L. Book, FEM-FCT: combining unstructured grids with high resolution. *Commun. Appl. Numer. Methods* **4** (1988) 717–729.

[55] G. I. Marchuk, *Methods of Numerical Mathematics.* Springer, 1975.

[56] A. Masud and T. J. R. Hughes, A space-time Galerkin/least-squares finite element formulation of the Navier-Stokes equations for moving domain problems. *Comput. Methods Appl. Mech. Engrg.* **146** (1997) 91–126.

[57] R. I. Nigmatulin, *Foundations of the Mechanics of Heterogeneous Media* (in Russian). Nauka, Moscow, 1978.

[58] R. I. Nigmatulin, *Dynamics of Multiphase Media.* Hemisphere, 1991.

[59] A. K. Parrott and M. A. Christie, FCT applied to the 2-D finite element solution of tracer transport by single phase flow in a porous medium. In: proceedings of the *ICFD Conference on Numerical Methods in Fluid Dynamics*, Oxford University Press, 1986, 609–619.

[60] J. Peraire, M. Vahdati, K. Morgan and O. C. Zienkiewicz, Adaptive remeshing for compressible flow computations. *J. Comput. Phys.* **72** (1987) 449-466.

[61] A. Prohl, *Projection and Quasi-Compressibility Methods for Solving the Incompressible Navier-Stokes Equations.* Advances in Numerical Mathematics. B. G. Teubner, Stuttgart, 1997.

[62] L. Quartapelle, *Numerical Solution of the Incompressible Navier-Stokes Equations.* Birkhäuser Verlag, Basel, 1993.

[63] L. Quartapelle and V. Selmin, High-order Taylor-Galerkin methods for nonlinear multidimensional problems. In: *Finite Elements in Fluids*, Pineridge Press, 1993, 1374–1384.

[64] A. Quarteroni and A. Valli, *Numerical Approximation of Partial Differential Equations*, Springer, 1994.

[65] V. V. Ranade, Flow in bubble columns: some numerical experiments. *Chem. Eng. Sci.* **47** (1992), no. 8, 1857–1869.

[66] R. Rannacher, On Chorin's projection method for the incompressible Navier-Stokes equations. In: proceedings of the conference *Navier-Stokes equations: Theory and Numerical Methods.* Lecture Notes in Math. **1530**, Springer, 1992, 167–183.

[67] R. Rannacher and S. Turek, A simple nonconforming quadrilateral Stokes element. *Numer. Methods PDEs* **8** (1992), no. 2, 97-111.

[68] J. O'Rourke, *Computational Geometry in C.* Cambridge University Press, 1994.

[69] J. O'Rourke, C.-B. Chien, T. Olson and D. Naddor, A new linear algorithm for intersecting convex polygons. *Comput. Graph. Image Process.* **19** (1982) 384-391.

[70] T. F. Russell, Eulerian-Lagrangian localized adjoint methods for advection-dominated problems. In: *Numerical Analysis*, Pitman Research Notes in Mathematics Series **228**, Longman Scientific & Technical, Harlow, U. K., 1990, 206-228.

[71] T. F. Russell and R. V. Trujillo, Eulerian-Lagrangian localized adjoint methods with variable coefficients in multiple dimensions. In: proceedings of the *8th International Conference on Computational Methods in*

Water Resources, Computational Mechanics Publications, Southampton, U. K., 1990, 357-363.

[72] T. F. Russell, R. V. Trujillo and D. W. Dean, Weak and direct Eulerian-Lagrangian localized adjoint methods for nonlinear physical velocity and reaction. Report No. 17, Center for Computational Mathematics, University of Colorado at Denver, 1994.

[73] A. Safjan and J. T. Oden, High-order Taylor-Galerkin methods for linear hyperbolic systems. *J. Comput. Phys.* **120** (1995) 206–230.

[74] M. P. Schwarz and W. J. Turner, Applicability of the standard k–ϵ turbulence model to gas-stirred baths. *Appl. Math. Modelling* **12** (1988) 273–279.

[75] V. Selmin, Third-order finite element schemes for the solution of hyperbolic problems. INRIA Report 707, 1987.

[76] T. K. Sherwood, R. L. Pigford and C. R. Wilke, *Mass Transfer.* McGraw-Hill, New York, 1975.

[77] A. Smolianski and D. Kuzmin, Multilayer Taylor-Galerkin schemes for convection problems. *Int. J. Numer. Meth. Engrg.* **46** (1999), no. 5, 659-670.

[78] A. Sokolichin and G. Eigenberger, Gas-liquid flow in bubble columns and loop reactors: Part I. Detailed modeling and numerical simulation *Chem. Eng. Sci.* **49** (1994), no. 24B, 5735–5746.

[79] A. Sokolichin, G. Eigenberger, A. Lapin and A. Lübbert, Dynamic numerical simulation of gas-liquid two-phase flows: Euler-Euler versus Euler-Lagrange. *Chem. Eng. Sci.* **52** (1997), no. 4, 611–626.

[80] H. F. Svendsen, H. A. Jakobsen and R. Torvik, Local flow structures in internal loop and bubble column reactors. *Chem. Eng. Sci.* **47** (1992), no. 13/14, 3297–3304.

[81] R. Temam, Sur l'approximation de la solution des équations de Navier-Stokes par la méthode des pas fractionnaires (I). *Arch. Rational Mech. Anal.* **32** (1969) 135–153.

[82] R. Temam, Sur l'approximation de la solution des équations de Navier-Stokes par la méthode des pas fractionnaires (II). *Arch. Rational Mech. Anal.* **33** (1969) 377–385.

[83] T. E. Tezduyar, M. Behr and J. Liou, A new strategy for finite element computations involving moving boundaries and interfaces — The deforming-spatial-domain/space-time procedure: I. The concept and the preliminary numerical tests. *Comput. Methods Appl. Mech. Engrg.* **94** (1992) 339–351.

[84] T. E. Tezduyar, M. Behr, S. Mittal and J. Liou, A new strategy for finite element computations involving moving boundaries and interfaces — The deforming-spatial-domain/space-time procedure: II. Computation of free-surface flows, two-liquid flows, and flows with drifting cylinders. *Comput. Methods Appl. Mech. Engrg.* **94** (1992) 353–371.

[85] R. Torvik and H. F. Svendsen, Modelling of slurry reactors. A fundamental approach. *Chem. Eng. Sci.* **45** (1990), no. 8, 2325–2332.

[86] S. Turek, A comparative study of time stepping techniques for the incompressible Navier-Stokes equations: From fully implicit nonlinear schemes to semi-implicit projection methods. *Int. J. Numer. Meth. Fluids* **22** (1996) 987-1011.

[87] S. Turek, On discrete projection methods for the incompressible Navier-Stokes equations: An algorithmical approach. *Comput. Methods Appl. Mech. Engrg.* **143** (1997) 271–288.

[88] S. Turek, *Efficient Solvers for Incompressible Flow Problems: An Algorithmic and Computational Approach*, Springer, 1999.

[89] S. O. Unverdi and G. Tryggvason, A front-tracking method for viscous, incompressible multi-fluid flows. *J. Comput. Phys.* **100** (1992) 25–37.

[90] M. Utku and G. F. Carey, Boundary penalty techniques. *Comput. Methods Appl. Mech. Engrg.* **30** (1982) 103–118.

[91] E. Varoğlu and W. D. L. Finn, Finite elements incorporating characteristics for one-dimensional diffusion-convection equation. *J. Comput. Phys.* **34** (1980) 371–389.

[92] E. Varoğlu and W. D. L. Finn, Utilization of the method of characteristics to solve accurately two-dimensional transport problems by finite elements. *Int. J. Numer. Methods Fluids* **2** (1982) 173–184.

[93] R. M. Wellek, R. J. Brunson and F. H. Law, *Can. J. Chem. Engrg.* **56** (1978) 181.

[94] M. F. Wheeler and C. N. Dawson, An operator-splitting method for advection-diffusion-reaction problems. In: *The Mathematics of Finite Elements and Applications, VI.* Academic Press, 1988, 463–482.

[95] S. T. Zalesak, Fully multidimensional flux-corrected transport algorithms for fluids. *J. Comput. Phys.* **31** (1979) 335–362.

[96] O. C. Zienkiewicz and K. Morgan, *Finite Elements and Approximation.* John Wiley & Sons, 1983.

[97] N. Zuber, On the dispersed two-phase flow in the laminar flow regime. *Chem. Eng. Sci.* **19** (1964) 897–917.

YHTEENVETO (FINNISH SUMMARY)

Väitöskirjassa tutkitaan numeeristen menetelmien avulla fysikaalisia ja kemiallisia ilmiöitä monifaasireaktorissa. Työ sisältää katsauksen kaasuneste virtausten mallintamisesta sekä yksityiskohtaisen matemaattisen mallin. Malli yhdistää kaksi-faasivirtausdynamiikan sekä massan kuljetuksen sisältäen myös homogeenisen kemiallisen reaktion nestefaasissa. Mallin yksinkertaistamista käsitellään.

Tehtävä ratkaistaan likimääräisesti äärellisten elementtien menetelmällä. Tehtävän tekee haastavaksi muun muassa liikkuvan rajapinnan seuraaminen, voimakas konvektio ja vahvat epälineaariset ilmiöt. Operaattorin jakamistekniikalla alkuperäinen tehtävä jaetaan helpommin ratkaistaviksi osatehtäviksi. Osatehtävien ratkaisumenetelmiä esitellään ja toimivuutta havainnollistetaan ns. benchmark-tehtävillä. Tärkeimpiä tuloksia ovat sisään- ja ulosvirtausreunojen käsittely Lagrangen aika-paikka äärellisten elementtien menetelmällä, pisteittäisten rajoitteiden käsittely puhtaalle konvektiotehtävälle ja massan säilyttävä yksinkertainen projektiomenetelmä laskentaverkkojen välillä. Peruskomponentit on yhdistetty globaaliksi algoritmiksi, jonka avulla on simuloitu kaasun aikaansaamaa aikariippuvaa virtausta kuplareaktorissa.

Menetelmää on sovellettu kaksiulotteisen kuplareaktorin käynnistysvaiheen tutkimiseen useilla eri toimintavaihtoehdoilla. Mallin eri parametrien merkitys on analysoitu. Esitetyt laskennalliset tulokset yhtyvät kvalitatiivisesti hyvin kirjallisuudesta saatuihin mittaustuloksiin.